

FLUORINATION OF VANADIUM OXY-PHOSPHATES FOR
HIGH-ENERGY CATHODE MATERIALS OF LI-ION BATTERIES

by

SOROOR SEMSARI PARAPARI

Submitted to the Graduate School of Engineering and Natural Sciences

in partial fulfillment of

the requirements for the degree of

Doctor of Philosophy

Sabanci University

February 2020

FLUORINATION OF VANADIUM OXY-PHOSPHATES FOR HIGH-
ENERGY CATHODE MATERIALS OF LI-ION BATTERIES

APPROVED BY:

Prof. Dr. Mehmet Ali Gülgün
(Thesis Supervisor)



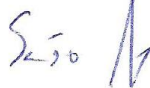
Assoc. Prof. Dr. Robert Dominko



Prof. Dr. Cleva Ow-Yang



Assoc. Prof. Sašo Šturm



Prof. Melih Papila



DATE OF APPROVAL: 28/02/2020

© Sorour Semsari Parapari 2020

ALL RIGHTS RESERVED

FLUORINATION OF VANADIUM OXY-PHOSPHATES FOR HIGH-ENERGY CATHODE MATERIALS OF LI-ION BATTERIES

Sorour Semsari Parapari

Materials Science and Nano-Engineering, PhD Thesis, 2020

Supervisor: Prof. Mehmet Ali Gülgün

Keywords: Li Ion Batteries, Cathode Materials, Vanadium Oxy-Phosphates,
Fluorination

Abstract

The requirement for sustainable high energy density materials for next generations of Li-ion batteries is driving the research to develop new materials with enhanced properties. The thesis work was focused on fluorination of vanadium oxy-phosphate cathode materials with an aim of increasing their energy density. The synthesis, structural and chemical characteristics including electrochemical properties of the vanadium oxy-phosphates and their fluorinated counterparts were investigated. β -VPO₄O, ϵ -LiVPO₄O and β -LiVPO₄O phases were synthesized by solid state synthesis method. The fluorination process was carried out under argon atmosphere at high temperatures (<600 °C) using a sealed stainless-steel reactor. Lithium fluoride (LiF) and Polytetrafluoroethylene (PTFE) compounds were used as the fluorine resources. The heat-treatment of the powder mixes of vanadium oxy-phosphate and F-containing compounds resulted in incorporation of F into the structure of materials. The ϵ -LiVPO₄O phase preserved the main framework structure after the fluorination by LiF, but it changed to LiVPO₄F-type framework by the use of PTFE as the F source. The β -VPO₄O phase formed a LiVPO₄F-type structure after the incorporation of LiF. All of the fluorinated materials had a Tavorite-type crystal structure, composed of VO₆ octahedra interconnected through corners to PO₄ tetrahedra. The operating potential of all the precursor vanadium oxy-phosphates increased after the fluorination, due to the higher ionicity of the V-O/F ligands brought by the inductive effect of F in the structure. Those conclusions were based on a systematic characterization at both micro- and nano-scale using XRD, NMR, SEM, STEM-EDS and STEM-EELS, in addition to the electrochemical characterization.

VANADYUM OXİ-FOSFAT MALZEMELERİNİN FLORİNASYONU: YÜKSEK ENERJİ Lİ İYON PİLİ KATOD MALZEMELERİ

Sorour Semsari Parapari

Malzeme bilimi ve nano-mühendisliği, Doktora Tezi, 2020

Danışman: Prof. Mehmet Ali Gülgün

Anahtar kelimeler: Li İyon Pili, Katod Malzemesi, Vanadyum Oxi-Fosfat, Florinasyon

Özet

Gelecek nesil Li-ion piller için sürdürülebilir yüksek enerji yoğunluklu malzemeler için gereksinim, araştırmayı gelişmiş özelliklere sahip yeni malzemeler geliştirmeye itiyor. Tez çalışması, enerji yoğunluklarını arttırmak amacıyla vanadyum oksî-fosfat katot malzemelerinin florlanması üzerine odaklanmıştır. Vanadyum oksî-fosfatların ve bunların florlu muadillerinin elektrokimyasal özelliklerini içeren sentez, yapısal ve kimyasal özellikleri araştırıldı. β -VPO₄O, ϵ -LiVPO₄O ve β -LiVPO₄O fazları seramik sentez yöntemiyle sentezlendi. Florlama işlemi, yüksek sıcaklıklarda argon atmosferi altında özel bir paslanmaz çelik reaktör kullanılarak gerçekleştirildi. Flor kaynağı olarak lityum florür (LiF) ve Politetrafloroetilen (PTFE) bileşikleri kullanıldı. Vanadyum oksî-fosfat ve F-içeren bileşiklerin karışımının ısıl işlemi, malzemelerin yapısına F'nin girmesiyle sonuçlanmıştır. ϵ -LiVPO₄O fazı, LiF tarafından florizasyondan sonra ana çerçeve yapısını korudu, ancak PTFE ile LiVPO₄F tipi çerçeveye dönüştü. β -VPO₄O fazı, LiF'nin dahil edilmesinden sonra bir LiVPO₄F tipi yapı oluşturmuştur. Florlanmış malzemelerin tümü, köşelerden PO₄ tetrahedraya birbirine bağlanmış VO₆ oktahedradan oluşan Tavorite tipi bir kristal yapıya sahipti. Tüm öncü vanadyum oksî-fosfatların işletme potansiyeli florlamadan sonra artmıştır. Bu, F'nin yapıdaki endüktif etkisi ile getirilen V-O/F ligandlarının daha yüksek iyonikliğinden kaynaklanıyordu. Sentezlenen malzemeler, elektrokimyasal karakterizasyona ek olarak, XRD, NMR, STEM, EDS, EELS ve benzeri gibi çeşitli yöntemler kullanılarak hem mikro hem de nano ölçekte sistematik bir karakterizasyona tabi tutuldu.

Gülümsemeyi yüzüme, ışıltıyı gözlerime ve sevgiyi kalbime koyanlara.

To the ones who put the smile on my face,

the sparkle in my eyes, and

the love in my heart.

ACKNOWLEDGMENTS

This PhD thesis becomes a reality with the kind support and help of many individuals at Sabanci University, Turkey, and at the National Institute of Chemistry (NIC), Slovenia. I am very blessed to have had the opportunity of conducting this collaborative work within these two prestigious institutes.

Foremost, I would like to express my sincere gratitude to my thesis supervisors, Prof. Mehmet Ali Gülgün and Prof. Robert Dominko for providing me the opportunity to do this PhD work. Their continuous support, encouragement, patience and immense knowledge guided me in completion of this work.

I am grateful to Prof. Gülgün for being my supervisor for my MSc and PhD studies, during the last 6 years. I have learned so much from him that has helped to broaden my vision not only academically, but also personally. He welcomed me to his research group and helped me to grow as an individual researcher. I enjoyed all our fruitful discussions about science and life, in general and research results, in particular. Mali Hoca, my academic father, made it possible for me to go to Slovenia and supported me throughout all this time.

Prof. Dominko welcomed me to his research group of *modern battery systems* at the National Institute of Chemistry and supported me unconditionally during all the thesis work. I have learned all I know about battery materials by working under his supervision. He gave me the opportunity to be at NIC, guided and led the work throughout the research and helped me to improve my work by dedicating his time and vast knowledge on batteries. Without Robert's constant support, this work could not be possible.

Besides my supervisors, I had the great pleasure of working under the mentorship of Dr. Jean Marcel Ateba Mba and Dr. Elena Tchernychova. Our stimulating discussions, especially during writing the manuscripts, helped improve the quality of this work.

The main idea of thesis work was initiated by Dr. Ateba Mba. He introduced me to the subject of vanadium oxy-phosphates and helped me with the synthesis and characterization of the materials. He also taught me how to make batteries and characterize them. His ideas helped improve the results throughout this work.

My deepest appreciation goes to Dr. Tchernychova, whose support, patience and encouragement led me to carry out and carry on with the PhD work. She helped me with the TEM work, either by teaching me or by implementing the microscopy herself. She

spent a great deal of time correcting my writing in the paper manuscript and in the thesis, for which I am enormously grateful. Her moral support gave me the will to continue during the difficult times of this study. I enjoyed every bit of our conversations during tea/coffee times. Elena has been truly like an older sister to me during my stay in Slovenia. I would like to thank Prof. Cleva Ow-Yang, Prof. Sašo Šturm and Prof. Melih Papila for being on my thesis committee and for taking the time to help improve my work. I especially thank Cleva Hoca for her guidance and unbounded kindness towards me, which has always warmed my heart. I am grateful to Prof. Šturm also for supporting me financially during the last two months of PhD at the Jožef Stefan Institute and his understanding and kindness.

My thanks go to Dr. Goran Dražić for his guidance and help related to TEM analysis and delightful chats. I thank Dr. Marjan Bele for the rewarding discussions related to the synthesis, Dr. Gregor Mali for NMR, Gregor Kapun for FIB, Edi Kranjc for XRD, Dr. Ivan Jerman and Nigel Van de Velde for Raman and Dr. Iztok Arčon for XANES measurements. I thank Ivana Maver at NIC for her helps regarding administrative works. I thank all my friends at Sabanci University, especially Melike Mercan Yıldızhan, Shalima Shawuti, Arzu Coşgun and Noyan Özkan for their friendship and support.

I am truly grateful to all my fellow labmates and friends at NIC, who were in reality my family in Slovenia. Their presence and friendship made my stay in Slovenia and my work at the *department of materials chemistry* delightful. In particular, I would like to mention Rekha Narayan, Anja Kopač Lautar, Maria Laura Para, Matija Gatalo, Francisco Ruiz Zepeda, Jože Moškon, John Fredy Velez Santa, Jan Bitenc, Klemen Pirnat, Tanja Bančič, Nejc Pavlin and Léonard Moriau.

This work was financially supported by the LiRichFCC project under the Grant Agreement No. 711792 from the EU Horizon 2020 program, by the Slovenian Research Agency (P1-0112 and P2-0393 programs) and by AkçanSA company (Turkey). The TUBITAK–ARRS Program Code 2508, Project No. 112M018 is also acknowledged.

Finally, and most importantly, I would like to thank my beloved family for their unconditional love and support throughout my life and my many years of education! My parents Akram and Rahman, my sisters Sona and Parisa, and my dearest grandparents; thank you for raising me to become who I am today and for always and ever believing in me. Special thanks go to Dr. Ali Khalili Sadaghiani, who has been the one true friend, with his kindness, encouragement and support.

TABLE OF CONTENTS

CHAPTER1: INTRODUCTION.....	1
1.1. General Introduction	1
1.2. Rechargeable Lithium Ion Batteries.....	2
1.3. Cathode Materials of Lithium Ion Batteries.....	4
1.4. Vanadium Oxy-Phosphate Polyanionic Materials	7
1.4.1. Crystal Structure of Vanadium Oxy-Phosphates	8
1.4.2. Electrochemical Properties of Vanadium Oxy-Phosphates	12
1.5. Fluorination of Phosphate Materials	15
1.6. Aim of the Thesis	17
CHAPTER2: EXPERIMENTAL TECHNIQUES	20
2.1. Synthesis	20
2.2. Characterization Methods	22
2.2.1. X-Ray Diffraction	22
2.2.2. X-ray Absorption Spectroscopy.....	23
2.2.3. Nuclear Magnetic Resonance	25
2.2.4. Scanning Electron Microscopy	26
2.2.5. Transmission Electron Microscopy	26
2.2.6. Spectroscopic techniques in TEM	27
2.2.7. Focused Ion Beam	28
2.3. Electrochemical Measurements	29
2.3.1. Positive Electrode Preparation.....	30
2.3.2. Battery Assembly.....	31
2.3.3. Electrochemical tests	33
CHAPTER3: VANADIUM OXY-PHOSPHATE INTERMEDIATE PHASES.....	36
3.1. β -VPO ₄ O	36
3.1.1. Synthesis and Characterization.....	36
3.1.2. Crystal Structure	43
3.1.3. Electrochemical Behavior.....	45
3.2. ϵ -LiVPO ₄ O	46
3.2.1. Synthesis and Characterization.....	46
3.2.2. Crystal Structure	49

3.2.3.	Electrochemical Behavior	51
3.3.	β -LiVPO ₄ O.....	53
3.3.1.	Synthesis and Characterization	53
3.3.2.	Crystal structure	58
3.3.3.	Electrochemistry	59
3.4.	LiVPO ₄ F.....	62
3.5.	Summary and Discussion	64
CHAPTER4: FLUORINATION OF VANADIUM-OXY PHOSPHATES BY LiF..		67
4.1.	Fluorination of β -VPO ₄ O by LiF	67
4.1.1.	Synthesis and Characterization	67
4.1.2.	Electrochemical Analysis	70
4.1.	Fluorination of ϵ -LiVPO ₄ O by LiF	72
4.1.1.	Synthesis and Characterization	73
4.1.2.	Electrochemical Analysis	91
4.2.	Summary and Discussion	94
CHAPTER5: FLUORINATION OF VANADIUM OXY-PHOSPHATES BY PTFE		97
5.1.	Fluorination of VPO ₄ O by PTFE	97
5.2.	Fluorination of ϵ -LiVPO ₄ O by PTFE.....	98
5.2.1.	Stoichiometric Mix: Synthesis and Characterization.....	99
5.2.2.	Stoichiometric Mix: Electrochemical Behavior	102
5.2.3.	Excess of PTFE: Synthesis and Characterization	103
5.2.4.	Excess of PTFE: Crystal Structure	106
5.2.5.	Excess of PTFE: Electrochemical Behavior	108
5.3.	Summary and Discussion	110
CHAPTER6: CONCLUSIONS.....		112
CHAPTER7: PERSPECTIVES FOR FUTURE WORK.....		117

LIST OF FIGURES

Figure 1-1 Schematic illustration of a Li-ion battery with graphite as the anode and LiCoO ₂ as the cathode, adapted from [Goodenough, 2013].	3
Figure 1-2 Schematic illustration of crystal structure of most common cathode materials: layered oxide LiCoO ₂ (left), spinel oxide LiMnO ₄ (middle) and polyanionic olivine LiFePO ₄ . Li ions are shown as purple balls [Boivin, 2017].	5
Figure 1-3 Predicted cell voltages vs. gravimetric capacity for a wide range of transition metal phosphates. Vanadium and Molybdenum couples are circled as the most promising redox couples within the electrolyte stability limit of 4.5 V (red dotted line) [Hautier, 2011].	8
Figure 1-4 Schematic of VO ₆ octahedra and PO ₄ tetrahedra in VPO ₄ O. Short V=O bond and long V-O (V...O) bond are marked [Sun, 2017].	9
Figure 1-5 Schematic representation of crystal structure of (a) α ₁ -, (b) α ₂ - and (c) β-VPO ₄ O polymorphs. The red polyhedra and purple tetrahedra denote the VO ₆ and PO ₄ units, respectively [Sun, 2017].	10
Figure 1-6 Schematic representation of crystal structure of (a) β-, (b) ε- and (c) α ₁ -LiVPO ₄ O polymorphs. Green spheres are Li atoms. The red octahedra and purple tetrahedra denote the VO ₆ and PO ₄ units, respectively [Lin, 2017].	12
Figure 1-7 The first charge–discharge cycling curve for three LiVPO ₄ O polymorphs [Hidalgo, 2019].	14
Figure 1-8 Respective positions of redox couples in a few V-containing compounds relative to the Fermi level of metallic lithium.	16
Figure 1-9 Representation of the Tavorite crystal structures. The dark and light blue polyhedra are MO ₄ Y ₂ octahedra and the yellow are XO ₄ tetrahedra. The octahedra chain is along <i>c</i> direction [001], adapted from [Masquelier, 2013].	17
Figure 1-10 Illustration of synthesis steps and related characterization in this work...	19
Figure 2-1 Schematic of the applied ceramic synthesis route to obtain the vanadium oxy-phosphate intermediate compounds.	21
Figure 2-2 Schematic of the synthesis route for the fluorination process.	21
Figure 2-3 Stainless steel reactor (autoclave) and its components, used in the synthesis process.	22
Figure 2-4 Features of an XAS spectrum for various vanadium oxide materials.	24
Figure 2-5 EELS spectrum of Si, showing various information at different energy scales [Duscher, 2019].	28
Figure 2-6 The preparation process of a lamella from a synthesized particle using FIB for TEM analysis.	29
Figure 2-7 Preparation of cathode electrodes from a slurry; (a) casting on an Al foil, (b) cutting circular electrodes using punch and (c) cut and dried electrodes, ready for battery assembling.	30
Figure 2-8 SEM micrographs of prepared composite electrode, (a) at low magnification, showing the overall view and (b) at high magnification, showing various	

components; A: active material particle, B: binder (PTFE) and C: carbon <i>Printex</i> particles.	31
Figure 2-9 Various battery testing cells: (a) beaker cell, (b) coin cell, (c) Swagelok cell and (d) pouch cell (coffee-bag cell), showing their components.	32
Figure 3-1 XRD patterns of products obtained through heat-treatment of the mix ($V_2O_3+NH_4H_2PO_4$) at various temperatures and times. w/o heating refers to the mix of precursors prior to any heat treatment.	38
Figure 3-2 XRD patterns of some of formed VPO polymorphs at various heat-treatment conditions. The purple asterisks on γ -VPO (700 °C-0h) pattern mark the β -VPO (impurity) peak positions.	39
Figure 3-3 XRD patterns of the products obtained in similar calcining conditions of 700 °C-12 h from same reactants; (a) different batches and (b) same batch. The main phase is β -VPO and the asterisks mark the position of impurities.	40
Figure 3-4 XRD patterns of the products obtained after heat-treatment at 700 °C-12h with 0.5 °C/min and 5 °C/min. Asterisks mark the impurities.	41
Figure 3-5 XRD patterns of VPO_4 and the products obtained through oxidation at 500-600-700 °C.....	42
Figure 3-6 SEM micrographs of the β -VPO particles obtained at 700 °C, (a) at low magnification, showing the agglomerate and (b) at high magnification showing the single particles.	43
Figure 3-7 Fullpattern refinement matching of β -VPO XRD pattern using LeBail method. The observed, calculated and difference curves are presented as red dots, black line and blue lines, respectively. The Bragg positions are shown as green lines. The inset shows the synthesized powder.	43
Figure 3-8 Representation of crystal structure of β -VPO, (a) interconnection of VO_6 octahedra and PO_4 tetrahedra, (b) VO_6 octahedral chain.....	44
Figure 3-9 Galvanostatic cycling curve of β -VPO at second cycle at high-voltage range (3.0-4.5 V vs. Li/Li ⁺) with a current density corresponding to C/50 cycling rate.	45
Figure 3-10 XRD patterns of the samples heat-treated at various conditions (temperature-time) from the batch prepared through ball-milling in agate jar. The pre-heated sample is also shown, marked as w/o heating. The dotted horizontal lines show the main peak positions of ϵ -LVPO, which can shift at higher temperatures.....	47
Figure 3-11 XRD patterns of the samples heat-treated at various conditions (temperature-time) from the batch prepared through ball-milling in zirconia jar.	48
Figure 3-12 SEM micrographs of the ϵ -LVPO particles obtained at 700 °C, (a) at low magnification, showing the agglomerate and (b) at high magnification showing the single particles.	49
Figure 3-13 Fullpattern refinement matching of XRD pattern of ϵ -LVPO using LeBail method. The observed, calculated and difference curves are presented as red dots, black line and blue lines, respectively. The Bragg positions are shown as green lines. The inset shows the synthesized powder.	49
Figure 3-14 The crystal structure of ϵ -LVPO; (a) and (b) interconnection of VO_6 and PO_4 tetrahedra in two different directions, and (c) octahedral chain formed from $V(1)O_4O_2$ and $V(2)O_4O_2$	51

Figure 3-15	galvanostatic cycling curves of ϵ -LVPO for the first 10 cycles, at high-voltage range (3.0-4.5 V vs. Li/Li ⁺) and low-voltage range (1.5-3.0 V vs. Li/Li ⁺).	53
Figure 3-16	XRD patterns of pre-treated batch of V ₂ O ₅ , LiF and NH ₄ H ₂ PO ₄ mix heated under air at different conditions of 300 °C-12 h, 300 °C-24 h and 450 °C-12 h. 54	54
Figure 3-17	SEM micrographs of the samples pre-treated at (a) 300 °C-24 h and (b) 450 °C-12h. 55	55
Figure 3-18	XRD patterns of the samples heat-treated at various conditions, from the batch pre-treated at 300 °C-12 h (w/o heating pattern).	56
Figure 3-19	XRD patterns of the samples heat-treated at 500 °C and 600 °C for 1 h, from the batch pre-treated at 300 °C-24 h (w/o heating pattern).	56
Figure 3-20	SEM micrographs of the sample obtained at 600 °C from the 300 °C-24 h batch, (a) at low magnification, showing the agglomerates and (b) at high magnification showing the single particles morphology.	57
Figure 3-21	XRD patterns of the samples heat-treated at 600 °C for 1 h and 12 h, from the batch pre-treated at 600 °C-12 h (w/o heating pattern).	57
Figure 3-22	Fullpattern refinement matching of XRD pattern of β -LVPO using LeBail method. The observed, calculated and difference curves are presented as red dots, black line and blue lines, respectively. The Bragg positions are shown as green lines. The inset shows the synthesized powder.	58
Figure 3-23	The crystal structure of β -LVPO; (a) interconnection of VO ₆ and PO ₄ tetrahedra and (b) octahedral chain formed from VO ₆	59
Figure 3-24	Galvanostatic cycling curve of β -LVPO at second cycle at (a) high-voltage range (3.0-4.5 V vs. Li/Li ⁺) and (b) low voltage range (1.5-3.0 V vs. Li/Li ⁺) with a current density corresponding to C/50 cycling rate.	60
Figure 3-25	Comparison between galvanostatic cycling curves of β -VPO (starting with oxidation) and β -LVPO (starting with reduction).	61
Figure 3-26	Comparison between galvanostatic cycling curves of β -LVPO and ϵ -LVPO. 62	62
Figure 3-27	XRD pattern of synthesized LVPF sample.	63
Figure 3-28	SEM micrographs of the LVPF sample, (a) at low magnification, showing the agglomerates and (b) at high magnification showing the single particles morphology. 63	63
Figure 3-29	Galvanostatic cycling curve of LVPF at second cycle at (a) high-voltage range (3.0-4.5 V vs. Li/Li ⁺) and (b) low voltage range (1.5-3.0 V vs. Li/Li ⁺) with a current density corresponding to C/50 cycling rate.	64
Figure 4-1	XRD patterns of VPO+LiF (VPOF) samples at RT and heat-treated at 400-700 °C. The red dashed lines show the position of LiF phase peaks.	68
Figure 4-2	Comparison of XRD patterns of VPOF-700 and LVPF.	69
Figure 4-3	SEM micrographs of the sample VPOF-700, (a) at low magnification, showing the agglomerates and (b) at high magnification showing the single particles morphology. 69	69
Figure 4-4	(a) ³¹ P MAS-NMR and (b) ⁶ Li MAS-NMR spectra of sample VPOF-700 in comparison to LVPF. The asterisks mark the position of spinning side-bands.	70

Figure 4-5	Galvanostatic cycling curve of the sample VPOF-700 at second cycle at (a) high-voltage range (3.0-4.5 V vs. Li/Li ⁺) and (b) low voltage range (1.5-3.0 V vs. Li/Li ⁺) with a current density corresponding to C/50 cycling rate.	71
Figure 4-6	XRD pattern of the product obtained through heat-treatment of β-VPO in the stainless steel reactor.....	72
Figure 4-7	XRD patterns of LVPOF samples heat-treated at 600 °C, 700 °C and 800 °C (LVPOF-600, LVPOF-700 and LVPOF-800, respectively) in a comparison with LVPO+LiF and LVPF samples. The patterns are shown in the selected 2θ regions chosen to emphasize the main peaks. Asterisks represent some of LVPO peaks and hashes represent LiF peaks. Blue dashed lines show the location of LVPOF peaks, adapted from [Semsari Parapari, 2020].	74
Figure 4-8	SEM micrographs of LVPOF-600, LVPOF-700 and LVPOF-800 powder samples in two different magnifications (left, lower and right, higher magnification). The arrows show the new LVPOF phase, adapted from [Semsari Parapari, 2019].	76
Figure 4-9	V K-edge XANES spectra of (a) LVPOF-600, LVPOF-700, and LVPOF-800 samples in a comparison to ε-LVPO precursor and LVPF; and (b) reference VO ₂ F, V ₂ O ₅ , VPO ₄ O, VF ₃ and ε-LVPO and LVPF samples [Semsari Parapari, 2019].....	78
Figure 4-10	³¹ P (a) and ⁷ Li (b) and (c) MAS NMR spectra of LVPOF-600, LVPOF-700, and LVPOF-800 samples in comparison to ε-LVPO precursor and LVPF. Asterisks denote spinning sidebands. In (b), ⁷ Li NMR spectra are vertically scaled so that the highest signals of different spectra are equally high, whereas in (c) they are scaled so that the signals at cca 80 ppm within the different spectra are equally high. Vertical dotted lines mark the positions of the ⁷ Li resonances of ε-LVPO and LVPF [Semsari Parapari, 2019]......	80
Figure 4-11	Rietveld refinement of LVPOF-800 sample based on X-ray powder diffraction pattern. The observed, calculated and difference curves are presented as red dots, black line and blue lines, respectively. The theoretical Bragg positions of LVPOF (green), LiF (orange), ε-LVPO (dark yellow) and Li ₃ PO ₄ (blue) are also shown [Semsari Parapari, 2019]......	81
Figure 4-12	a) Representation of Tavorite-type structure of LVPOF. b) Comparison of chains of ···[V(1)O ₄ X ₂]-[V(2)O ₄ X ₂]··· (with X=O, O/F) in ε-LVPO and LVPOF [Semsari Parapari, 2020]......	83
Figure 4-13	(a, c) SAED experimental patterns along with patterns simulated using JEMS software (Stadelmann, 1999) for LVPOF-800 and ε-LVPO samples, respectively. STEM-HAADF images of (b) LVPOF-800 and (d) ε-LVPO samples, with the line intensity profiles in the insets. Yellow dashed line denotes the intensity profile position. (e) Atomic structure of the LVPOF phase viewed in the [-101] direction along with the (f) unit cell atomic structure of LVPOF phase pictured close to [100] direction, with blue dashed lines denoting unit cell borders [Semsari Parapari, 2020]......	85
Figure 4-14	STEM-HAADF and corresponding STEM-ABF images of LVPOF-800 (a,b) and ε-LVPO (c,d) samples [Semsari Parapari, 2020]......	86
Figure 4-15	STEM-HAADF image and EDS mapping of V, P, F and O elements on a single particle of LVPOF-800 sample [Semsari Parapari, 2020].	87

Figure 4-16 FIB-cutting from an agglomerate of LVPOF-800 sample; (a) Pt-deposited particle agglomerate, (b) FIB-cut agglomerate, (c) EDX elemental mapping and (d) elemental values for 3 phases.	88
Figure 4-17 STEM-HAADF image and EDS mapping of P, V, F and O elements on the FIB-cut lamella of a particle of LVPOF-800 sample [Semsari Parapari, 2020].....	89
Figure 4-18 EELS spectra obtained at 80kV electron beam energy (a) comparison of LVPO, LVPOF-800, LVPF and reference V_2O_3 and V_2O_5 samples; (b) comparison of four different particles of (b) LVPF, (c) LVPOF-800 and (d) LVPO [Semsari Parapari, 2020].	91
Figure 4-19 Galvanostatic cycling curves obtained vs. Li at a C/50 rate for (a) LVPOF-600, LVPOF-700 and LVPOF-800 samples; and (b) ϵ -LVPO, LVPOF-800 and LVPF, in the high-voltage range (<i>i.e.</i> between 3.0 and 4.5 V vs. Li/Li ⁺) [Semsari Parapari, 2020].	93
Figure 4-20 Galvanostatic cycling curves obtained vs. Li at a C/50 rate for LVPOF-600, LVPOF-700 and LVPOF-800 samples, in the low-voltage range (<i>i.e.</i> between 1.5 and 3.0 V vs. Li/Li ⁺) [Semsari Parapari, 2020].	94
Figure 5-1 XRD patterns of VPO+PTFE mixture (VPO/T) at RT and heat-treated at 500, 600, and 700 °C.	98
Figure 5-2 XRD patterns of ϵ -LVPO+PTFE mixture (LVPO/T) at RT and heat-treated at 600, 700 and 800 °C. The black and green dashed lines respectively show the location of LVPO and LVPF peaks.	100
Figure 5-3 XRD patterns of ϵ -LVPO+PTFE mixture (LVPO/T) heated at 700 °C for 0.5 h and 5 h. The orange dashed lines show the location of LVPF peaks in LVPO/T-700.	101
Figure 5-4 SEM micrographs of sample LVPO/T-700, (a) at low magnification, showing the agglomerates and (b) at high magnification showing the single particles morphology.	101
Figure 5-5 STEM image of a particle of sample LVPO/T-700, (a) particle covered with a carbonaceous layer and (b) high-resolution image of the particle, showing the amorphous nature of the carbon layer. The inset shows the FFT of the amorphous layer.	102
Figure 5-6 Galvanostatic cycling curves obtained for LVPO/T-700 in comparison to LVPO and LVPF at a C/50 rate in the high-voltage range (<i>i.e.</i> between 3.0 and 4.5 V vs. Li/Li ⁺).	103
Figure 5-7 XRD patterns of ϵ -LVPO+2PTFE mixture at RT and heat-treated at 600, 700, 800 and 900 °C in comparison to ϵ -LVPO and LVPF. The black and green dashed lines respectively show the location of LVPO and LVPF peaks. The asterisks show the $Li_3V_2(PO_4)_3$ impurity peaks.	104
Figure 5-8 SEM micrographs of sample LVPO/2T-900, (a) at low magnification, showing the agglomerates and (b) at high magnification showing the single particles morphology.	105
Figure 5-9 STEM-HAADF image and EDS mapping of V, P, F and O elements on a single particle of LVPO/2T-900 sample.	105

Figure 5-10 Comparison of main peaks of XRD patterns of LVPO, LVPO/2T-900 and LVPF.	106
Figure 5-11 Rietveld refinement of LVPO/2T-900 sample based on X-ray powder diffraction pattern. The observed, calculated and difference curves are presented as red dots, black line and blue line, respectively. The theoretical Bragg positions of LVPF (green) and impurity $\text{Li}_3\text{V}_2(\text{PO}_4)_3$ (purple) are shown.....	107
Figure 5-12 Crystal structure of LVPO/2T-900, (a) interconnection of VO_4F_2 octahedra and PO_4 tetrahedra, (b) VO_4F_2 octahedral chain.	108
Figure 5-13 Galvanostatic cycling curve of LVPO, LVPO/2T-800, LVPO/2T-900 and LVPF at second cycle at (a) high-voltage range (3.0-4.5 V vs. Li/Li^+) and (b) low voltage range (1.5-3.0 V vs. Li/Li^+) with a current density corresponding to C/50 cycling rate.	109
Figure 7-1 XRD patterns of β -LVPO+PTFE mixture (β -LVPO/T) at RT and heat-treated at 600 °C and 700 °C in comparison to β -LVPO and LVPF. The green dashed lines show the location of LVPF peaks.	118
Figure 7-2 SEM micrographs of sample β -LVPO/T-700, (a) at low magnification, showing the agglomerates and (b) at high magnification showing the single particles morphology.	119
Figure 7-3 Galvanostatic cycling curve of β -LVPO, β -LVPO/T-700 and LVPF at second cycle at high-voltage range (3.0-4.5 V vs. Li/Li^+) with a current density corresponding to C/50 cycling rate.....	120

LIST OF TABLES

Table 1-1	Various polymorphs of VPO_4O and $LiVPO_4O$ compounds, their crystal system and space group.	9
Table 3-1	Refined structural parameters of synthesized β -VPO.....	44
Table 3-2	Structural parameters of the synthesized ε -LVPO calculated by LeBail refinement matching method.	50
Table 3-3	Structural parameters of the synthesized β -LVPO calculated by LeBail refinement matching method.	59
Table 4-1	Lattice parameters of LVPOF phase in LVPOF-600, LVPOF-700 and LVPOF-800 samples, determined from LeBail refinement.....	75
Table 4-2	Atomic parameters obtained by Rietveld refinement of XRD pattern of LVPOF-800 sample (the structure of ε -LVPO phase was used for refinement) [Semsari Parapari, 2019].....	82
Table 4-3	STEM-EDS chemical composition analysis of LVPOF-800, precursor ε -LVPO and reference LVPF samples. The values represent the average atomic percentage and standard deviations of V, P, O and F elements over 20 particles	89
Table 5-1	Structural parameters of LVPO/2T-900 calculated by LeBail refinement matching method.....	107

LIST OF ABBREVIATIONS

AC: Alternating Current

CE: Counter Electrode

CTR: Carbothermal Reduction

CV: Cyclic Voltammetry

EDS: Energy Dispersive X-ray Spectroscopy

EELS: Electron Energy-Loss Spectroscopy

EIS: Electrochemical Impedance Spectroscopy

FIB: Focused Ion Beam

GC: Galvanostatic Cycling

GITT: Galvanostatic Intermittent Titration Technique

LIB: Lithium Ion Batteries

LVPF: Lithium Vanadium Fluoro-Phosphate

LVPO: Lithium Vanadium Oxy-Phosphate

NMR: Nuclear Magnetic Resonance

PITT: Potentiostatic Intermittent Titration Technique

PTFE: Polytetrafluoroethylene

SEM: Scanning Electron Microscopy

SEI: Solid-Electrolyte Interface

STEM: Scanning Transmission Electron Microscopy

TEM: Transmission Electron Microscopy

VPO: Vanadium Oxy-Phosphate

WE: Working Electrode

XAS: X-Ray Absorption Spectroscopy

XRD: X-Ray Diffraction

CHAPTER1: INTRODUCTION

1.1. General Introduction

With the increasing energy demands, the modern civilizations have become reliant on fossil fuels, the non-renewable energy resources. Among the drawbacks of using fossil fuels is that, there is the limited supply, which cannot answer the increasing consumption needs. Only the recent two centuries were enough to consume a large part of resources that were formed during hundred millions of years in the past. Additionally, the uneven global distribution can lead to vulnerability of nation states, which are in need of importing fossil fuels. Besides these problems is the negative impact of these non-renewable energy resources on the environment. The combustion of the carbonated compounds results in release of significant amounts of CO₂, leading to an increase in the concentration of this greenhouse gas in the atmosphere. Thus, the global warming and climate change become inevitable with tragic consequences for the eco-systems. Rise of sea levels due to irregular ice melting, acidification of oceans due to high CO₂ concentration, temperature rises and draughts are just few examples of disastrous costs of fossil fuel consumption [Goodenough, 2013][IPCC, 2014].

To overcome the shortcomings of non-renewable energies, many countries have turned to renewable energies, such as hydroelectric, geothermic, wind and solar energy. It is believed that these alternative resources can deliver sufficient energy to satisfy the growing energy demand. However, most of these energy resources, such as wind energy, are dependent on weather conditions, which makes them uncertain and variable. The fluctuations in delivered energy makes these resources incompatible with the steady demand patterns for the electricity and may lead to problems in reliable service. For example, blackouts may occur during peak hours of energy demand. Therefore, an efficient energy storage system is required for regulation of electricity consumption.

Batteries and capacitors are considered the most flexible energy storage systems. As an example of their superiority, a portable rechargeable battery, together with an electrochemical capacitor can substitute the internal combustion engine by powering electric vehicles. The batteries, themselves, are well above other forms of electrical energy storage systems, with flexible sizes ranging from coin cell to megawatt load-leveling applications.

With the introduction of rechargeable Li-ion batteries (LIB) to the market in the early 1990s by SONY, a wireless revolution of cell phones, tablets, laptop computers, etc. took place, which led to a transformation in global communications. The LIBs were motivated by the need for a higher energy density in rechargeable batteries [Goodenough, 2013][Li, 2017]. Right now, LIB is a well-established and efficient energy-storage system in terms of energy and power densities, shelf life, and design flexibility. In addition to the communication sector, the efforts to electrify the transportation means due to the environmental concerns are opening up another large market for Li-ion technology. Energy density of a battery is an essential parameter that determines the vehicle autonomy range and thus makes the LIBs ever so important in this sector [Armand, 2008][Li, 2017].

1.2. Rechargeable Lithium Ion Batteries

The working principle of all batteries is based on the conversion of chemical energy to electric energy through the redox reactions at electrodes. The primary (non-rechargeable) batteries undergo a non-reversible conversion reaction, while secondary (rechargeable) batteries go through a reversible one. A battery is composed of one or more interconnected electrochemical cells, with each producing a certain current and a voltage. An electrochemical cell itself is made up of two electrodes, one an anode (negative electrode) and the other one a cathode (positive electrode), electrically separated by an electrolyte-permeable separator. Conventional room-temperature batteries have solid electrodes and liquid electrolyte. The ionic component of the chemical reactions at the electrodes is conducted through the electrolyte, while the electronic component travels through an outer load circuit, where it performs the work. The metallic current collectors (*e.g.* Cu and Al) help to deliver the electronic current from/to the redox centers of the electrodes through the terminals on the external circuit [Goodenough, 2013].

Figure 1-1 shows the components of a Li-ion rechargeable battery with graphite as the anode and LiCoO₂ as the cathode. In this system, during the charging process, the Li⁺ ions are extracted from the positive electrode due to the electric field generated by the external system. The Li⁺ ions migrate across the electrolyte towards the negative electrode, where they are intercalated between the graphite layers. Simultaneously, electrons move through the outer circuit to reach the anode. This process results in the oxidation of the transition metal ions (*e.g.* Co) in the host cathode material and the reduction of the anode material. During the subsequent discharge process, the opposite phenomena occurs in which Li⁺ ions migrate toward the cathode material where they are reinserted back into the structure and the battery returns to its equilibrium state. In this process, the migration of Li⁺ ions is driven by the electric field induced by the voltage difference between the anode and the cathode.

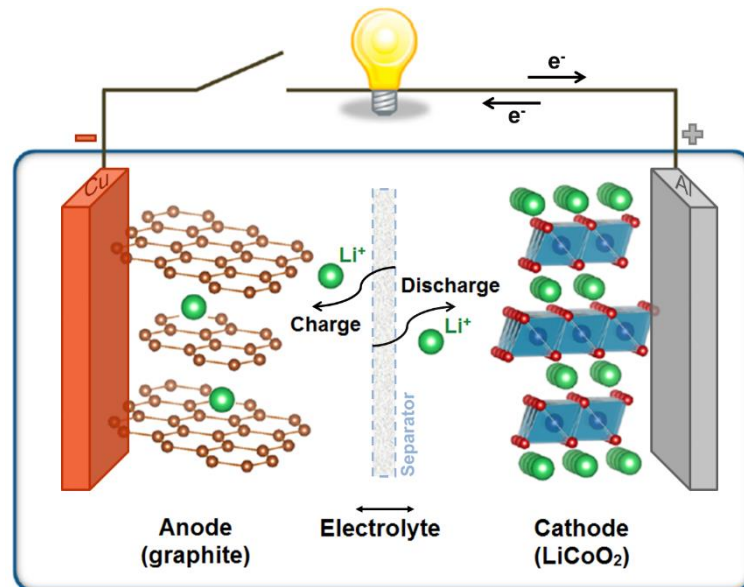
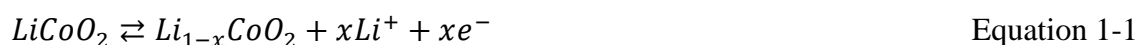


Figure 1-1 Schematic illustration of a Li-ion battery with graphite as the anode and LiCoO₂ as the cathode, adapted from [Goodenough, 2013].

The chemical reactions occurring at the cathode and the anode for the LiCoO₂-graphite system can be summarized as in Equation 1-1 and Equation 1-2, respectively:



These reversible phenomena can occur during numerous charge/discharge cycles, where Li⁺ ions can be inserted/extracted reversibly over a finite solid-solution range, or else

through a biphasic reaction at some other systems. Currently, the practical LIBs are based on insertion compounds, which can tolerate the insertion/extraction reactions free of major structural changes.

The total electrical potential energy that can be supplied by LIBs is determined by two main characteristics: *i*) the output voltage, which is determined by the difference of electrochemical potentials between the two electrode materials and *ii*) the capacity, which depends on the number of exchanged Li (and accordingly e^-) per molecular weight. The energy density of the battery is defined as the multiplication of these two parameters (voltage \times capacity) and thus, the design of proper electrode systems is of prime significance to realize a high energy density battery, as is the case for LIBs compared to other batteries.

Apart from the energy density (amount of the stored energy at a specific power), some of the other critical parameters of any rechargeable battery are safety, cycle and service life, storage efficiency, and fabrication cost [Li, 2017][Goodenough, 2010][Manthiram, 2011].

1.3. Cathode Materials of Lithium Ion Batteries

The choice of the cathode (positive electrode) materials is of great importance for the optimization of the Li-ion battery. A wide range of materials may be potentially used as the active material of cathodes in LIBs, from which, several are already commercially produced for various applications. These materials have a transition metal in their composition, which is stable at different oxidation states (can be oxidized and/or reduced reversibly). They should also have a stable crystallographic structure that allows an insertion/extraction of the Li^+ ions [Li, 2017]. The various reported materials are usually classified according to their framework structure in three main groups (Figure 1-2): layered oxides (2D frameworks), spinel oxides and polyanionic materials (3D frameworks).

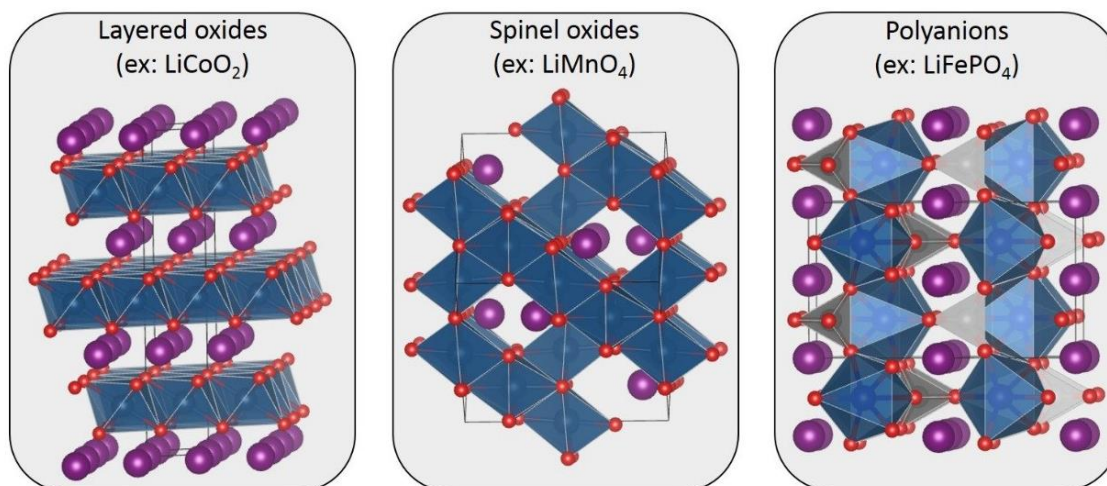


Figure 1-2 Schematic illustration of crystal structure of most common cathode materials: layered oxide LiCoO₂ (left), spinel oxide LiMnO₄ (middle) and polyanionic olivine LiFePO₄. Li ions are shown as purple balls [Boivin, 2017].

i) Layered oxides

The layered materials, with the general formula of LiMO₂ (with M as transition metal) are built up by layers of close-packed octahedra formed from M and O, with Li atoms lying in between the layers in octahedral sites. Their structure is thus a two-dimensional framework with large empty spaces, from which, lithium ions may be easily extracted/inserted. Among the layered compounds, LiCoO₂ has been widely studied and commercially used as the positive electrode material in the mobile devices' LIBs on the market. LiCoO₂ was introduced by Goodenough in the 1980s [Mizushima, 1980] and was soon commercialized by Sony in 1990s. It has a good practical performance with a working voltage of ~4 V for the Co³⁺/Co⁴⁺ redox couple and a theoretical capacity of 272 mAh/g, even though only 0.5 Li⁺ can be reversibly extracted/inserted. Extracting beyond 0.5 Li⁺ ions per formula unit, may result in structural rearrangements such as irreversible Co migration to the Li layers, leading to significant performance degradation [Wang, 1999][Macneil, 2001]. In addition, at high temperatures, the material can decompose with oxygen release from the structure, which can trigger a thermal runaway and explosion. Therefore, in commercial applications, the capacity of LiCoO₂ is being limited to ca. 140 mAh/g compared to the theoretical value of 272 mAh/g for safety reasons. However, in more recent studies, various methods such as surface coating of LiCoO₂ particles are suggested which have extended the Li extraction range and improved the structural stability [Kalluri, 2017]. Moreover, the price and toxicity of Co has motivated the

investigation of other compositions such as $\text{LiNi}_{1-y-z}\text{Co}_y\text{Al}_z\text{O}_2$, [Guilmard, 2003] and $\text{LiCo}_{1/3}\text{Ni}_{1/3}\text{Mn}_{1/3}\text{O}_2$ [Ohzuku, 2001].

ii) Spinel oxides

In order to overcome the structural instability of 2D layered structures, the 3D oxides have been suggested and widely investigated. In LiMn_2O_4 spinel oxide, the structure is built up by MnO_6 octahedra connected to each other through edge-sharing, which defines a 3D network of conduction paths for lithium motion. Spinel LiMn_2O_4 has an operating potential of 4.1 V vs. Li/Li^+ , and its high potential analogue, $\text{Li}[\text{Ni}_{1/2}\text{Mn}_{3/2}]\text{O}_4$, has a 4.7 V potential vs. Li/Li^+ . Both layered oxides and spinel oxides are reasonably good ionic and electronic conductors and lithium extraction/insertion proceeds mostly between 4V and 5V vs. Li/Li^+ while operating on the $\text{M}^{3+}/\text{M}^{4+}$ redox couple. Nevertheless, the LiMn_2O_4 spinel exhibits a lack of robustness in its cycle life and can undergo irreversible loss of capacity that may accelerate at higher temperatures [Li, 2017].

iii) Polyanionic materials

Beside the oxide materials, 2D or 3D frameworks built of transition metals and polyanions became the subject of intensive research with the discovery of electrochemically active LiFePO_4 [Padhi, 1997]. Polyanionic compounds are constructed from MO_6 octahedra (M = transition metal) and XO_4 polyhedra (X = P, S, Si, B, etc.) with a variety of frameworks with open interstitial spaces usable for easy alkaline diffusion. The substitution of oxygen anions in oxides by XO_4 groups in polyanionic compounds in fact reduces the gravimetric energy density due to the weight penalty of electrochemically inactive components. Nevertheless, the high covalency of these polyanionic groups leads to an increase in the ionicity of the metal-oxygen bonds. This, in turn, increases the operating potential vs. Li for a given redox couple, due to the inductive effect, compared to the oxide form. The “inductive effect” mechanism was theorized and experimentally shown by Goodenough [Manthiram, 1989]. According to this theory, the potential of a given redox couple ($\text{M}^{n+}/\text{M}^{(n+1)+}$) is affected by the iono-covalent character of the bonds formed by M and its ligands. An increase of the ionicity of metal-ligand bond tends to stabilize the antibonding 3d orbitals of the transition metal and as a result, increase of the difference of fermi levels between the anode and the cathode materials. Tuning the potential is further possible by tuning the nature of the polyanionic group, since the electronegativity of the X would affect the X-O bond covalency and therefore the iono-covalent character of the M-X-O bond.

The large variety of crystal structures that the polyanionic compounds can assume, with the possibility of cationic and anionic substitutions, allows for adjusting desired property according to the required application. Moreover, the polyanionic frameworks sustain long-term structural stability, which is essential for extensive electrochemical cycling and safety issues [Masquelier, 2013].

1.4. Vanadium Oxy-Phosphate Polyanionic Materials

One major challenge with the polyanion-type cathodes is their relatively low energy density compared to the structurally simpler oxide forms, due to the presence of inactive ions in the composition. For example, LiFePO_4 has a theoretical energy density of 587 Wh/kg, which is comparatively lower than LiCoO_2 with 1000 Wh/kg theoretical energy density [Whittingham, 2014]. One effective strategy to overcome this shortage and increase the storage capacity is to explore materials with multiple electron transfer, *i.e.* incorporation of a second electron per metal redox center. This can be done by inserting two single-valent ions (Li^+ , Na^+) or one multi-valent ion (Mg^{2+} , Ca^{2+}). Some cathode materials have the potential to store two lithium ions through the insertion/extraction mechanism such as layered dichalcogenides like VSe_2 , and vanadium oxy-phosphate VPO_4O . Figure 1-3 [Hautier, 2011] shows a graph built of the expected potentials in a lithium cell for various transition metal phosphates, some with the possibility of using two electrons. The red dotted line shows the electrolyte stability limit. We can see that Mo and V are circled as the most promising candidates. Vanadium is well-known in this regard with the capability of reacting with two electrons, for example in the oxide form, V_2O_5 [Whittingham, 2014][Whittingham, 2018].

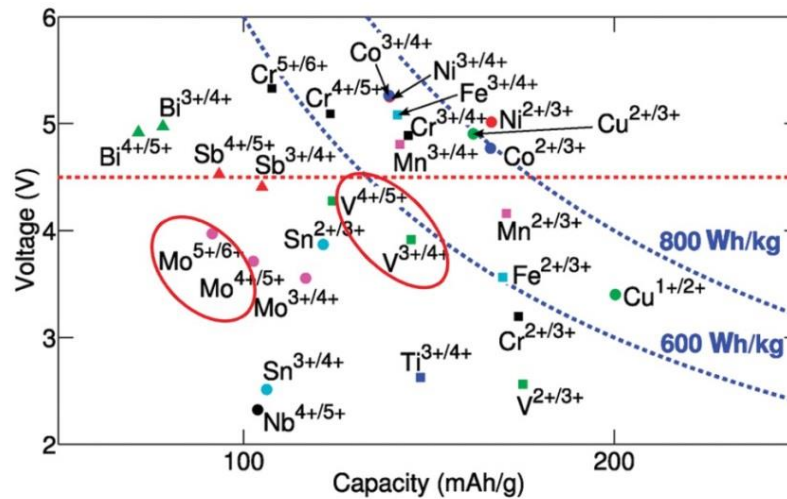


Figure 1-3 Predicted cell voltages vs. gravimetric capacity for a wide range of transition metal phosphates. Vanadium and Molybdenum couples are circled as the most promising redox couples within the electrolyte stability limit of 4.5 V (red dotted line) [Hautier, 2011].

The vanadium oxy-phosphates (known also as vanadyl phosphates) are attractive polyanionic cathode materials which can reach high energy densities. Their general chemical formula is $\text{Li}_x\text{VPO}_4\text{O}$ (with $x=0,1,2$) which can also be described as Li_xVOPO_4 (vanadyl description). These materials consist of vanadyl (VO) and phosphate (PO_4)³⁻ groups. Vanadyl term refers to a double $\text{V}=\text{O}$ bond with a short bond length (1.57-1.68 Å) [Clark, 1968][Schindler, 2000]. Because of enhanced ionicity of $\text{V}-\text{O}$ bonds in the presence of (PO_4)³⁻ anion, the $\text{V}^{4+}/\text{V}^{5+}$ redox couple of VPO_4O has a higher redox potential than oxide V_2O_5 [Park, 2001]. Vanadium oxy-phosphates can undergo a two-electron reaction through reduction of V^{5+} to V^{3+} , of which, both redox potentials are useful for energy storage. For the insertion of one Li ion at a voltage of 3.5–4.0 V vs. Li/Li^+ , the theoretical capacity of VPO_4O is 166 mAh/g, which can increase to 332 mAh/g upon the insertion of a second lithium. This would happen through $\text{VPO}_4\text{O} \leftrightarrow \text{LiVPO}_4\text{O} \leftrightarrow \text{Li}_2\text{VPO}_4\text{O}$ reactions [Whittingham, 2005][Song, 2005][Bianchini, 2014][Harrison, 2013][Chen, 2013][Ateba Mba, 2013][Siu, 2018].

1.4.1. Crystal Structure of Vanadium Oxy-Phosphates

In the research for the insertion-type cathode materials, the crystal chemistry and structure, including the polymorphism of the active material are of utmost importance. These aspects can play a role in determining many intrinsic electrochemical characteristics such as the lithiation voltage and the path and barrier for lithium diffusion

[Eames, 2012][Sirisopanaporn, 2010]. The rich crystal chemistry and high polymorphism of vanadium oxy-phosphates besides the promising electrochemical properties, thus, attract a great deal of interest in the field of LIB cathode materials.

VPO₄O compound has seven known polymorphs and LiVPO₄O compound (the lithium-containing form) has three known polymorphs that are reported in the literature [Azmi, 2002][Hidalgo, 2019]. The polymorphs of VPO₄O and LiVPO₄O are listed in Table 1-1, with their crystal systems and space groups. The polymorphs of VPO₄O consist of layered α_I , α_{II} , δ , ω , γ , and three-dimensional β , ϵ . The crystal systems of α_I , α_{II} , δ and ω polymorphs are tetragonal, β and γ are orthorhombic, and ϵ is monoclinic [Sun, 2017]. Despite of their different systems, they are all composed of VO₆ octahedra and PO₄ tetrahedra (Figure 1-4).

Table 1-1 Various polymorphs of VPO₄O and LiVPO₄O compounds, their crystal system and space group.

Polymorph	Crystal system	Space group
α_I -VPO ₄ O	tetragonal	<i>P4/n</i>
α_{II} -VPO ₄ O	tetragonal	<i>P4/n</i>
δ -VPO ₄ O	tetragonal	<i>P4₂/mbc</i>
ω -VPO ₄ O	tetragonal	<i>P4₂/mmc</i>
β -VPO ₄ O	orthorhombic	<i>Pnma</i>
γ -VPO ₄ O	orthorhombic	<i>Pbam</i>
ϵ -VPO ₄ O	monoclinic	<i>Cc</i>
α_I -LiVPO ₄ O	tetragonal	<i>P4/nmm</i>
β -LiVPO ₄ O	orthorhombic	<i>Pnma</i>
ϵ -LiVPO ₄ O	triclinic	<i>P$\bar{1}$</i>

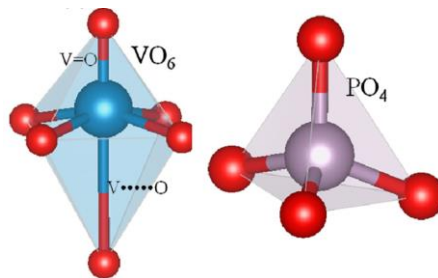


Figure 1-4 Schematic of VO₆ octahedra and PO₄ tetrahedra in VPO₄O. Short V=O bond and long V-O (V...O) bond are marked [Sun, 2017].

The VO₆ polyhedron is so strongly distorted that it is often considered as a VO₅ square pyramid with a very short V=O bond (~1.6-1.8 Å) and a much longer V-O bond (~2.2 Å) in the opposite direction. Both of the “octahedral” VO₆ and “pyramidal” VO₅ representations have been mentioned in different studies [Dupre, 2004a] [Girgadies, 2006] [Azmi, 2002]. The distorted VO₆ polyhedra share corners to form infinite O=V...O=V chains. PO₄ groups act like bridges between these chains and result in formation of 3D frameworks. The structural variation in VPO₄O polymorphs is mainly caused by the variation in the orientation of the vanadyl bond (V=O). Figure 1-5 illustrates two examples of VPO₄O polymorphs’ structure; layered structure of α₁ and three-dimensional structure of β. In α₁-VPO₄O, the consecutive polyhedra layers are connected through V...O bond [Jordan, 1973]. In β-VPO₄O, the VO₆ octahedra are tilted to form zig-zag O=V...O=V chains, contrary to all the other VPO₄O polymorphs, and PO₄ tetrahedra connect the neighboring layers [Gopal, 1972][Sun, 2017]. All of the vanadium oxy-phosphate phases are constituted of the same building blocks with different stacking. Note that, there are two different V sites alternating along the octahedra chain.

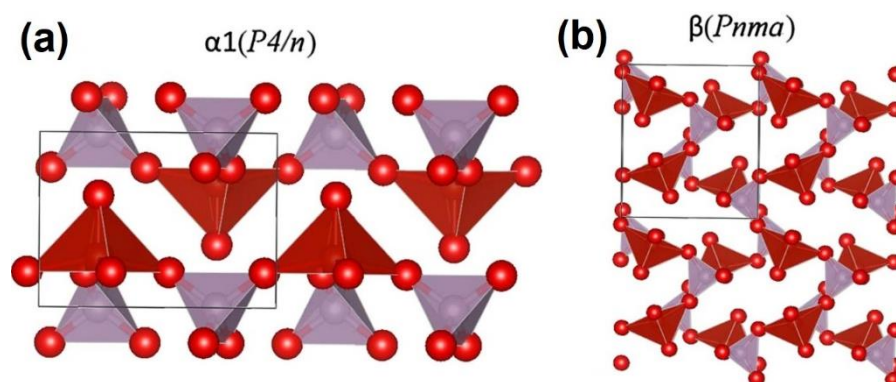


Figure 1-5 Schematic representation of crystal structure of (a) α₁- and (b) β-VPO₄O polymorphs. The red polyhedra and purple tetrahedra denote the VO₆ and PO₄ units, respectively [Sun, 2017].

Formation of VPO₄O polymorphs depends highly on the synthesis conditions, *e.g.* temperature and pressure. For example, α_I-VPO₄O can be obtained by dehydration of α-VPO₄O·2H₂O at 250°C, while ω-VPO₄O is obtained by slow heating of VOHPO₄·*n*H₂O (*n*=2, 4) under air. β-VPO₄O is the only polymorph that is observed to form above 700 °C [Azmi, 2002]. It should be noted that the small changes in the synthesis conditions often lead to mixtures of polymorphs, especially for α_{II}-, γ-, and δ-VPO₄O. This is due to a small formation energy difference between these polymorphs. For that reason, as well

as due to the difficulty in achieving high crystallinity, the structural characterization of VPO_4O has been challenging [Dupre, 2004].

The lithium containing form of vanadium oxy-phosphates, LiVPO_4O , has three distinct polymorphs: ϵ with triclinic, β with orthorhombic and α_1 with tetragonal crystal structures. The nomenclature used in the literature to address these polymorphs can be confusing since the Greek letters were being assigned in the order of phases being discovered. Therefore, in the literature α - LiVPO_4O does not refer to the Li-containing form of α - VPO_4O and actually to ϵ - VPO_4O [Whittingham, 2014]. In this thesis, for the sake of clarity, the names of the Li-free forms will be used equivalent of the Li-containing forms. Thus, ϵ - LiVPO_4O , β - LiVPO_4O and α_1 - LiVPO_4O are the Li-containing forms of ϵ - VPO_4O , β - VPO_4O and α_1 - VPO_4O , respectively.

Similar to VPO_4O , LiVPO_4O framework is also constructed from interconnected VO_6 octahedra and PO_4 tetrahedra via trans-corner-sharing (Figure 1-6). The VO_6 octahedron is distorted having four almost equal V–O bonds along with one short and one long V–O bonds. The distortion in α_1 - LiVPO_4O polymorph is more pronounced than other polymorphs. It is still not completely known if these structures undergo an extensive phase change upon lithium insertion/extraction. However, the lithiated forms generally follow the same structural trends as the VPO_4O polymorphs. Triclinic ϵ - LiVPO_4O features a connectivity pattern same as ϵ - VPO_4O , while orthorhombic β - LiVPO_4O is related to β - VPO_4O . The tetragonal α_1 - LiVPO_4O polymorph contains an α_1 - VPO_4O type host lattice. Nevertheless, an inversion of vanadyl bonds from VPO_4O to LiVPO_4O has been observed for the ϵ polymorph. In contrast to the parallel oriented VO_5 pyramid stacks in ϵ - VPO_4O structure, ϵ - LiVPO_4O contains anti-parallel stacks. Thus, every second $\text{V}=\text{O}\cdots\text{V}$ chain has to be inverted during the insertion of one lithium into ϵ - VPO_4O . The “easy” inversion of vanadyl bonds could impose a mechanism that would allow the VPO_4O lattice to accommodate the additional lithium ions. Upon Li insertion, the monoclinic lattice of ϵ - VPO_4O with a formula volume of 82.14 \AA^3 transforms to a distorted triclinic lattice of ϵ - LiVPO_4O with a slight increase in volume (85.51 \AA^3 formula unit). The flexibility of the lattice could be an important factor in obtaining interesting electrochemical properties for the VPO_4O family [Whittingham, 2014][Ling, 2014][Berrah, 2001][Lavrov, 1982][Girgsdies, 2006][Dupre, 2004b][He, 2018].

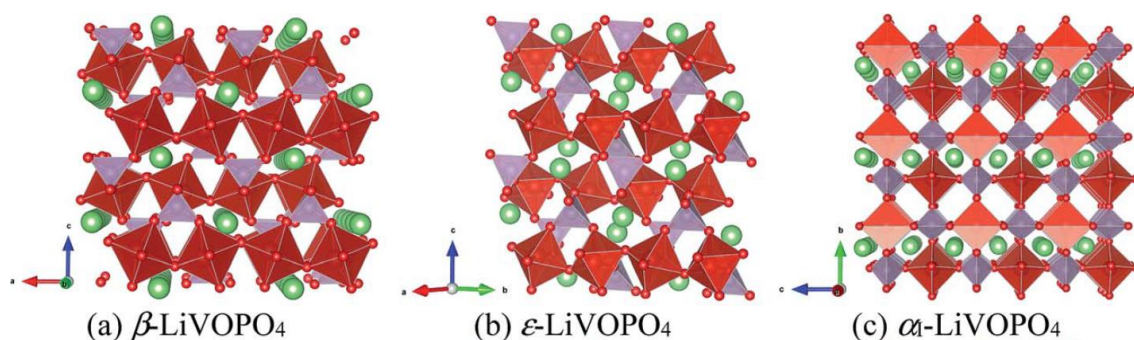


Figure 1-6 Schematic representation of crystal structure of (a) β -, (b) ϵ - and (c) α_1 -LiVOPO₄O polymorphs. Green spheres are Li atoms. The red octahedra and purple tetrahedra denote the VO₆ and PO₄ units, respectively [Lin, 2017].

Similar to VPO₄O, the complicated polymorphism of LiVPO₄O challenges the synthesis of a pure phase, although the energy difference between LiVPO₄O polymorphs is generally higher compared to VPO₄O polymorphs. This, in turn, inhibits a comprehensive understanding of the structure-related electrochemical properties [Ling, 2014][Lin, 2017].

Among VPO₄O polymorphs, β -VPO₄O is predicted to be the most stable, while with the insertion of one lithium, ϵ -LiVPO₄O becomes the most stable phase. This shows itself in the synthesis procedure, as well, where ϵ -VPO₄O transforms to β -VPO₄O and β -LiVPO₄O transforms to ϵ -LiVPO₄O by heating above a certain temperature. Comparison of lattice volumes can give a hint about the stability in an ionic lattice, since the most compact phase is expected to be the most stable. However, it is not the sole parameter. In the Li-containing form (LiVPO₄O), the volume/VPO₄O unit is in the order:

$$\beta (83.74 \text{ \AA}^3) < \epsilon (85.51 \text{ \AA}^3) < \alpha_1 (87.97 \text{ \AA}^3)$$

Whereas, for the Li-free form (VPO₄O), the order is:

$$\alpha_1 (80.35 \text{ \AA}^3) < \epsilon (82.14 \text{ \AA}^3) < \beta (83.14 \text{ \AA}^3)$$

Nevertheless, we should note that the kinetics rather than thermodynamics might control the phase stability [Whittingham, 2014][Zhou, 2017].

1.4.2. Electrochemical Properties of Vanadium Oxy-Phosphates

Vanadium oxy-phosphate materials offer interesting electrochemical properties due to their rich crystal chemistry and also the presence of multiple-valent vanadium. The ability to exchange more than one electron during the electrochemical charge/discharge provides

a high theoretical specific capacity. This capability, in addition to the relatively high operating potential, offers a high energy density for these materials to be used as cathode materials of LIBs. In spite of the superior properties, the observed electrochemical performance of VPO₄O and LiVPO₄O vanadium oxy-phosphate materials is still far from the theoretical values. The achievable capacity of VPO₄O usually remains below 160 mAh/g and the direct accessibility to the insertion of the second lithium is still unclear. Different polymorphs of VPO₄O and LiVPO₄O may vary considerably in terms of the electrochemical properties. Additionally, small changes in synthesis conditions can affect the capacity or cyclability, even for the same crystal structure materials [Azmi, 2003][Harrison, 2013].

The α_I , α_{II} , δ and ω polymorphs of VPO₄O show high potential of 3.7 V and 3.9 V for the electrochemical insertion (reduction) and extraction (oxidation) reactions of Li. However, for β and ϵ polymorphs, the observed potential is slightly higher, being 3.8 V and 4.1 V for insertion and extraction of Li. The strong covalency of vanadyl V=O bond has an effect on lowering the redox potential of these compounds than the expected values. Higher covalency which results in shorter bond length for V=O bond results a lower redox potential. For example, the V=O bond length is 1.58 Å and 1.69 Å for α_I -VPO₄O and ϵ -VPO₄O, respectively. As mentioned in the previous section, the β and ϵ polymorphs of VPO₄O have a 3D network with an open tunnel structure, which could facilitate their use as electrodes for LIBs with respect to other polymorphs. On the other hand, the charge and discharge capacity also vary among different polymorphs, despite having the same chemical composition. This may be due to differences in stability of crystal structure and the average valence number of vanadium cation in crystals. The studies have shown that the capacity for initial insertion of Li is in the following order, $\beta \ll \alpha_{II} < \omega < \alpha_I < \epsilon < \delta$ for VPO₄O polymorphs. The δ , ϵ , α_I , and ω polymorphs of VPO₄O exhibit fairly large capacity, while β polymorph has the lowest one. This may be related to the strength of the chemical bonds. For instance, the V=O bond is stronger (higher covalency) in β -VPO₄O compared to ϵ -VPO₄O, which was deduced from the higher frequency shift of V=O in β -VPO₄O in IR spectra. This can suggest that the redox reaction of V in ϵ -VPO₄O can proceed easier than that in β -phase, which would lead to a higher capacity in ϵ -VPO₄O [Azmi, 2002][Gaubicher, 1999][Kerr, 2000][Dupre, 2001].

The variation in electrochemical performance is also observed for the three polymorphs of LiVPO₄O. However, their closely related structures lead to similarities in their

behavior. There is discrepancy in literature regarding the electrochemical characteristics such as capacity and operating potential of the three polymorphs. One important factor in inducing such differences is the applied synthesis route and even small variations of synthesis conditions. This means that the structural chemistry of these materials is highly dependent on the applied synthesis method. In addition, the electrode preparation technique can also affect the electrochemical observations. Therefore, for a fair comparison of the properties of LiVPO_4O polymorphs, it is recommended to study the materials synthesized through similar methods. One such study is the work by Whittingham group [Hidalgo, 2019][Lin, 2017], in which, three polymorphs were obtained through the heat treatment of $\text{LiVPO}_4\text{O}\cdot 2\text{H}_2\text{O}$ precursor at various temperatures and/or atmospheres. The first charge–discharge cycling curves for three LiVPO_4O polymorphs obtained in that work are shown in Figure 1-7. The operating potentials of all three polymorphs at the high-voltage range ($>3\text{V}$) are very close to each other ($\sim 4\text{V}$). However, $\beta\text{-LiVPO}_4\text{O}$ shows slightly higher potential than $\varepsilon\text{-LiVPO}_4\text{O}$, which in its turn has a bit higher potential compared to $\alpha_1\text{-LiVPO}_4\text{O}$. The cycling curve at the low-voltage range ($<3\text{V}$) varies more prominently for the three polymorphs regarding the voltages as well as the lithiation mechanism, as can be seen from the difference of curve shape. Here (Figure 1-7), $\beta\text{-LiVPO}_4\text{O}$ has the highest achievable capacity among three phases, which can be related to its better kinetics [Lin, 2017]. These findings are in contrast with the results from Zhou *et al.*, where they showed a higher achievable capacity for $\varepsilon\text{-LiVPO}_4\text{O}$ compared to $\beta\text{-LiVPO}_4\text{O}$. They relate it to the more open structure of ε polymorph compared to β polymorph (85.51 \AA^3 vs. 83.74 \AA^3 volume/ VPO_4O) which resulted in better reaction kinetics [Zhou, 2017].

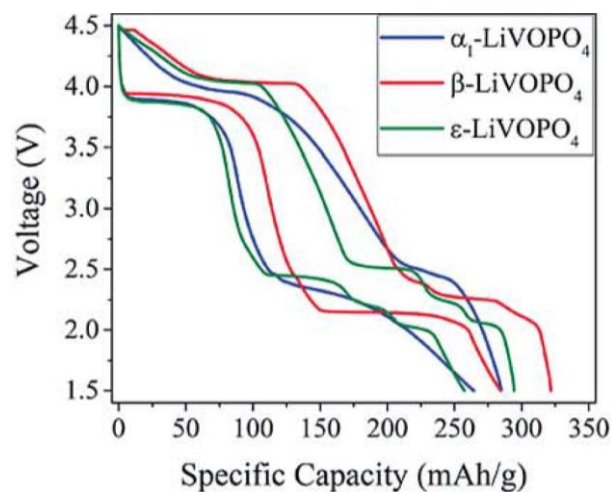


Figure 1-7 The first charge–discharge cycling curve for three LiVPO_4O polymorphs [Hidalgo, 2019].

Lithium has 1D and 2D diffusion pathway in β -LiVPO₄O and α_1 -LiVPO₄O, respectively. The diffusion pathway in ϵ -LiVPO₄O is under debate, where some studies [Yang, 2008][Lin, 2017] claim a pseudo-1D channel similar to β -LiVPO₄O and some [He, 2018] claim a 2D diffusion channel for Li. Nevertheless, a complete lithium extraction is nearly never realized in ϵ -LiVPO₄O, probably due to the distorted lattice, poor diffusion kinetics (especially for V⁴⁺/V⁵⁺ redox couple) and low intrinsic electronic conductivity (mainly due to the insulating PO₄ units that isolate the V atoms within the lattice). These factors can limit the application of vanadium oxy-phosphate materials. Various studies have been conducted, where the Li extraction has been shown to improve by changing some parameters such as synthesis method, nano-sizing and carbon coating, which can have effect on shortening the conduction length and Li diffusion pathway [Shi, 2019][He, 2018][Lin, 2017][Bianchini, 2014][Siu, 2018].

1.5. Fluorination of Phosphate Materials

Introduction of fluorine into the composition of compounds has been suggested as an effective way to increase their energy density. Fluorine can play a role in increasing the redox potential by exploiting the inductive effect due to its high electronegativity. As it was discussed in section 1.3 for polyanionic materials, the ionocovalency of the M-X bond (M: transition metal, X: anion) governs the redox potential of insertion electrode materials. The higher the electronegativity of the anion, the higher is the ionicity of the bond and as a result, higher redox potential. Since fluorine has a higher electronegativity compared to oxygen, it imposes a higher potential. As an example, the redox potential of LiFePO₄F is 850 mV higher than that of LiFePO₄ due to the higher ionicity of Fe-F bond compared to Fe-O bonds. In fact, the compounds containing both fluorine and phosphate groups can benefit from the inductive effect of both anionic species. Therefore, in recent years, these materials have captured much attention as candidates for Li-ion battery cathodes. Incorporation of fluorine in the structure can bring other advantages such as improving the easy transport of Li⁺ ions and improving the safety. The latter is due to a higher stability of the structure [Julien, 2016][Antipov, 2015].

The vanadium-containing fluoro-phosphate, LiVPO₄F, was first proposed and described by Barker et al. [2003][2005a][2005b]. This material has the highest redox potential among V³⁺/V⁴⁺ redox couples in polyanion compounds with ~4.2 V vs. Li/Li⁺. This is

located 0.4 V higher than fluorine-free $\text{Li}_3\text{V}_2(\text{PO}_4)_3$ with ~ 3.8 V vs. Li/Li^+ . Figure 1-8 illustrates the respective position of redox couples in these two materials versus lithium in the energy diagram. V_2O_5 and LiVPO_4O are also shown in this diagram. LiVPO_4F can achieve 655 Wh/kg of energy density and in addition, has high structural and thermal stability [Sun, 2013][Zhou, 2009]. Typical thermal response of the LiVPO_4F phase obtained by differential scanning calorimetry shows that, with a heat flow of ~ 205 J/g, the safety characteristics is vastly superior to known oxide cathode materials (for instance 345 J/g for LiMn_2O_4) [Gover, 2006].

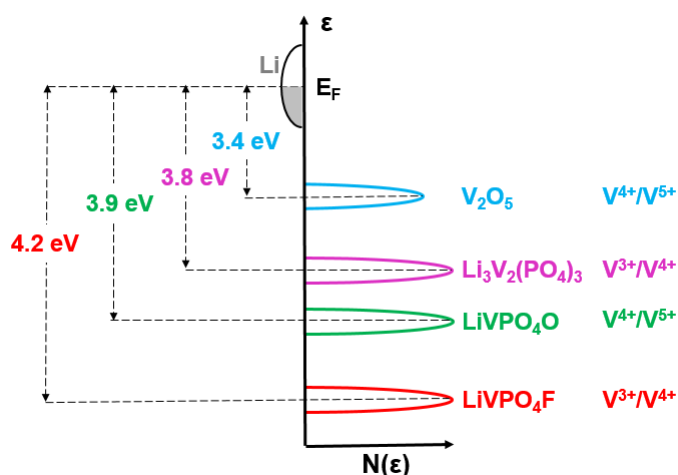


Figure 1-8 Respective positions of redox couples in a few V-containing compounds relative to the Fermi level of metallic lithium.

LiVPO_4F is isostructural with the mineral Tavorite, with the chemical formula of LiFePO_4OH , and therefore is classified as a Tavorite-type material. The ϵ - LiVPO_4O and ϵ - VPO_4O vanadium oxy-phosphates, described in Section 1-4, also have Tavorite-type structure. Tavorite materials crystallize in triclinic ($P\bar{1}$ space group) or monoclinic ($C2/c$ space group) structure. The general chemical formula of this family of materials is $\text{A}_x\text{MXO}_4\text{Y}$, with A as alkaline ion, M as a transition metal, X as phosphorus or sulfur and Y as fluorine, hydroxide or oxygen. The structure (Figure 1-9) is built up by $[\text{MO}_4\text{Y}_2]$ octahedra and $[\text{XO}_4]$ tetrahedra connected to each other through their corners. The octahedra form chains, where they are connected to each other via ligand Y (bridging anion). These chains are then linked to each other through $[\text{XO}_4]$ tetrahedra. In these structures, in addition to the polyanion, the bridging anion (F, OH, O) can play a significant role in improving the working potential of the material by tuning the inductive effect. In fact, the potential of the redox couple is highly influenced by the local environment of the transition metal [Masquelier, 2013][Whittingham, 2014]. Therefore,

adjusting the amount of O and F as the ligand can have substantial effect on the electrochemical properties of such materials.

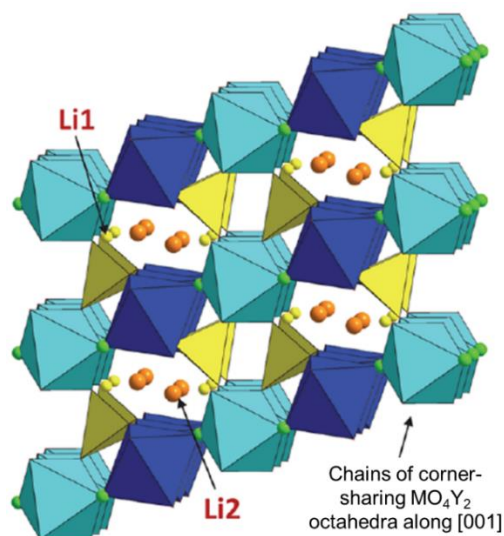


Figure 1-9 Representation of the Tavorite crystal structures. The dark and light blue polyhedra are MO_4Y_2 octahedra and the yellow are XO_4 tetrahedra. The octahedra chain is along c direction [001], adapted from [Masquelier, 2013].

Recently studied lithium vanadium oxy/fluoro-phosphate compounds demonstrated oxygen partial substitution by fluorine so as to form a solid solution [Onoda, 2015][Ma, 2016][Kim, 2017][Boivin, 2016][Boivin, 2018][Boivin, 2019]. Such compounds were produced either by solid-state synthesis, or by oxidation of LiVPO_4F -based compound. In these works, promising results were achieved where the produced materials were distinguishable from LiVPO_4F and LiVPO_4O . Kim *et al.* [2017] synthesized $\text{LiVPO}_4\text{O}_{0.75}\text{F}_{0.25}$ compound with +3.75 as V valence state which had working potentials at ~4.1 V and ~2.4 V (vs. Li/Li^+). Boivin *et al.* [2018] worked on synthesizing a larger composition range of $\text{LiVPO}_4\text{O}_{1-x}\text{F}_x$ with mixed V^{3+} - V^{4+} valence state. They showed that the electrochemical performance of these materials can be tuned by changing the amount of vanadyl-type defects, *i.e.* the ionicity ($\text{V}^{3+}\text{-F}$) or covalency ($\text{V}^{4+}\text{=O}$) of the bond.

1.6. Aim of the Thesis

The aim of thesis work is to modify and enhance the electrochemical properties of vanadium oxy-phosphate (VPO_4O and LiVPO_4O) materials by introduction of fluorine in their structure. Vanadium oxy-phosphate materials offer promising electrochemical properties due to their rich crystal chemistry as well as the presence of multiple-valent

vanadium. The ability to exchange more than one electron during the electrochemical charge/discharge provides a high theoretical specific capacity. This, in addition to the relatively high operating potential, makes these compounds important candidates for high energy density cathode materials for LIBs. The crystal structure strongly influences the key electrochemical properties in these systems. Thus, a complete Li extraction/insertion is nearly never realized due to the poor diffusion kinetics and the distorted lattice of (Li)VPO₄O.

To the best of our knowledge, there has been no study on modifying the electrochemical characteristics of vanadium oxy-phosphates by tuning their crystal structure. The hypothesis of this work was built on the fact that the introduction of F in the material would lead to structural changes. Fluorine atoms are expected to substitute, partially or completely, the oxygen atoms on the V-O ligands of the VO₆ octahedral chains. The higher ionicity of the formed V-F bonds due to the inductive effect of F would lead to higher operating potential vs. Li. Additional effects on the structure such as altering the lattice distortions would provide an easier Li diffusion path and lead to improvement in electrochemical cycling behavior. Furthermore, the high electronegativity of the F⁻ anion could increase the stability of the host structure and therefore, the safety parameters.

Three vanadium oxy-phosphate phases, namely β-VPO₄O, ε-LiVPO₄O and β-LiVPO₄O are synthesized and further fluorinated with lithium fluoride and polytetrafluoroethylene (PTFE) as the fluorine resources in order to prove the above stated hypothesis. Figure 1-10 shows the hierarchical steps of the synthesis and the related characterization methods. The vanadium oxy-phosphates and their fluorinated counterparts are characterized for their chemical and structural properties by means of XRD, SEM, NMR, XANES and advanced analytical STEM (EELS and EDX) techniques. Electrochemical properties were characterized with electrochemical galvanostatic cycling (GC).

The results obtained within this work are contributing to more profound understanding of the fluorination induced by different fluorinating agents. The correlation between structural, chemical and electrochemical characterization results is essential to further tuning of the electrochemical properties of vanadium oxy/fluoro-phosphates.

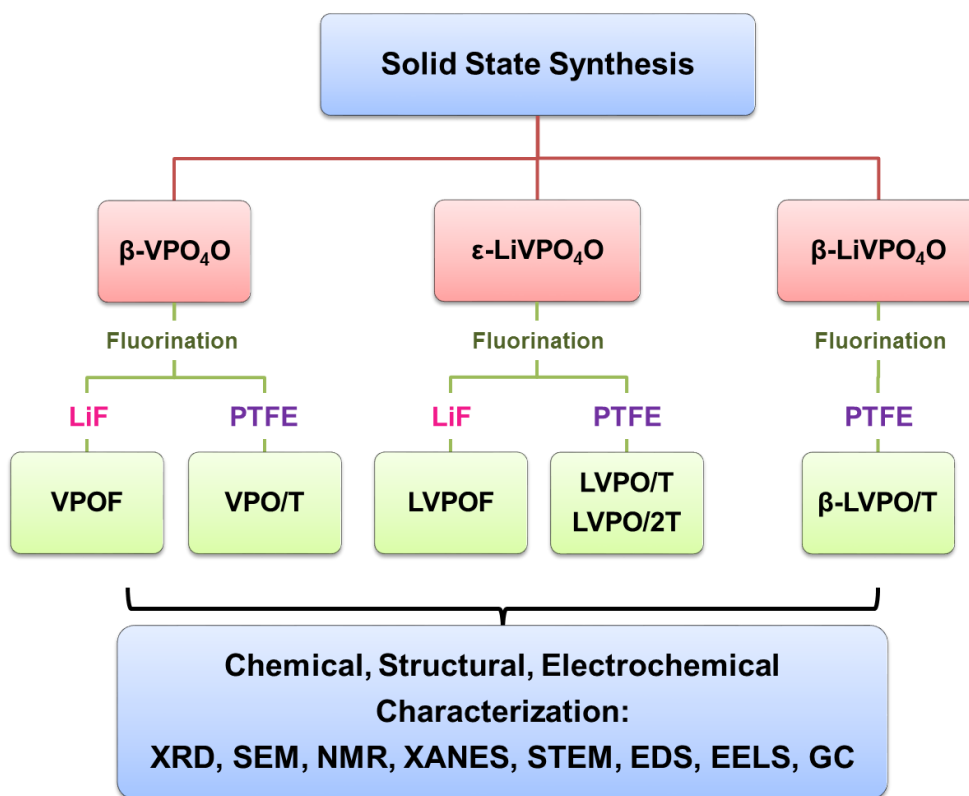


Figure 1-10 Illustration of synthesis steps and related characterization in this work. The nomenclature is an arbitrary naming of the synthesis products, such as VPOF being the product of fluorination of β -VPO₄O by LiF, etc.

CHAPTER2: EXPERIMENTAL TECHNIQUES

2.1. Synthesis

Solid-state reaction technique was used in this thesis as the main method for the synthesis of vanadium oxy-phosphate materials (the intermediate compounds) and their fluorinated counterparts (final products).

Solid-state ceramic synthesis of the vanadium oxy-phosphates was initiated by weighing out the various precursors in the stoichiometric amounts, according to the intended product. Figure 2-1 shows a schematic of the synthesis process of the oxy-phosphate compounds. A thorough grinding of the precursors was necessary to obtain a homogenous mixture and also to have large surface area to maximize the contact between particles [Callister, 2011]. Therefore, the reactant mixture was ball-milled in agate jar (or else zirconia jar) using high energetic planetary ball-milling machine at 600 rpm rotations. The well-mixed batch was then pressed as pellets to increase the intimate contact between particles. The pellets were placed in alumina crucibles and then pre-heated at low temperatures (generally 300 °C) under argon or oxygen flow inside a quartz tube. Afterwards, they were ground again to obtain a homogeneous powder. This powder was then heated at high temperatures (according to the product, up to 800 °C).

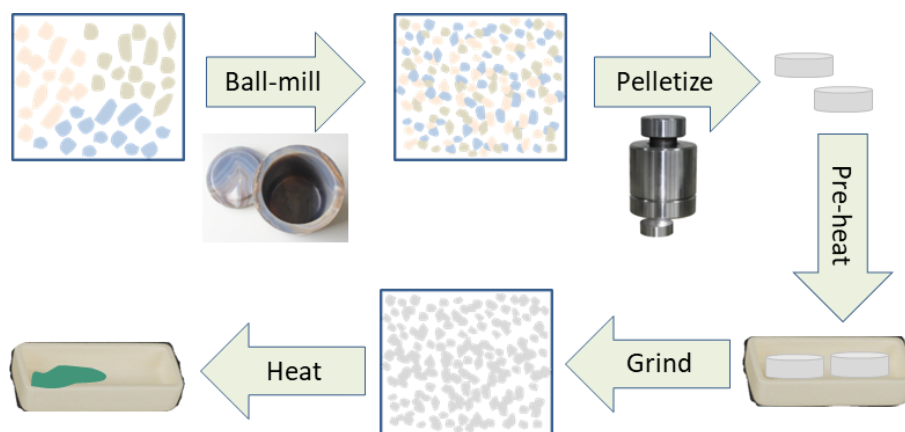


Figure 2-1 Schematic of the applied ceramic synthesis route to obtain the vanadium oxy-phosphate intermediate compounds.

The obtained vanadium oxy-phosphate materials were fluorinated through a consequent ceramic synthesis step. For this, stoichiometric amounts of the reactants including the intermediate oxy-phosphates and the fluorine-containing powder were weighed, mixed and well-ground using agate mortar and pestle. The powder was pressed as pellets with 100-150 weight in average (Figure 2-2). These pellets were then introduced inside of a stainless-steel reactor (autoclave) with ~2.5 mL inner volume. The reactor was sealed in the glovebox with an argon atmosphere in order to have a controlled atmosphere during the synthesis. The components of the reactor, involving the main cylinder, the cap, a copper ring (to help sealing) and a golden liner-tube are shown in Figure 2-3. The golden liner-tube was used in order to prevent the direct contact of pellets (or powders) with the stainless-steel body. The reactor was inserted in the furnace and heated at elevated temperatures. The synthesis temperature varied between 500 °C and 900 °C depending on the related experiment. The duration of the heating process usually varied between 30 min and 1 h. The reactors were quenched in liquid nitrogen after the end of heating process, unless otherwise indicated.

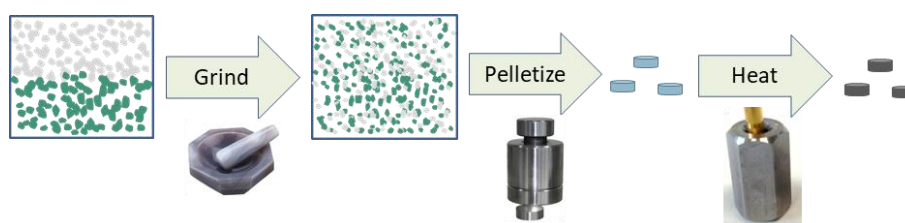


Figure 2-2 Schematic of the synthesis route for the fluorination process.



Figure 2-3 Stainless steel reactor (autoclave) and its components, used in the synthesis process.

2.2. Characterization Methods

To determine and evaluate the properties of the synthesized materials, several characterization techniques were employed in this work. A comprehensive structural and chemical information from the produced materials was obtained at both micro- and nano-scale. This helped in thorough understanding of the characteristics of each material in relation with their synthesis route and the involved mechanisms. The characterization techniques in this work involved X-ray diffraction, X-ray absorption spectroscopy, nuclear magnetic resonance spectroscopy, scanning electron microscopy, transmission electron microscopy, energy-dispersive X-ray spectroscopy, electron energy-loss spectroscopy and focused ion beam microscopy.

2.2.1. X-Ray Diffraction

The X-ray diffraction (XRD) is a non-destructive characterization technique for powders or solids to investigate their crystalline phases. This method is based on the scattering of incident beam of X-rays at specific angles relative to the atomic planes of a crystal. The specific diffraction angles are representative of the crystallographic structure of materials [Bragg, 1913]. Therefore, analyzing the XRD diffractogram helps in identification of crystalline phases with long-range order. Indexing the diffraction peaks allows determining the unit cell and the lattice parameters. An XRD-based Rietveld refinement can be used to solve the structural model and obtain the atomic parameters that define the crystal structure.

In this work, XRD patterns were acquired by means of two instruments. The first instrument was a D5000 Bruker diffractometer (Massachusetts, United States). The

measurements were carried out using a Cu $K\alpha_1$ radiation ($\lambda=1.5406 \text{ \AA}$) produced using 30 mA current and 40 kV tension. Data was recorded in the $10\text{--}80^\circ$ (2θ) with a step size of 0.04° at a counting time of 3 s per step.

The second instrument was a PANalytical X'Pert PRO diffractometer (from Malvern/Panalytical, United Kingdom) equipped with an X'Celerator detector (128 channels) using energy discrimination and Cu $K\alpha_1$ radiation ($\lambda=1.5406 \text{ \AA}$). The X-rays were produced using 40 mA current and 45 kV tension. Measurements were performed in $10\text{--}80^\circ$ (2θ) angular range with increments of 0.033° at constant counting time of 100 s per step. Measurements for high resolution data were conducted using the same X'Pert instrument in the $10\text{--}120^\circ$ (2θ) angular range with increments of 0.008° at a constant counting time of 550 s per step.

HighScore Plus software from Malvern/Panalytical [Degen, 2014] was used for identification of the phases in the synthesized materials. The lattice refinements were carried out using *Fullprof_suite* program [Rodriguez, 1990]. The crystal structure visualization was done using *Diamond* software (from Crystal Impact, Germany).

2.2.2. X-ray Absorption Spectroscopy

X-ray absorption spectroscopy (XAS) is a technique in which X-ray synchrotron radiation is used to obtain information about the local geometric and electronic structure of materials. The characteristic information can be obtained when X-rays are absorbed by an atom at energies near and above the core level binding energies of that atom. Each absorption edge is representative of a specific core-electron binding energy, which increases with increasing atomic number. XAS denotes the measurement of cross-section at absorption edges. The measurements can be performed either in transmission mode or fluorescence mode. The transmission mode often is used for concentrated samples, whereas the fluorescence mode is preferred for thicker samples or lower concentrations where higher sensitivity is required. A monochromator may be used to choose the X-ray energy during the measurements.

An XAS spectrum has two main features: X-ray absorption near-edge structure (XANES) and extended X-ray absorption fine structure (EXAFS). The XANES region is sensitive to coordination (local electronic and crystal structure) and valence state. The absorption edge moves to higher energies by the increase of valence state. An example

can be seen in Figure 2-4 for vanadium edge in different vanadium oxide samples, where the edge shifts to higher energies from V_2O_3 (V^{3+}) to V_2O_5 (V^{5+}). The EXAFS region is used for quantitative determination of bond length and coordination number. In addition to these features, the pre-edge region can also be descriptive of geometric features [Penner-Hahn 2019]. For instance, a higher structural symmetry implies a lower intensity in the pre-edge feature, such is the case for V_2O_3 in comparison to asymmetric V polyhedra in V_2O_5 .

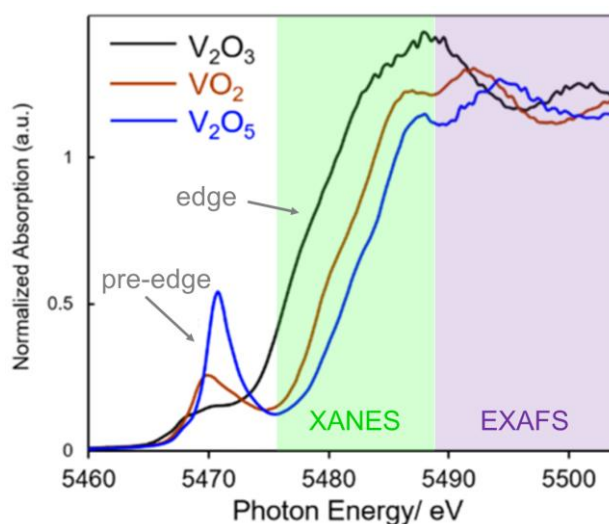


Figure 2-4 Features of an XAS spectrum for various vanadium oxide materials.

In this work, XAS was used for investigating the valence state and local geometry of vanadium atoms. Vanadium K-edge XANES spectra of vanadium (oxy/fluoro) phosphates and reference vanadium compounds with known vanadium valence state and structure were measured at room temperature in transmission detection mode at the XAFS beamline of the ELETTRA synchrotron radiation facility in Trieste, Italy, and at P65 beamline of PETRA III, DESY, Hamburg. A Si (111) double-crystal monochromator was used at both beamlines with energy resolution of about 0.7 eV at 6 keV. The intensity of the monochromatic X-ray beam was measured by using three consecutive ionization detectors, filled with appropriate nitrogen and argon gas mixtures to obtain 15% absorption in the first cell and 80% in the second and third cell. All the V-containing samples including reference compounds (*e.g.* V_2O_5 , VO_2F) were prepared in the form of homogenous pellets, pressed from micronized powder mixed with boron nitride powder. In all cases, the total absorption thickness of the sample was about 2 above the V K-edge. The absorption spectra were measured within the interval [-250 eV - 1000 eV] relative to the V K-edge. At the XAFS beamline, equidistant energy steps of 0.25 eV were used with

the integration time of 2 s/step in the XANES region. At P65 beamline, the absorption spectra were measured in continuous fast (3 min) scans and re-binned to the same energy steps in the XANES region as at XAFS beamline. Two to five repetitions of the scans were superimposed to improve the signal-to-noise ratio. The exact energy calibration was established with a simultaneous absorption measurement on a 5 micron thick V metal foil placed between the second and the third ionization chamber. The V K-edge in the V metal is at 5470.6 eV. Absolute energy reproducibility was ± 0.02 eV. The analysis of XANES spectra is performed with Demeter (IFEFFIT) program package [Ravel, 2005], in combination with FEFF6 program code [Rehr, 1992] for ab initio calculation of photoelectron scattering paths.

2.2.3. Nuclear Magnetic Resonance

Nuclear magnetic resonance (NMR) spectroscopy is used to probe the intrinsic spin properties of the atomic nuclei in samples. During the measurement, the sample is placed in a strong magnetic field, in which, excitation of the nuclei with radio waves promotes the transitions between nuclear energy levels (resonance) and produces the NMR signal. The resonance frequency depends on the magnetic field around the atoms. This, in turn, can reveal the details of the electronic structure. A nonzero nuclear spin is required for an atom to be detected by NMR. This is the case when the total number of protons and/or neutrons in the atom is odd, which gives them intrinsic nuclear magnetic moment and angular momentum. In solid-state NMR spectroscopy, special techniques such as magic angle spinning (MAS) are used to reduce the broadening of chemical shifts.

In this work, solid-state MAS-NMR was used in order to explore the local environment of phosphorous and lithium atoms in the structure. Solid-state ^{31}P and ^7Li MAS-NMR spectra were recorded on a 600 MHz Varian NMR system, operating at ^{31}P Larmor frequency of 242.65 MHz and ^7Li Larmor frequency of 232.97 MHz. Varian 1.6 mm HXY MAS probe head at sample rotation frequency of 40 kHz was used. ^{31}P MAS NMR spectrum of each sample was obtained as a sum of a series of spin-echo sub-spectra, recorded at different irradiation frequencies [Pell, 2013]. The irradiation-frequency step was 160 kHz. Durations of the first and the second pulse in the rotation-synchronized spin-echo experiment were 1.8 μs and 3.6 μs , respectively, and the delay between the pulses was 25 μs (*i.e.* one rotation period). Repetition delay between consecutive scans varied between 120 s (for irradiation frequencies close to 0 ppm) and 1 s (for irradiation

frequencies close to 600 ppm and beyond). Number of scans for each individual spectrum was 32 (when recorded with the repetition delay of 120 s) or 2400 (when recorded with the repetition delay of 1 s). The frequency axes of the ^{31}P MAS NMR spectra were reported relative to the signal of 85% H_3PO_4 . ^7Li MAS NMR spectra were obtained with spin-echo sequence, in which the durations of the first and the second pulse were 1.4 μs and 2.8 μs , respectively, and the delay between the pulses was 25 μs . Repetition delay between consecutive scans was 100 s, and number of scans was 24. The frequency axes of the ^7Li MAS NMR spectra were reported relative to the signal of Li_2SiO_3 (0 ppm).

2.2.4. Scanning Electron Microscopy

Scanning electron microscopy (SEM) is generally used for morphological studies and compositional analysis of materials. The working principle of SEM is to scan the surface of the samples with a finely focused electron beam, during which electrons interact with the atoms of the sample and produce various signals. These signals include secondary electrons (SE), backscattered electrons (BSE), auger electrons, characteristic X-rays, fluorescent X-rays and visible light (cathodoluminescence). SE and BSE signals are commonly used for imaging purpose [Goldstein, 1981][Zhang, 2008].

In this work, a field-emission scanning electron microscope (FE-SEM, Model SUPRA 35VP, Carl Zeiss, Germany) was used to characterize the size and morphology of the powder samples. Secondary electron images were formed using the electron beam with acceleration voltage of 1 keV.

2.2.5. Transmission Electron Microscopy

Transmission electron microscopy (TEM) is a microscopy technique in which high-energy electrons (*e.g.* 80 keV) are irradiated onto a specimen. TEM can reveal the finest structures and in some cases individual atoms within a sample. Features such as crystal structure, defects, quantum well, chemical composition etc. can be studied by TEM. In this technique, the electron beam strikes the sample and parts of it transmits depending on the thickness and electron transparency of the sample. Similar to SEM, several signals are formed due to the interaction of electron beam with sample. Most of the signals are formed by energy or phase change in the interaction. The specimen is often nano-sized particles or an ultrathin section with thickness less than 100 nm.

A scanning transmission electron microscope (STEM) differs with the conventional TEM in the shape of the beam. In STEM, the lenses are adjusted to create a convergent fine-focused beam, as opposed to conventional TEM, in which, a beam parallel to the optical access illuminates the sample. The rastering of the beam over the specimen in STEM mode makes it suitable for analytical techniques such as Z-contrast annular dark-field imaging, and spectroscopic mapping by energy dispersive X-ray spectroscopy, or electron energy loss spectroscopy. These signals can be acquired simultaneously which then allows a direct correlation of images and spectroscopic data [Williams, 1996].

In this work, selected area electron diffraction (SAED) technique was employed for the structural analysis of the synthesized materials in transmission electron microscope. Atomic structure of synthesized materials was studied by means of high-resolution scanning TEM high-angle annular dark field (STEM-HAADF) and annular bright field (STEM-ABF) imaging. For these analyses, a probe aberration-corrected JEM-ARM200CF equipped with JEOL STEM detectors (JEOL, Tokyo, Japan) was employed. The applied accelerating voltage for all the measurements was 80 keV. Specimens for electron microscopy analysis were prepared in two ways: (1) by focused ion beam (FIB) milling of a lamella from a single particle and (2) by drop casting the powder particles, which were dispersed in isopropanol on TEM Cu-grid.

2.2.6. Spectroscopic techniques in TEM

Energy dispersive X-ray spectroscopy (EDX or sometimes EDS, EDXS) and electron energy-loss spectroscopy (EELS) are both powerful analytical microscopy techniques. They enable qualitative and quantitative compositional analyses, elemental mapping, and electronic property analysis of both crystalline and amorphous materials. The signals used in these techniques are caused by inelastic scattering of electrons (involves loss of energy) as they pass through the specimen.

EDX uses characteristic X-rays created when high-energy electrons of the beam eject inner shell electrons from their orbitals in the sample. Following this, the ionized atoms go back to their lowest energy states by replacing the missing inner shell electrons by the outer shell electrons. This process results in the emission of an X-ray characteristic of the electron shell energy; thereby providing a unique signature for the atom present in the sample.

EELS looks at the energy distribution of the electrons that have undergone inelastic scattering when passing through the sample. An EEL spectrum of Si is shown in Figure 2-5. Low energy losses *i.e.* valence loss (< 50 eV) usually correspond to electrons that have interacted with the weakly bound outer-shell electrons of the atoms and provide information about the electronic and optical properties of the material. High losses *i.e.* core losses (> 50 eV) are related to electrons that have been scattered by the inner electron shells and so have characteristic information of the atoms. The onset position of ionization edges at high-energy losses is characteristic of atoms present in the sample. The fine structure of the ionization edges can provide information on chemical bonding, oxidation state and atomic configurations.

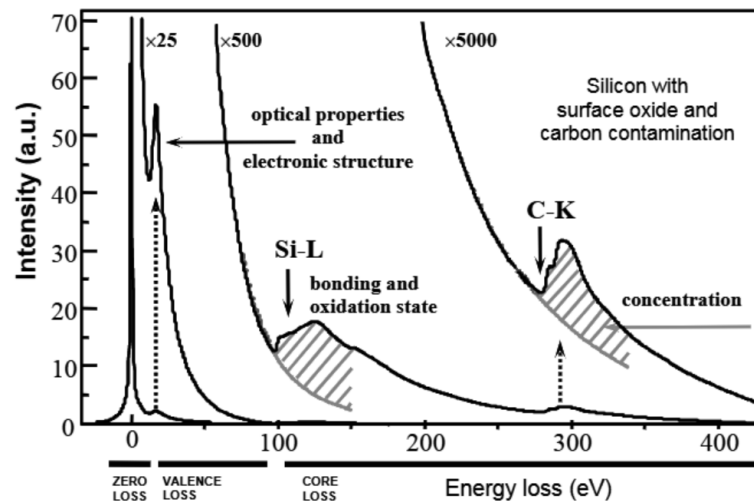


Figure 2-5 EELS spectrum of Si, showing various information at different energy scales [Duscher, 2019]

In this work, elemental distribution was assessed by standardless energy dispersive X-ray spectroscopy in STEM mode (STEM-EDX), while electronic structure was studied by EELS. For these analyses, a JEOL Centurio 100 mm² EDXS detector and Gatan GIF Quantum ER spectrometer (Gatan, Pleasanton, USA) installed on a probe aberration-corrected JEM-ARM200CF was employed.

2.2.7. Focused Ion Beam

Focused ion beam (FIB) is a technique which uses a beam of heavy ions, typically Ga⁺, to sputter atoms from a target surface. Therefore it can be used for several applications such as milling, surface polishing, slice and view, micromachining and manipulation, and TEM sample preparation [Stevie, 2005]. A dual-beam system incorporates ion beam

(FIB) and electron beam (SEM) for a simultaneous sample preparation and imaging purpose.

In this work, FIB instrument was used for preparation of thin lamella for TEM analysis. The sample preparation involved several steps. Figure 2-6 presents some images of the lamella preparation procedure. Firstly, the powder sample was deposited on the carbon paste and was coated with a layer of carbon to enhance the electrical conductivity in interaction with electron and ion beam. Then, a particle with a diameter of $\sim 25 \mu$ was chosen as the target sample, since lamella preparation from powder particles can only be applied for particles larger than 20μ . Platinum layers were deposited on top of the particle to prevent gallium implantation. Then, ion milling was applied until forming a 1-2 micron thick cross-section sample. For the lift-out step, a micromanipulator was glued to the sample and the shoulders were cut to free the sample for the next step. The freed section was then mounted on a TEM grid using Pt deposition, and the sample was thinned by ion milling until a thin lamella (below 100 nm) was formed. For this processes, a Helios NanoLab 600i Dual-beam system (Thermo Fisher Scientific, Waltham, USA, previously FEI company) was used.

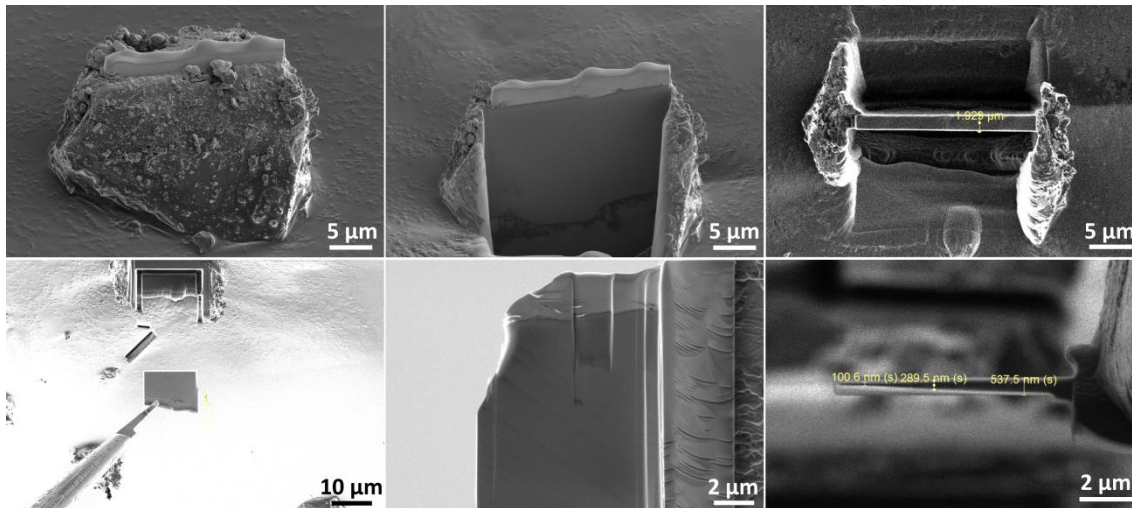


Figure 2-6 The preparation process of a lamella from a synthesized particle using FIB for TEM analysis.

2.3. Electrochemical Measurements

Electrochemical tests were performed to evaluate the electrochemical characteristics of the synthesized materials in lithium ion batteries. Each LIB cell is typically composed of

a positive electrode, a negative electrode and an electrolyte as the main components. The synthesized materials act as the active material of the positive electrodes in a LIB cell. Here, firstly the positive electrode (cathode) preparation is described and then assembling the LIB cells and the electrochemical tests are discussed.

2.3.1. Positive Electrode Preparation

Cathode composite electrodes are generally composed of active material, conducting agent (*e.g.* carbon black) and polymer binder. The amount and type of each component may vary depending on the related experiment and the properties of the components. In this work, the composite electrodes were prepared using 75 wt% of active material (synthesized materials), 15 wt% of carbon black Printex (from Degussa) and 10 wt% of PTFE (dissolved in water) as the binder. The materials were mixed together with isopropanol, either by planetary ball-milling at 300 rpm for 30 min or by hand-grinding using agate mortar and pestle. The obtained slurry was then cast onto carbon-coated aluminum mesh or scratched aluminum foil (Figure 2-7 a). The aluminum mesh or foil act as the current collector in the positive side of a battery cell. Circular electrodes with a diameter of 12 mm or 14 mm were punched, pressed at ~ 200 MPa, and dried overnight at 80 °C (Figure 2-7 b and c). The typical loading of active material in electrodes was ~ 2 mg/cm².

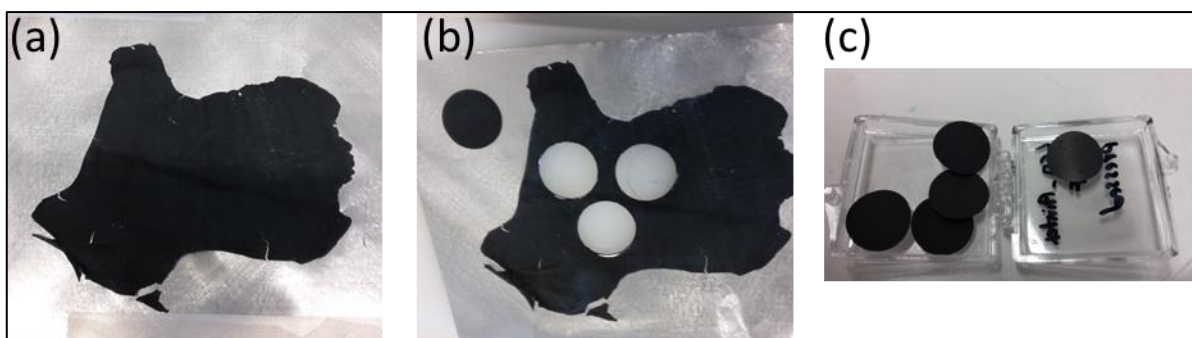


Figure 2-7 Preparation of cathode electrodes from a slurry; (a) casting on an Al foil, (b) cutting circular electrodes using punch and (c) cut and dried electrodes, ready for battery assembling.

Figure 2-8 shows the typical microstructure of a composite electrode including the active material particles (A), carbon Printex particles (C) and PTFE binder (B) under SEM at two different magnifications. A homogeneous distribution of components and good

contact between them is important in performing the optimum electrochemical measurements.

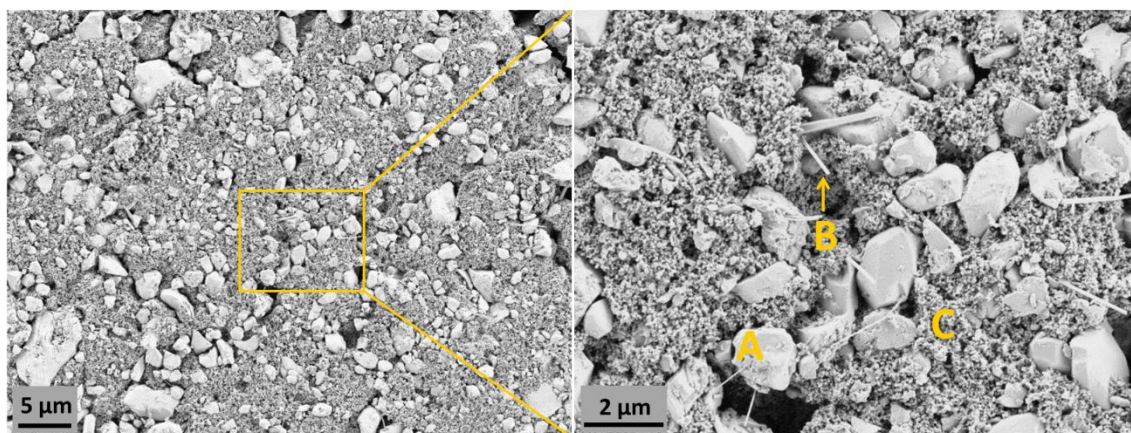


Figure 2-8 SEM micrographs of prepared composite electrode, (a) at low magnification, showing the overall view and (b) at high magnification, showing various components; A: active material particle, B: binder (PTFE) and C: carbon *Printex* particles.

2.3.2. Battery Assembly

The prepared electrodes were used in battery cells to test the electrochemical properties of materials. Generally, four common laboratory-scale cells are used for testing different battery chemistries: beaker cell, coin cell, Swagelok cell and pouch cell (coffee-bag cell). Figure 2-9 shows the different measurement cells with their parts for battery systems. Choice of each cell type is dependent on the type of measurement and the interested characteristic under study, and may have advantages and drawbacks. For example, a beaker cell is suitable for simple laboratory tests and it is easy to assemble but it requires a lot of electrolyte and the whole measurement should to be carried out inside of the glovebox.

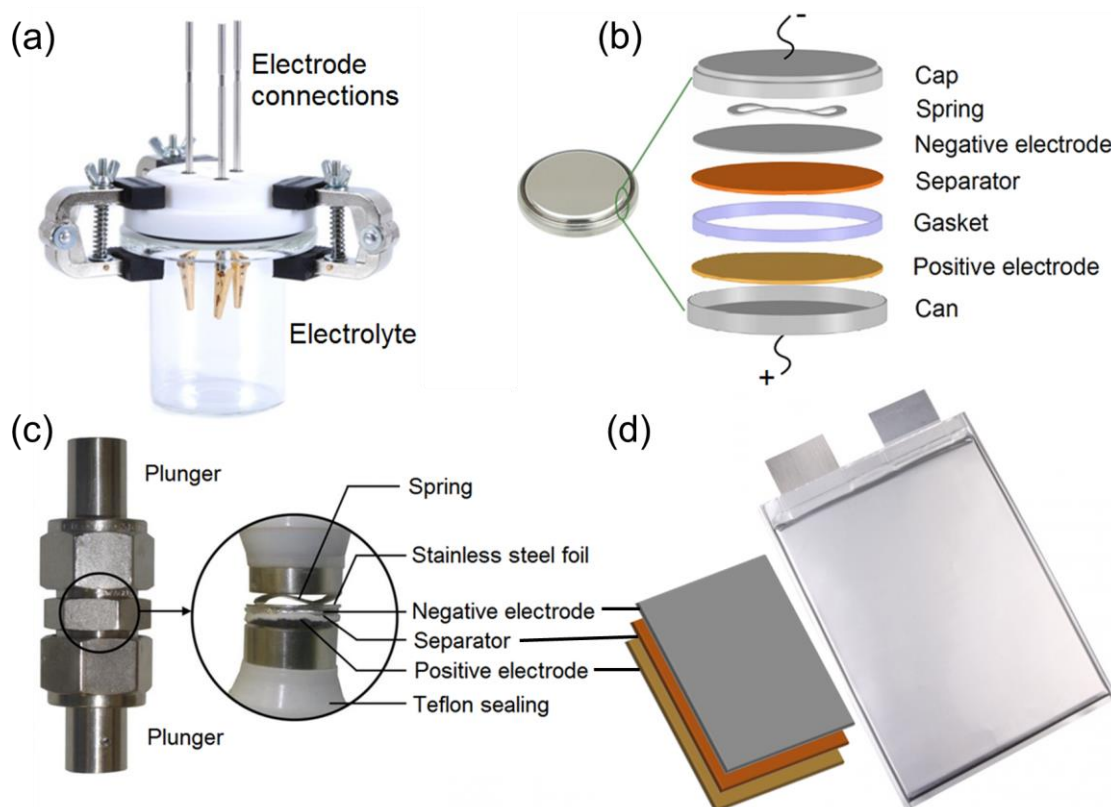


Figure 2-9 Various battery testing cells: (a) beaker cell, (b) coin cell, (c) Swagelok cell and (d) pouch cell (coffee-bag cell), showing their components.

For testing battery materials, especially the newly developed ones, reliable electrochemical setups are essential for evaluating their basic properties. In any electrochemical measurement, the electrode under study, *i.e.* where the reaction of study occurs, is called a working electrode (WE) and the other auxiliary electrode is called a counter electrode (CE). A reference electrode (RE) is an electrode which provides a constant, stable reference potential against which the potential of WE can be determined. The tested battery can be assembled in either two-electrode or three-electrode cell configuration. In a two-electrode cell, the CE also acts as RE. The specific capacity (*i.e.* the total amount of charge that can be stored per unit of volume or mass) and the cell voltage are usually measured in a two-electrode configuration during discharge and charge processes. A three-electrode configuration, with an additional reference electrode (RE), is usually used when the effect of each individual cell component to overall battery performance is to be studied. An RE also enables a quantitative evaluation of various electrochemical aspects during the battery operation. For Li-ion cells, a two-electrode half-cell configuration with composite electrode as WE and Li metal electrode as both CE and RE is the typical standard setup for laboratory-scale tests. Half-cell setup is as

opposed to a full-cell, in which the CE (negative electrode in this case) is a carbonaceous material. In conventional cells, a separator soaked with electrolyte solution sits between the WE and the CE in order to prevent short circuit between these two electrodes. The electrodes are electronically connected to outer circuit by electrode terminals through current collectors (e.g. Al and Cu foils for positive and negative electrodes, respectively).

In this work, the electrochemical measurements were performed in half-cell configuration using either coffee-bag cells (Figure 2-9c) or Swagelok cells (Figure 2-9 d). A *Whatman* glass microfiber separator separated the WE (composite electrode) and the CE (metallic Li foil). The separator was soaked with the LP40 commercial electrolyte from *Merck*, which is a 1 M solution of LiPF_6 salt in EC:DEC solvent in a 1:1 volume ratio. Typically, 20 drops of electrolyte was used to soak the separator. All of the test cells were assembled in an argon-filled glovebox.

2.3.3. Electrochemical tests

The assembled battery cells can be tested with various electrochemical testing methods, depending on the parameter under study (such as potential-composition relation, potential stability window, kinetics, etc.). Typical electrochemical characterization techniques include cyclic voltammetry (CV), galvanostatic cycling (GC), galvanostatic or potentiostatic intermittent titration techniques (GITT or PITT), and electrochemical impedance spectroscopy (EIS).

Both potential-controlled techniques (such as CV) and current-controlled techniques (such as GC) enable the study of various reactions at battery electrodes and measurement of battery capacity by inducing large perturbations which could drive the electrodes far from equilibrium. CV and GC are the two base techniques employed to test active materials. In CV, a potentiostat is used to adjust the current between WE and CE in order to reach the desired potential difference between WE and RE. Then, the resulting current flow between WE and CE is recorded as a function of potential or time. In GC, a galvanostat is used to apply a constant positive or negative current between WE and CE, and the evolution of cell potential is recorded as a function of time. In galvanostatic cycling, usually voltage limitations are applied under current for both charge (positive current) and discharge (negative current). The charge/discharge is performed until potential reaches a set value, at which point the direction of the reaction changes.

Processing such results enables the monitoring of potential evolution versus the number of moles of mobile species (*e.g.* Li⁺). In battery tests, GC measurement is usually preferred over CV since they it can produce much more useful data over a narrow voltage range. The battery capacity can also be measured with much higher precision using GC.

GITT and PITT techniques consist of stepwise variation of capacity and potential in small amounts, respectively, and relaxation periods. These two techniques serve two main purposes, which are obtaining the potential as a function of composition in conditions close to equilibrium and determining the diffusion coefficient of the cation inside the active material. EIS is also a widely-adopted technique in investigating battery materials. It is based on the concept of the opposition to current flow induced by various battery components when the cell is operated under an alternating current (AC) signal. The impedance is measured as a function of the frequency of the AC signal, which enables separation of various processes occurring with different time constants within the cell. EIS can provide information about various processes occurring in the electrochemical cell, such as mass transfer in the electrolyte or through a solid-electrolyte interface (SEI), charge transfer and diffusion [Raccichini, 2019][Dugas, 2019].

The applied current in GC is determined based on the theoretical capacity (Q) of the active material and the C-rate. The input current is calculated by multiplication of these two parameters ($Q \times \text{C-rate}$). The C-rate is a measure of the rate at which a battery is discharged. For instance, a 1C rate means that the discharge current will discharge the cell in 1 hour. The capacity of a battery is the amount of available electric charge expressed in ampere-hours (Ah) and it represents the specific energy in Ah units. The capacity of a cell is related to the quantity of active material used in the electrode. The theoretical specific capacity of a battery can be calculated by Faraday's law (Equation 2-1):

$$Q_{\text{theoretical}} = (nF) / (3600 * M_w) \text{ mAh/g} \quad \text{Equation 2-1}$$

Where n is the number of charge carrier (e⁻), F is the Faraday constant (96,500 C/mol) and M_w is the molecular weight of the active material. Therefore, in principle, lighter materials can have higher capacity. The practical specific capacity of a cell can be different from the theoretical one and it is calculated by the potential-time curve from the galvanostatic cycling test (Equation 2-2):

$$Q_{\text{practical}} = (i \cdot A \cdot t_{\text{cutoff}}) / (3600 \cdot M_w) \text{ mAh/g} \quad \text{Equation 2-2}$$

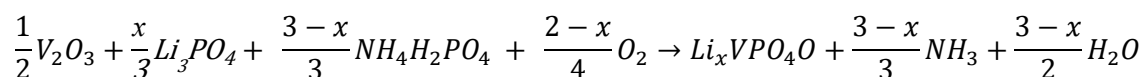
Where i is the current density (A/m^2), A is the area (m^2) and t_{cutoff} is the time (s) to reach the cut off potential (V_{cutoff}). The practical capacity depends on the used C-rate and voltage range in the measurement. The reason why practical capacity is usually lower than theoretical capacity is that not all the Li can be removed from the lattice of the host active material.

In this work, the electrochemical behavior of the half-cell batteries were measured using galvanostatic cycling technique. For this, a “VPM3” (*Bio-Logic*) potentiostat/galvanostat device running with *EC-Lab*[®] software was employed. A current density was applied on the electrodes within certain voltage ranges calculated from the theoretical capacity of the related active material. A C-rate of C/50 was used in all the measurements. This meant that the necessary current was applied or drained from the battery to completely charge or discharge it in 50 h. The cells were cycled between 3 V and 4.5 V vs. Li/Li⁺ when the cycling test was aimed to start with charge (oxidation, extraction of Li⁺ from the active material) and they were cycled between 3 V and 1.50 V vs. Li/Li⁺ when the cycling started with a discharge (reduction, insertion of Li⁺ into active material).

CHAPTER3: VANADIUM OXY-PHOSPHATE INTERMEDIATE PHASES

In this chapter, synthesis, characterization, crystal structure and electrochemical performance of the intermediate vanadium oxy-phosphate phases (β -VPO₄O, ε -LiVPO₄O and β -LiVPO₄O) is discussed. These materials were prepared by solid-state synthesis method. A general reaction according to Equation 3-1 was employed for the synthesis of β -VPO₄O and ε -LiVPO₄O phases. This reaction is based on the oxidation of vanadium (starting by vanadium(III) oxide precursor) to a higher oxidation state.

Equation 3-1



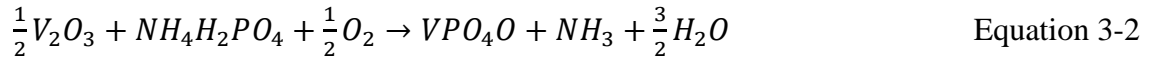
Additionally, vanadium(V) oxide (V₂O₅) was used as the vanadium-containing precursor to obtain β -LiVPO₄O and β -VPO₄O (through a second route).

3.1. β -VPO₄O

β -VPO₄O was chosen among the VPO₄O polymorphs due to its 3D network with an open tunnel structure, higher stability and higher operating potential (3.95 V) compared to the other polymorphs. The synthesis route to obtain β -VPO₄O and the related characterization, its crystal structure and the electrochemical properties are discussed in this section.

3.1.1. Synthesis and Characterization

The synthesis of β -VPO₄O was carried out by two different sets of precursors. In the first method, stoichiometric amounts of vanadium(III) oxide and monobasic ammonium phosphate precursors were mixed according to equation 3-2:



The mix was ball-milled for 12 h at 600 rpm in a planetary ball-milling machine and then pellets were pressed. A thermal pre-treatment was performed in order to remove ammonia [Viswanath, 1979]. The pellets were heated at 300 °C for the duration of 8 h under argon flow and then reground back to powder. This powder was heat-treated at various conditions (temperature and time) in order to obtain a pure VPO₄O (abbreviated as VPO). As mentioned in Chapter 1, this compound has at least 7 known polymorphs. Obtaining a pure single phase is very difficult and the polymorphs usually tend to stabilize in the same conditions due to their close formation energies. The XRD results of materials calcined ex-situ at various temperatures and heating durations are shown in Figure 3-1. The XRD pattern of the unheated mix of V₂O₃ and NH₄H₂PO₄ precursors is also presented (marked as w/o heating). At 500 °C, the peaks related to these precursors disappeared and a new phase started to form. Heating at higher temperatures and/or longer durations resulted in formation of various phases. Indeed, in most of the conditions, mixes of several phases including VPO polymorphs and impurities were present. The phase transformations can be followed from the changes in the XRD patterns of the products at various conditions. For example, the phase formed at 500 °C and 1 h heating decreased in amount by heating at 500°C and 12 h (example of related peak at 22°). By heating the precursor mix at higher temperatures of 600 °C and 700 °C, peaks of a new phase appeared (e.g. at 18° and 23°). This phase, too, disappeared at 740 °C and a single high-temperature phase formed. It should be mentioned that the batch melted above 750 °C.

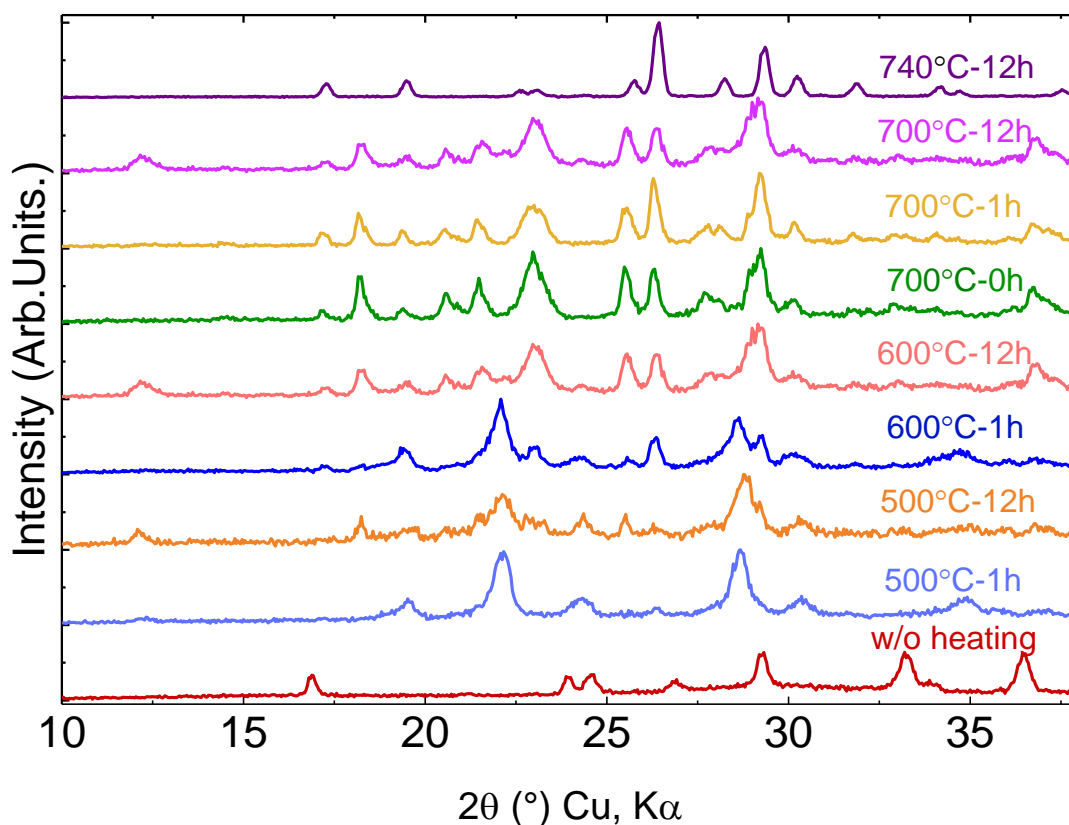


Figure 3-1 XRD patterns of products obtained through heat-treatment of the mix ($V_2O_3+NH_4H_2PO_4$) at various temperatures and times. w/o heating refers to the mix of precursors prior to any heat treatment.

Three of the polymorphs that were formed as the main phases during the heating experiments are shown in Figure 3-2. At 500 °C-1 h, the low-temperature δ -VPO phase was formed. The XRD pattern is in accordance with the ICSD card No. 420073. The δ -VPO has a tetragonal unit cell with a space group $P4_2/mbc$ (N°135) [Girgsdies, 2009]. By increasing the sintering temperature to 700 °C and quench at air, γ -VPO phase was formed. The XRD pattern matches with ICSD card No. 415213. The γ -VPO phase has an orthorhombic lattice with a $pbam$ space group (N°55). Simultaneously, peaks of another orthorhombic polymorph, β -VPO, also appeared (marked by asterisks on the 700 °C pattern). Heating at temperatures as high as 740 °C for longer durations (*e.g.* 72 h) resulted in stabilization of the β -phase solely.

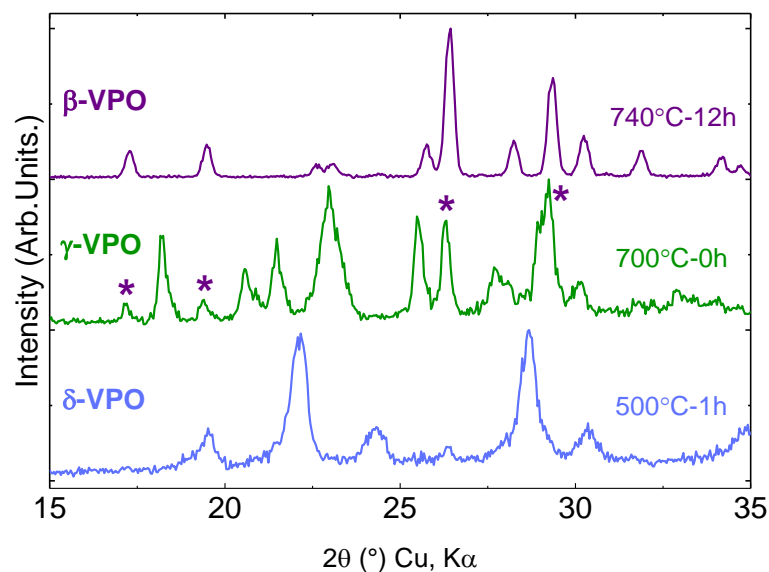


Figure 3-2 XRD patterns of some of formed VPO polymorphs at various heat-treatment conditions. The purple asterisks on γ -VPO (700 °C-0h) pattern mark the β -VPO (impurity) peak positions.

Nevertheless, obtaining pure phase remained a challenge. For instance, heat treatment at similar conditions of same reactants prepared in various batches could lead to various results. XRD patterns of three batches (composed of the same reactants), heat treated at 700 °C-12 h are shown in Figure 3-3a. The main phase in all three products was β -VPO, but additional peaks also appeared which mostly belong to other VPO polymorphs (marked by asterisks). In some cases, even heating the same batch in similar conditions could lead to different results. This is shown in Figure 3-3b, where various impurity peaks have appeared on the XRD patterns of the products heat-treated at 700 °C-12 h.

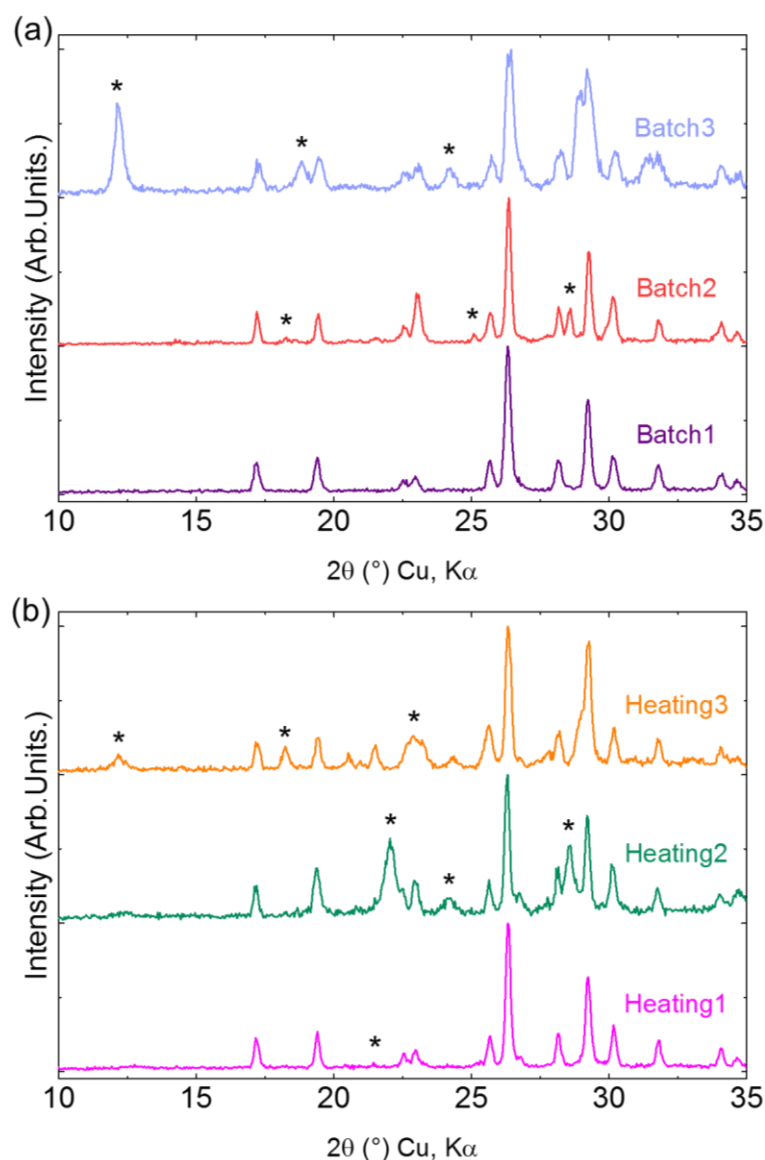


Figure 3-3 XRD patterns of the products obtained in similar calcining conditions of 700 °C-12 h from same reactants; (a) different batches and (b) same batch. The main phase is β -VPO and the asterisks mark the position of impurities.

Observations showed that in addition to heating duration, heating rate could also affect the VPO product. Figure 3-4 shows that heating at low rates (0.5 °C/min) lead to synthesis of a highly-crystalline pure β -VPO phase with a smooth yellow-colored appearance. However, heating at a higher rate of 5 °C/min resulted in formation of β -VPO with lower crystallinity as well as impurities and with a spongy darker appearance. This may be attributed to the diffusion of gas formed during the synthesis. In a higher heating rate, the gas molecules do not have enough time to escape and therefore get trapped in the material and could result in such an appearance.

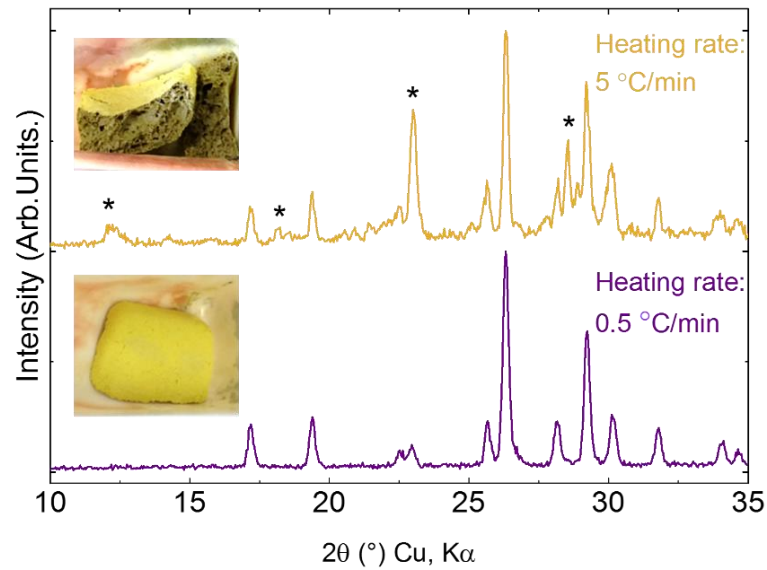
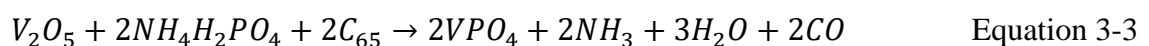


Figure 3-4 XRD patterns of the products obtained after heat-treatment at 700 °C-12h with 0.5 °C/min and 5 °C/min. Asterisks mark the impurities.

Albeit with significant difficulties, obtaining pure β -VPO phase using V_2O_3 precursor was possible. Although, the conditions for an optimum synthesis could vary, heating at 740 °C for at least 12 hours, or heating at 700 °C with a slow heating rate of 0.5 °C/min mostly resulted in a pure β -VPO phase. However, a second synthesis route was also investigated in this work, in order to find a faster and more reliable phase formation method.

In the second method, firstly vanadium phosphate (VPO_4) compound (with 3+ as vanadium oxidation state) was produced and then was oxidized to obtain VPO_4O (β -VPO with 5+ as vanadium oxidation state). The VPO_4 compound was synthesized via a carbothermal reduction (CTR) route. CTR is a solid-state synthesis method in which a highly divided carbon is used to reduce the oxidation state of a transition metal, in this case vanadium [Ellingham, 1944]. For this purpose, stoichiometric amounts of vanadium(V) oxide (V_2O_5 from Aldrich), ammonium phosphate monobasic ($NH_4H_2PO_4$ from Aldrich) and super C_{65} carbon were mixed according to Equation 3-3 [Barker, 2003]:



To ensure the complete vanadium reduction and also to have residual carbon in the final product, C_{65} was used 10 wt.% in excess. The precursors were mixed and ground in planetary ball milling inside an agate jar for the duration of 15 h at 600 rpm. The black-

colored mixed batch was then pressed as pellets and pre-treated at 300 °C for 8 h under Ar flow in quartz tube. Then, the pellets were ground to obtain a well-mixed batch prior to be pressed as pellets, again. These pellets were then heat-treated at 800 °C for the duration of 12 h under Ar flow. The XRD pattern of the obtained material is shown in Figure 3-5. This VPO₄ material has orthorhombic structure described in the space group Cmc₂m (N° 63).

The obtained VPO₄ was heat-treated under air in order to oxidize the vanadium and produce VPO₄O, according to Equation 3-4:



The XRD patterns related to calcining at three temperatures (500-600-700 °C) for the duration of 12 h are also shown in Figure 3-5. We can see that at 500 °C, the β-VPO already started to form and at 700 °C, a highly pure and crystalline β-VPO phase was obtained. This method proved to be much more straightforward in obtaining the desired pure material, although in essence it included another step (production of VPO₄) in the synthesis, which made the process a bit longer.

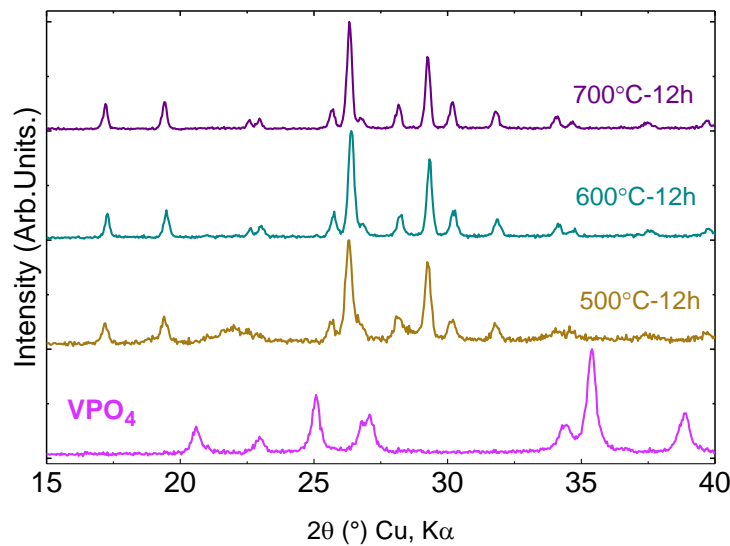


Figure 3-5 XRD patterns of VPO₄ and the products obtained through oxidation at 500-600-700 °C.

The microstructure of the obtained β-VPO phase was examined using SEM. Figure 3-6 shows the SEM images of the well-crystallized particles of β-VPO obtained at 700 °C at two different magnifications. We can see in Figure 3-6a that the powder formed as big agglomerations (>20 μm) of smaller particles. At higher magnification (Figure 3-6b),

particles with average size of 1-2 μm with pebble-like morphology mostly with not well-defined crystal shapes were observed.

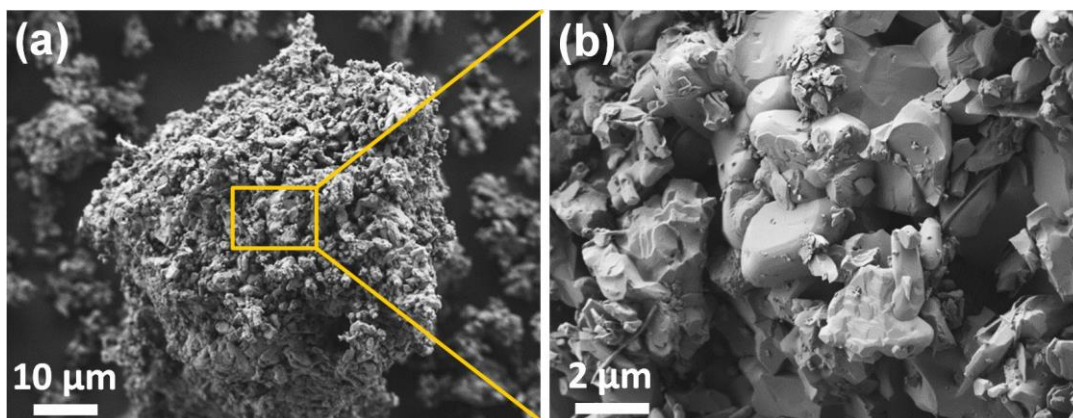


Figure 3-6 SEM micrographs of the β -VPO particles obtained at 700 $^{\circ}\text{C}$, (a) at low magnification, showing the agglomerate and (b) at high magnification showing the single particles.

3.1.2. Crystal Structure

β -VPO polymorph has an orthorhombic structure with $Pnma$ space group ($N^{\circ}62$). The fullpattern refinement matching of the XRD pattern of the phase using the LeBail method was carried out using the reported lattice parameters of β -VPO (ICSD No. 9413) and it is presented in Figure 3-7. The inset shows the yellow-colored as-synthesized powder. The refined lattice parameters are presented in Table 3-1.

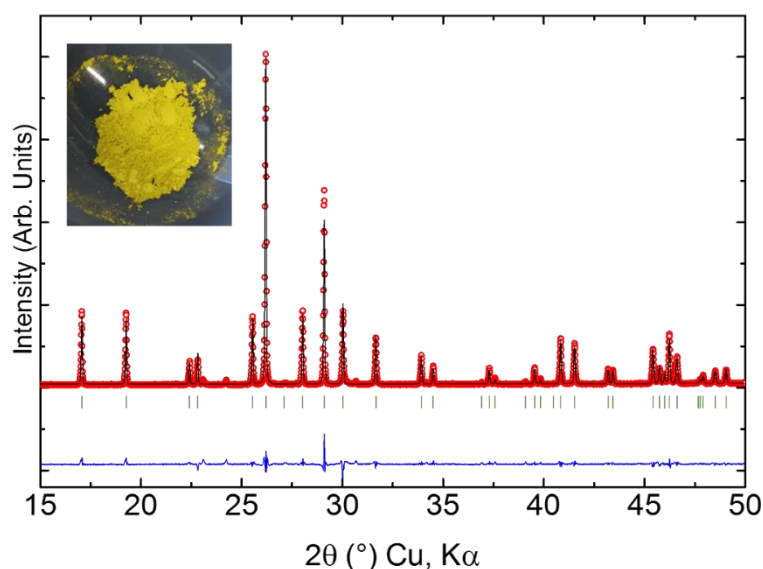
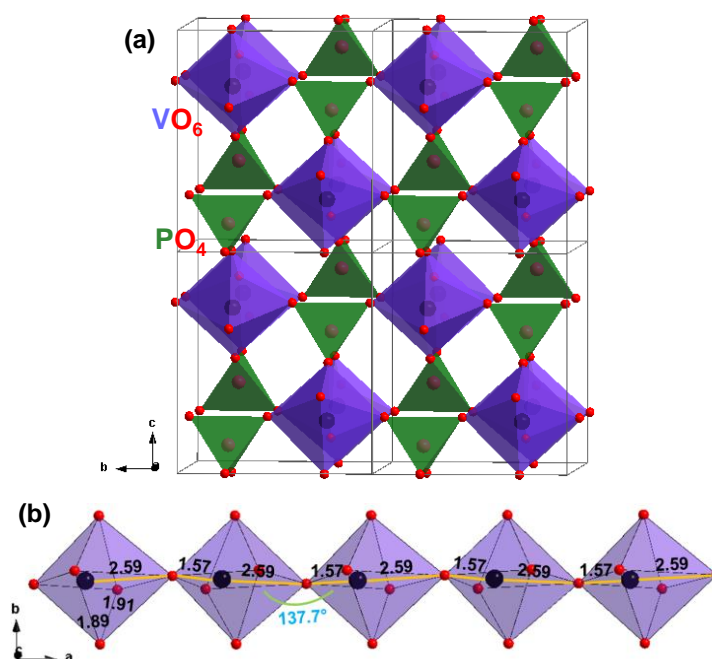


Figure 3-7 Fullpattern refinement matching of β -VPO XRD pattern using LeBail method. The observed, calculated and difference curves are presented as red dots, black line and blue lines, respectively. The Bragg positions are shown as green lines. The inset shows the synthesized powder.

Table 3-1 Refined structural parameters of synthesized β -VPO.

a (Å)	b (Å)	c (Å)	α (°)	β (°)	γ (°)	V (Å ³)
7.785(5)	6.130(7)	6.969(8)	90.00	90.00	90.00	332.412

As the generally-described structure for vanadium oxy-phosphates, β -VPO is formed of interconnected corner-sharing VO_6 octahedra and PO_4 tetrahedra (Figure 3-8a). The distorted VO_6 octahedra form infinite chains arrayed parallel to a axis. There is one long V-O and one short V=O bond which alternate along the a direction on the chain (Figure 3-8b). The other four V-O bonds are in bc planes and are corner-shared with four PO_4 tetrahedra. On the other hand, the PO_4 group shares its oxygens with four separate VO_6 groups in three separate chains and also makes additional bridges in the same octahedral chains, all together forming the 3D framework. The distortion in VO_6 groups is primarily due to displacement of V atoms from the center of octahedron towards one oxygen on the chain, which creates the alternative long and short bonds. These axial bonds are in the order of 1.57 Å and 2.59 Å in length, while the equatorial V-O bonds are ~ 1.88 Å. The average P-O bond length is in the order of 1.52 Å. β -VPO differs from other polymorphs in orientation of VO_6 octahedra and this, results in small differences of bond length and angles between octahedra. Upon lithiation, Li atoms enter the only available octahedral site, which is the 4a position of $Pnma$ space group. [Gopal, 1972][He, 2016] [Ni, 2018] [Chen, 2014] [Launay, 2003]

**Figure 3-8** Representation of crystal structure of β -VPO, (a) interconnection of VO_6 octahedra and PO_4 tetrahedra, (b) VO_6 octahedral chain.

3.1.3. Electrochemical Behavior

The lithium insertion/extraction into/from VPO relies on the reversibility of the V^{5+}/V^{4+} redox couple with a theoretical capacity of 165 mAh/g. The related electrochemical reaction can be described as Equation 3-5.



The galvanostatic charge/discharge (Li insertion/extraction) signature of β -VPO was investigated by testing it as cathode material in a half-cell battery. Figure 3-9 shows the galvanostatic cycling curve of β -VPO in the second cycle, at the high-voltage range (3.0-4.5 V vs. Li/Li⁺) with a current density corresponding to C/50 cycling rate. A flat plateau is observed at ~3.97 V involving V^{5+}/V^{4+} redox couple, which is in good agreement with the literature [Azmi, 2003]. According to Gibbs phase rule, this region implies a two-phase mixture *i.e.* a biphasic reaction. About 0.6 Li was exchanged during insertion/extraction of Li from the structure. Therefore, the charge capacity is about 100 mAh/g, which leads to 397 Wh/kg specific energy. Note that, according to Gaubicher *et al.*, the main framework of β -VPO structure is preserved upon lithiation and only a small distortion corresponding to 1% volume increase is induced [Gaubicher, 1999].

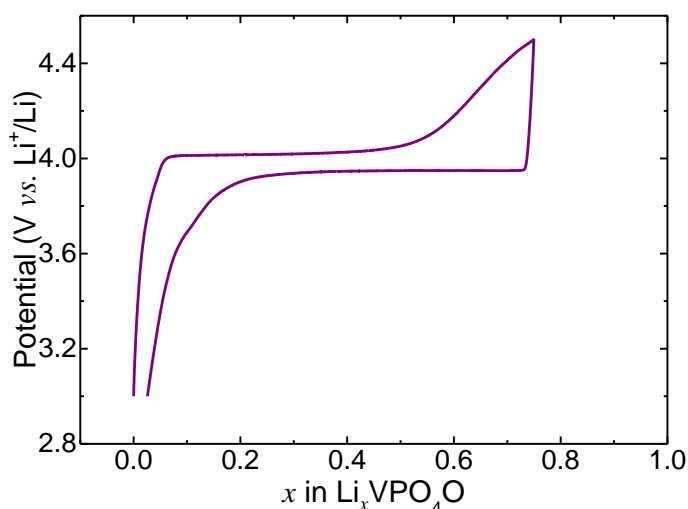


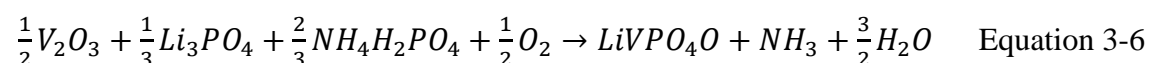
Figure 3-9 Galvanostatic cycling curve of β -VPO at second cycle at high-voltage range (3.0-4.5 V vs. Li/Li⁺) with a current density corresponding to C/50 cycling rate.

3.2. ϵ -LiVPO₄O

Among the lithium vanadyl phosphate phases, two polymorphs, namely ϵ -LiVPO₄O and β -LiVPO₄O were synthesized in this work. α_1 -LiVPO₄O polymorph was excluded due to the difficulties encountered during synthesis. In this section, synthesis of ϵ -LiVPO₄O, the related characterization, its crystal structure and the electrochemical performance is described.

3.2.1. Synthesis and Characterization

The synthesis of ϵ -LiVPO₄O was carried out by a one-step solid state synthesis according to the method described by Ateba Mba [2013]. Stoichiometric amounts of vanadium(III) oxide (V₂O₃), monobasic ammonium phosphate (NH₄H₂PO₄) and lithium phosphate (Li₃PO₄) were mixed according to Equation 3-6:



The mix was ground in an agate jar (or else zirconia jar) using a planetary ball milling machine for 12 h at 600 rpm and then the mixture was pressed as pellets. The color of the mixture after ball-milling depended on the utilized jar, where it was black or grey using agate jar and zirconia jar, respectively. It is assumed that zirconia could partially oxidize the V precursor. This could possibly affect the synthesis product properties. These pellets were pre-treated at 300 °C for 8 h under argon flow to remove ammonia. After the heat treatment, pellets were ground to obtain a homogenized powder, which was then heated at various conditions (time or temperature) under air to obtain LiVPO₄O (abbreviated as LVPO in this work).

The XRD results of the calcination at various conditions on the same batch (ground in agate jar) are shown in Figure 3-10. The XRD pattern of the unheated mix of reactants is also shown (marked as w/o heating). The ϵ -LVPO phase started to form already at 500 °C with calcination duration of 1 h. At higher temperatures and longer calcination durations the phase remained stable. However, a comparison of the main peak positions on the patterns shows that interestingly the peaks tend to shift to lower angles at higher temperatures and higher heating durations. This can be indicative of an increment in the lattice parameters (volume) of the unit cell at higher temperatures. This may be explained

as the tendency of vanadium to get oxidized at higher temperatures, which occurs by introduction of more oxygen atoms in the lattice. In addition, the crystallinity of the formed particles increase at higher temperatures, as can be seen from appearance of sharper peaks.

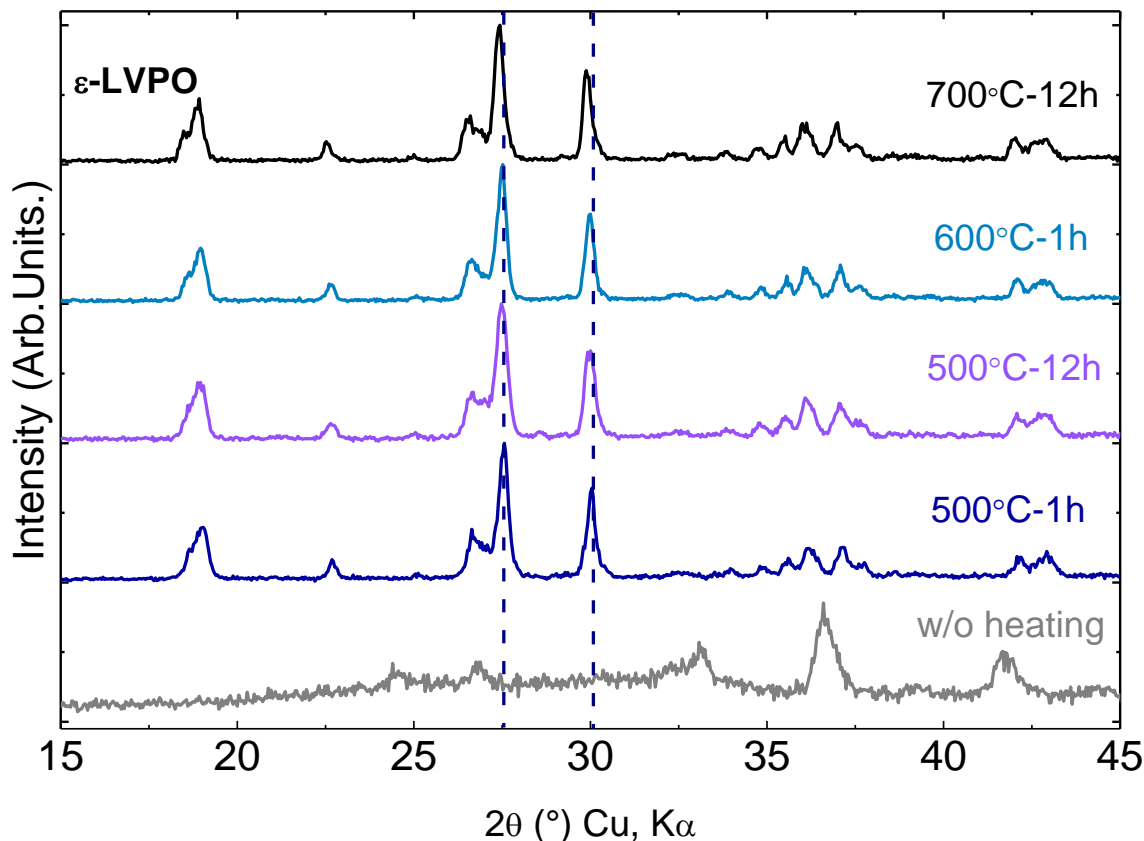


Figure 3-10 XRD patterns of the samples heat-treated at various conditions (temperature-time) from the batch prepared through ball-milling in agate jar. The pre-heated sample is also shown, marked as w/o heating. The dotted horizontal lines show the main peak positions of ϵ -LVPO, which can shift at higher temperatures.

As mentioned above, in a separate experiment, the synthesis process was initiated using zirconia jar as the grinding medium. Similar heat-treatments were repeated in the powders of the same batch from zirconia jar. The XRD patterns of these products are shown in Figure 3-11. We can see that calcination at 500 °C resulted in formation of a different phase than ϵ -LVPO. Phase identification showed that the peaks belong to another polymorph of LVPO (β -LVPO with orthorhombic structure). This phase remained stable at 600 °C for various heating durations (1, 12, 24 h). At 700 °C, the ϵ -LVPO phase started to form. At 1h calcination duration, both polymorphs were present and after calcination for 12 h, the β -phase completely disappeared and the triclinic ϵ -phase was dominant. Similar to previous observations for VPO, we can see that the synthesis of vanadium oxy-

phosphate compounds depends on a variety of parameters. In this case, the ball-milling medium, being the jar material, could play a role in stabilization of the polymorphs. It is believed that zirconia can affect the mix by oxidizing the materials. β -LVPO has a higher tendency than ϵ -LVPO to form in the oxidizing mediums [Hidalgo, 2019]. Therefore, the β polymorph forms by mixing the batch in the zirconia jar. However, the sensitivity of the synthesis suggests that other factors such as changes lab humidity could also affect the synthesis.

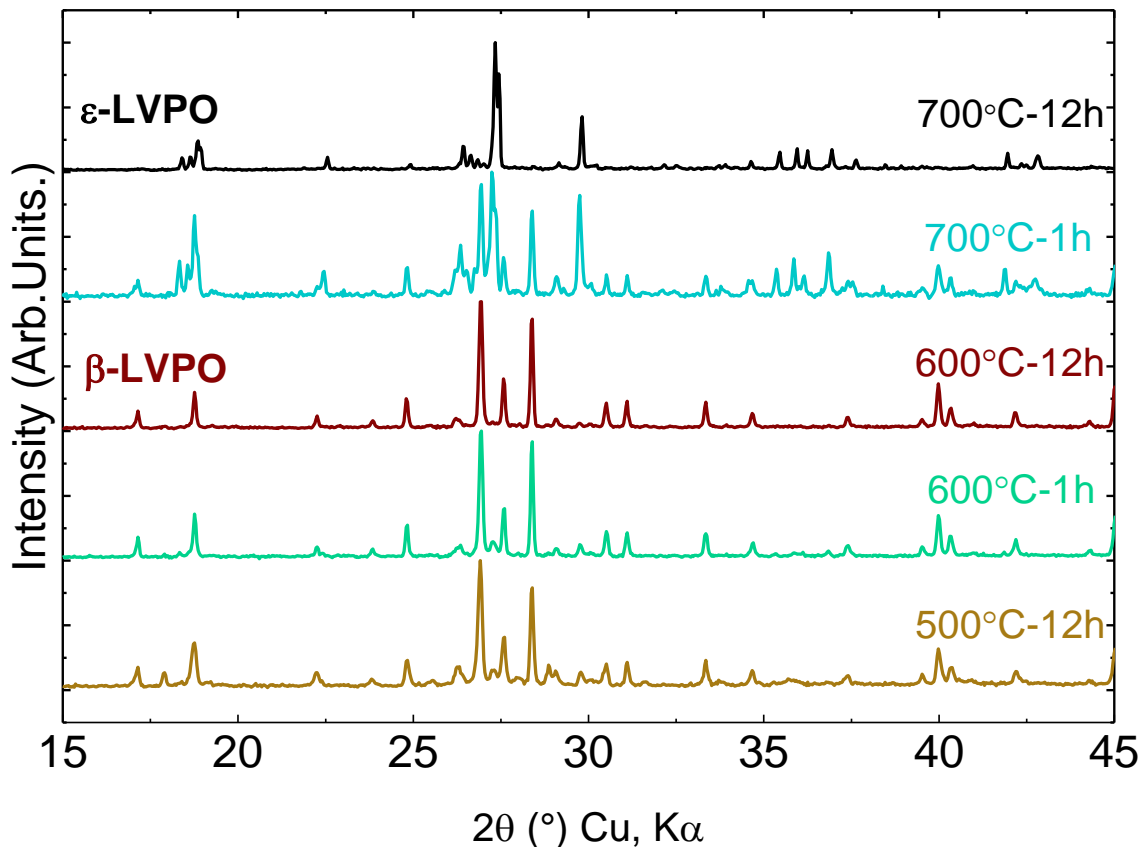


Figure 3-11 XRD patterns of the samples heat-treated at various conditions (temperature-time) from the batch prepared through ball-milling in zirconia jar.

SEM micrographs of the ϵ -LVPO material synthesized at 700 °C are shown in Figure 3-12. The sample contains agglomerates larger than 30 μm (Figure 3-12a). These agglomerates are composed of primary particles with 1-2 μm size. The particles have prismatic crystalline shapes.

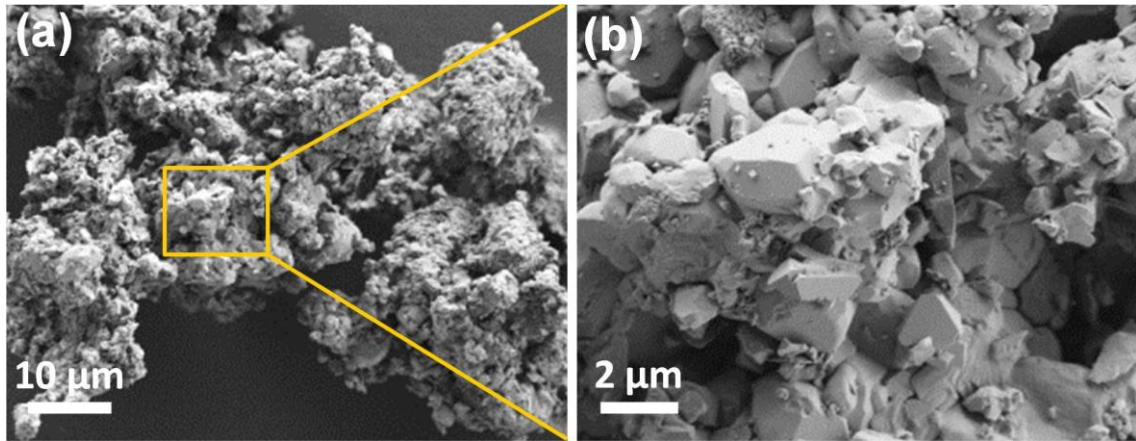


Figure 3-12 SEM micrographs of the ϵ -LVPO particles obtained at 700 °C, (a) at low magnification, showing the agglomerate and (b) at high magnification showing the single particles.

3.2.2. Crystal Structure

The Fullpattern LeBail refinement matching of XRD pattern of the synthesized LVPO sample at 700 °C-12 h is shown in Figure 3-13. The photograph in the inset of Figure 3-13 shows the teal green ϵ -LVPO powder. It has a triclinic crystal structure with $P\bar{1}$ space group ($N^{\circ}2$). The structural parameters obtained through refinement are shown in Table 3-2.

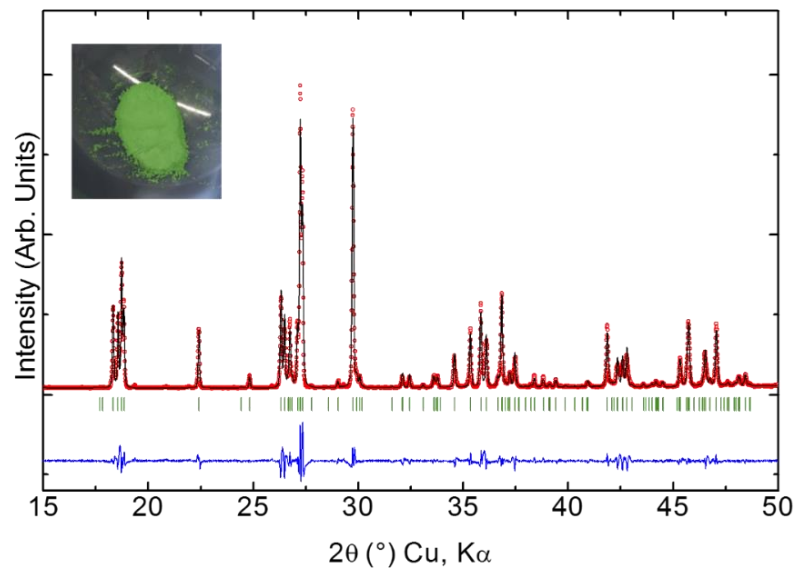


Figure 3-13 Fullpattern refinement matching of XRD pattern of ϵ -LVPO using LeBail method. The observed, calculated and difference curves are presented as red dots, black line and blue lines, respectively. The Bragg positions are shown as green lines. The inset shows the synthesized powder.

Table 3-2 Structural parameters of the synthesized ϵ -LVPO calculated by LeBail refinement matching method.

a (Å)	b (Å)	c (Å)	α (°)	β (°)	γ (°)	V (Å ³)
6.729(1)	7.198(1)	7.928(3)	89.812(9)	91.223(0)	116.856(7)	342.519

ϵ -LVPO has a Tavorite-type structure. The crystal structure of ϵ -LVPO can be described as an arrangement of VO₆ octahedra and PO₄ tetrahedra (Figure 3-14a, b). The octahedra are connected to each other by oxygen atoms (O(5) and O(6)) forming chains which run along the ***b*** direction (Figure 3-14c). Along that direction, there is alternatively long (V–O) and short (V=O) vanadyl bonds, the latter being a double bond. Within the structure, there are two types of V octahedra: V(1)O₆, for which the equatorial plane is almost parallel to the ***b*** direction, and V(2)O₆ with the equatorial plane being almost perpendicular to the ***b*** direction. As a result, the chains are forming a *trans* arrangement along the ***b*** direction (Figure 3-14a). Chains of VO₄O₂–VO₄O₂ are further connected to each other through PO₄ tetrahedra. This connection is done by the bridging oxygen atoms, which are in the equatorial plane of VO₆ octahedra. Note that there are also two types of PO₄ tetrahedra which alternate along the ***b*** and ***a*** direction (Figure 3-14b). The refinement of the structure shows that the V(2)O₆ octahedron is slightly more symmetrical than the V(1)O₆ octahedron ($\Delta = 5.51 \times 10^{-3}$ and $\Delta = 7.63 \times 10^{-3}$ respectively). Lithium in LVPO framework structure is located in 3D tunnels generated by polyhedra which run along the $[1\bar{1}0]$, $[101]$ and $[10\bar{1}]$ directions [Ateba Mba, 2012][Ateba Mba, 2013]. The minimum Li-Li distance along the $[10\bar{1}]$ tunnel in LVPO is about 5.6 Å, while in Li₂VPO₄O (with an extra incorporated Li) is 5.3 Å in the similar $[101]$ tunnel [Bianchini, 2014]. It is, thus, possible to incorporate extra Li within LVPO framework structure without generating steric constraint.

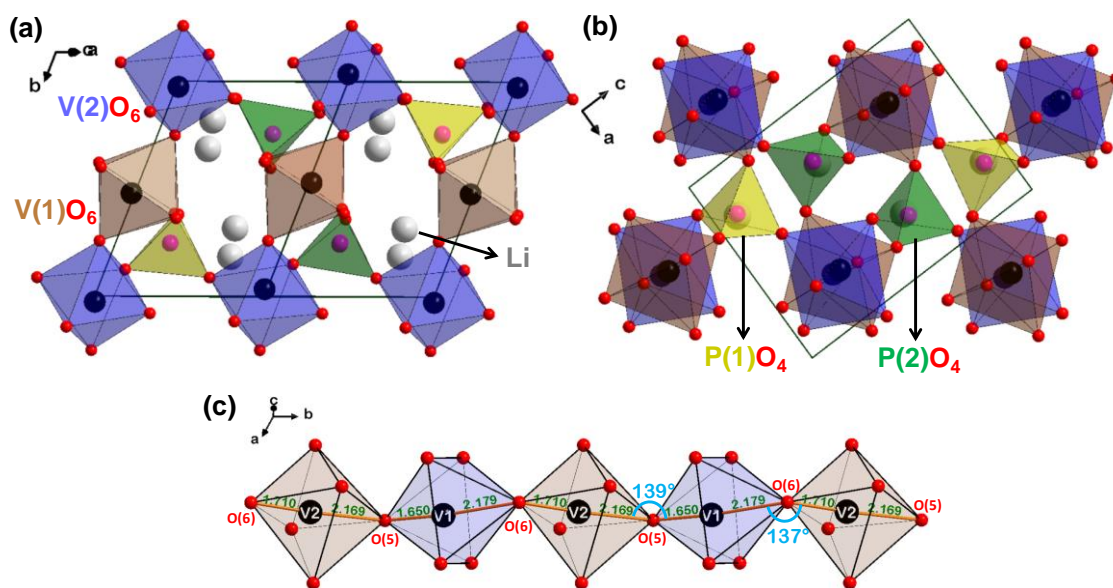


Figure 3-14 The crystal structure of ϵ -LVPO; (a) and (b) interconnection of VO₆ and PO₄ tetrahedra in two different directions, and (c) octahedral chain formed from V(1)O₄O₂ and V(2)O₄O₂.

3.2.3. Electrochemical Behavior

The lithium extraction/insertion reaction from LVPO, in the high-voltage range relies on the reversibility of the V⁴⁺/V⁵⁺ redox couple, while the lithium insertion/extraction reaction in the lower voltage range relies on the reversibility of the V³⁺/V⁴⁺ redox couple. The related electrochemical reactions can be summarized as Equation 3-7 and Equation 3-8, respectively. The theoretical capacity of LVPO for such reactions is 159 mAh/g:

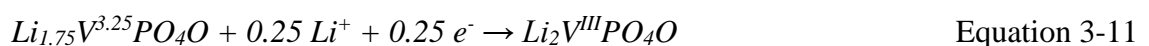
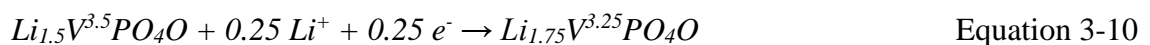
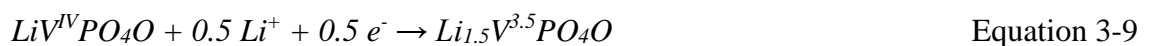


The galvanostatic charge/discharge (Li extraction/insertion) signature of LVPO was investigated by testing it as cathode material in a half-cell battery. Figure 3-15a, b show the galvanostatic cycling curves of ϵ -LVPO for the first 10 cycles, at high-voltage range (3.0-4.5 V vs. Li/Li⁺) and low-voltage range (1.5-3.0 V vs. Li/Li⁺), respectively. The current density for the cycling process corresponded to C/50 cycling rate.

At the high-voltage range, a biphasic reaction at 3.95 V with the activity of V⁴⁺/V⁵⁺ redox couple took place. We can see that in the first cycle, only about 0.5 Li is extracted from the pristine ϵ -LVPO. This means that only half of the theoretical capacity (~82 mAh/g specific capacity) is reached. The specific capacity increased slightly by increasing of

cycle numbers. This was observed by Ateba Mba [2013] and was attributed to big particles of ϵ -LVPO (Figure 3-12), since shrinkage in particle size by Spex milling improved the cycling and increased the capacity. However, Allen et al. notes that the better cyclability of ϵ -LVPO after Spex milling is not due to the particle size reduction, since the same process with planetary ball-milling did not result in higher capacity. Instead, they relate the better cycling to the ability of Spex in incorporating conductive carbon with the ϵ -LVPO phase [Allen, 2011]. In addition, synthesis of products with particle sizes ranging from a few microns to 100 nm through the same synthesis route resulted in similar capacities in another study [Harrison, 2013]. Therefore, particle size is not the sole parameter affecting the capacity. Nevertheless, breaking up the agglomerates or cracking the crystallites allows better accessibility of electrolyte to the active material at later cycles [Chen, 2014]. The polarization also decreased by increasing cycle numbers. The decrease of polarization along with the increase in capacity shows the activation of more particles during cycling which leads to lower current per surface. It should be mentioned that the high polarization of ϵ -LVPO is related to its large band gap which results in low electrical conductivity [Lin, 2017].

At low-voltage range, three biphasic reactions (plateaus) took place at 2.48, 2.21, and 2.03 V vs Li/Li⁺ through insertion of Li into LVPO (LiVPO₄O), yielding a composition close to Li₂VPO₄O. Three intermediate reactions (Equation 3-9, Equation 3-10 and Equation 3-11) indicate the formation of two intermediate phases before reaching final Li₂VPO₄O phase. These intermediate phases are Li_{1.5}VPO₄O and Li_{1.75}VPO₄O, which have respectively +3.5 and +3.25 average values as vanadium valence state. The valence state of vanadium changes according to the amount of Li in each phase, where it spans from +4 in LiVPO₄O to +3 in Li₂VPO₄O [Ateba Mba, 2013][Bianchini 2014].



We succeeded in inserting about 0.9 Li into LVPO structure (Figure 3-15b). It has been shown that the kinetics of such process at low-voltage domain is more favorable than extracting Li from LVPO at high-voltage domain [Lin, 2016]. Therefore, higher Li amount can be exchanged at low-voltage range. The flat plateaus tend to fade at higher

cycling numbers, which can be attributed to electrode failing and/ or structural changes, possibly amorphisation. However, it should be mentioned that the distinct plateaus corresponding to formation of intermediate phases were not observed in some of the previous studies on galvanostatic cycling of ϵ -LVPO at low potentials. For example, in the study from Harrison *et al.*, a single sloping voltage curve was observed, which corresponded to a single-phase (solid-solution) Li insertion/extraction mechanism [Harrison, 2014]. This can be attributed to the synthesis method that would lead to different level of crystallinity of the particles.

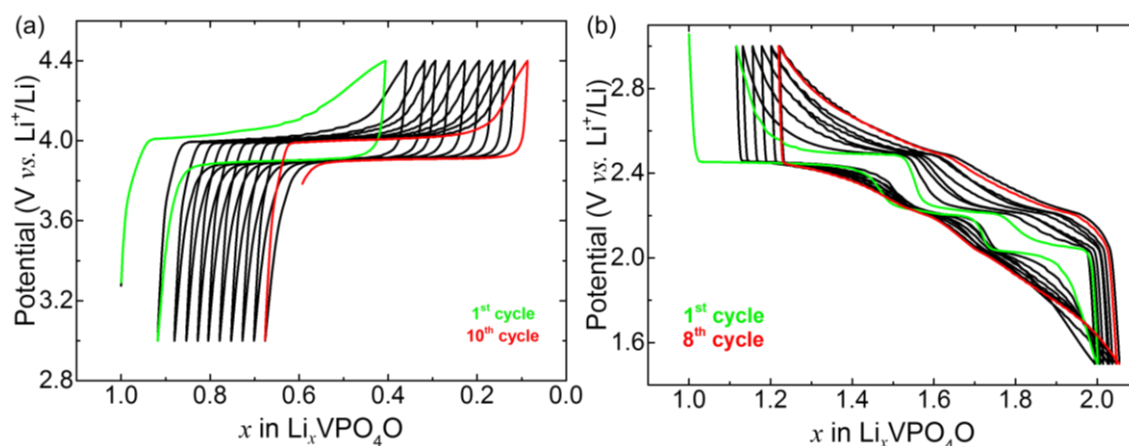


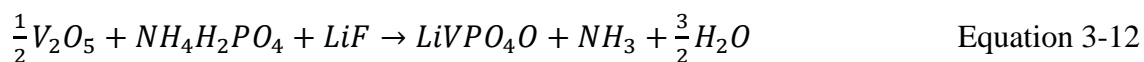
Figure 3-15 galvanostatic cycling curves of ϵ -LVPO for the first 10 cycles, at high-voltage range (3.0-4.5 V vs. Li/Li^+) and low-voltage range (1.5-3.0 V vs. Li/Li^+).

3.3. β -LiVPO₄O

In addition to the β -LVPO (β -LiVPO₄O) phase obtained through calcination of the V₂O₃-precursor batch (described in section 3.2.1.), a specific synthesis was carried out using V₂O₅ as the precursor to obtain β -LVPO. In this section, explicit synthesis of β -LVPO, the related characterization, its crystal structure and the electrochemical behavior of this phase is discussed.

3.3.1. Synthesis and Characterization

A ceramic route was applied in order to synthesize β -LVPO using vanadium(V) oxide (V₂O₅ from Aldrich), monobasic ammonium phosphate (NH₄H₂PO₄ from Aldrich) and lithium fluoride (LiF) as the precursors. Proportional amounts of these materials were mixed according to equation 3-7:



This mix was ground in a planetary ball-milling machine at 600 rpm for the duration of 12 h in a zirconia jar. Pellets were pressed out of this batch and were pre-treated under air at three different conditions as 300 °C-12 h, 300 °C-24 h and 450 °C-12 h. The XRD patterns of the products are shown in Figure 3-16. Pre-treatment at 300 °C for 12 h resulted in reduction of vanadium(V) oxide, as its peaks are no longer present in the pattern. Some unidentified phases were formed due to this reduction. Lithium fluoride and ammonium phosphate did not change in these conditions, as can be seen from the presence of their peaks. Pre-treatment at 300 °C, but for a longer duration (24 h) resulted in formation of a highly amorphous medium, as the XRD pattern consists of huge amorphous background. Therefore, at longer heating times at a low temperature (300 °C), the precursor phases lose their crystallinity and turn into amorphous phases. The pre-treatment at a higher temperature of 450 °C resulted in a complete phase change, where the precursor peaks disappeared and a new phase formed. Phase identification showed that the new phase is indeed β -LVPO. Therefore, it can be concluded that this heating condition were sufficient for formation of this phase.

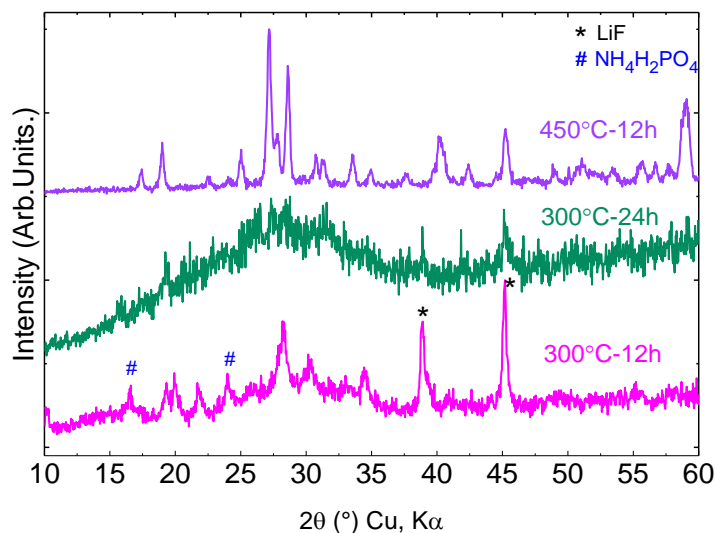


Figure 3-16 XRD patterns of pre-treated batch of V_2O_5 , LiF and $NH_4H_2PO_4$ mix heated under air at different conditions of 300 °C-12 h, 300 °C-24 h and 450 °C-12 h.

Figure 3-17 illustrates the SEM micrographs of the samples obtained at (a) 300 °C-24 h and (b) 450 °C-12h. The microstructure of the sample 300 °C-24 h consists of agglomerated stacks of thin nano-sheets/flakey crystalline particles. This shows that the XRD pattern of this sample was rather misleading, as one dimension of the flakes was

extremely small and the pattern appeared as an amorphous phase. The sample obtained at 450 °C-12 h contains at least three crystalline phases. Stacks of nano-sheets stacked in a less compact way than sample 300 °C-24 h are present that are surrounded by nano-sized particles too small to be detected by XRD. In addition, larger rock-shaped crystals (>2 μm) are also present, which are attributed to the non-reacted V₂O₅ precursor, as confirmed by EDS.

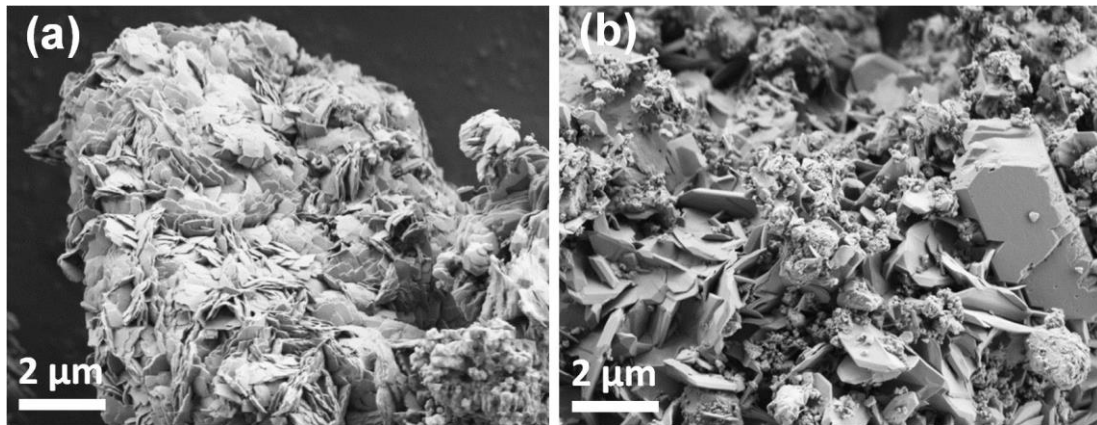


Figure 3-17 SEM micrographs of the samples pre-treated at (a) 300 °C-24 h and (b) 450 °C-12h.

New pellets were prepared of the pre-treated materials at three various conditions, which then were subjected to a subsequent calcination process. The pre-treated batch at 300 °C-12h was heated at 400 °C-12 h, 500 °C-1h and 600 °C-1h conditions. Figure 3-18 shows the XRD patterns of the materials obtained after such heat treatments. Additionally, XRD pattern of the pristine batch (pre-treated w/o heating) is also shown for comparison. The sample heat-treated at 400 °C for 12 h showed the formation of ϵ -LVPO phase. This temperature is quite low for the formation of this high-temperature polymorph. This can be due to the amorphous state of the pristine batch. When starting with an amorphous structure, which is reminiscent of a liquid, the first phase that forms is the high-temperature phase which is closest to the amorphous structure in terms of its density. To the best of our knowledge, ϵ -LVPO has not been obtained through ceramic synthesis at this temperature, before. β -LVPO phase also started to form at this temperature. However, its amount was rather small. Increasing the calcination temperature to 500 °C and 600 °C resulted in a decrease in the amount of ϵ phase and an increase in β , as can be seen from the peak intensities in XRD patterns.

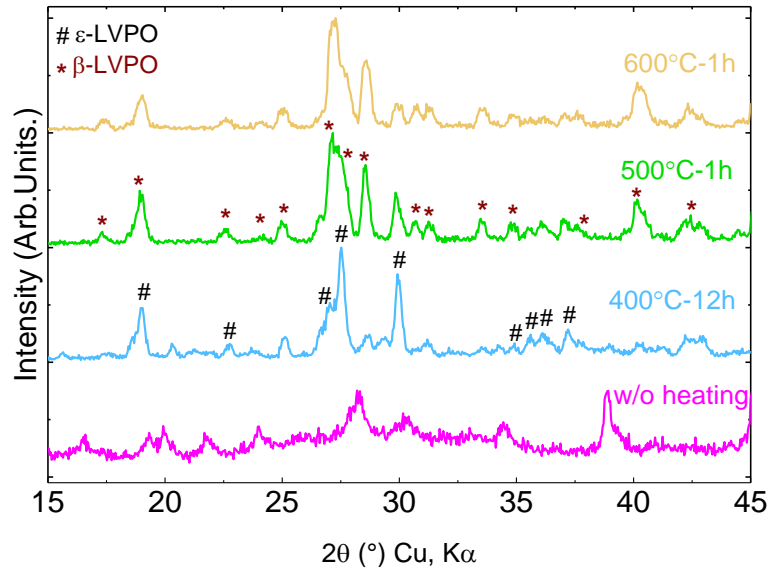


Figure 3-18 XRD patterns of the samples heat-treated at various conditions, from the starting batch that was pre-treated at 300 °C-12 h (w/o heating pattern).

Figure 3-19 shows the XRD patterns of the samples from the 300 °C-24 h batch, heat-treated at 500 °C and 600 °C in comparison with the pristine amorphous sample. In these samples, β -LVPO is the dominant phase, although with some existing impurities at 500 °C. This indicates that a longer pre-treatment duration at 300 °C has had an effect on the final product (comparing with same heating conditions for the samples of 300 °C-12 h batch) and facilitated the formation of β phase.

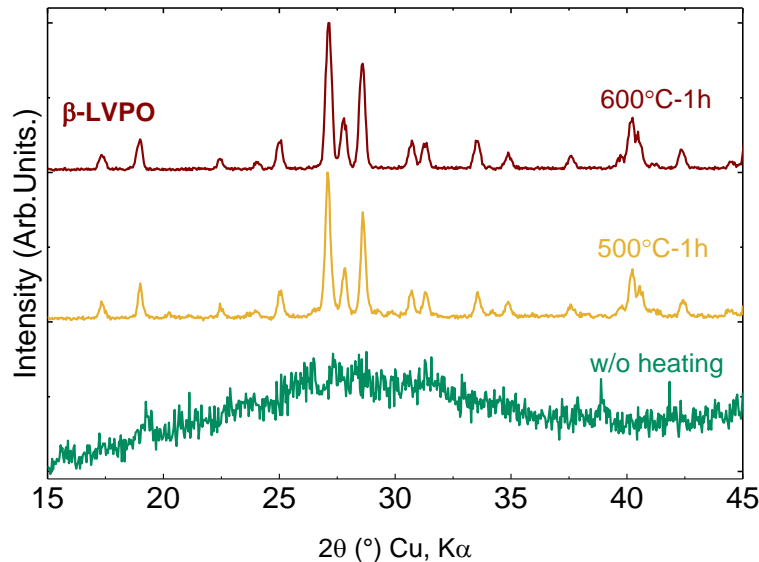


Figure 3-19 XRD patterns of the samples heat-treated at 500 °C and 600 °C for 1 h, from the starting batch that was pre-treated at 300 °C-24 h (w/o heating pattern).

The microstructure of the heat-treated sample at 600 °C from the 300 °C-24 h batch is shown in Figure 3-20, at low (a) and (b) high magnification SEM micrographs. Smaller agglomerates compared to the pre-treated sample (Figure 3-20-b) are present. The flakey nano-sheets with micrometer-size diameter and <100 nm thickness are the dominant particles.

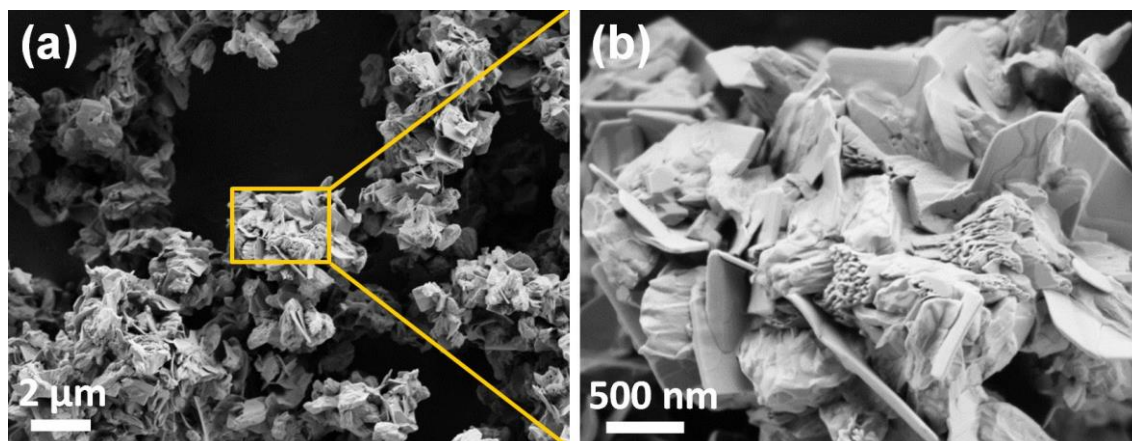


Figure 3-20 SEM micrographs of the sample obtained at 600 °C from the 300 °C-24 h batch, (a) at low magnification, showing the agglomerates and (b) at high magnification showing the single particles morphology.

As was seen earlier, the pre-treatment of the ground batch at 450 °C-12 h resulted in formation of the β -LVPO phase. Further calcination at 600 °C did not result in any phase change, however the crystallinity of the material increased, as can be seen in the sharp peaks of the XRD pattern of the calcined sample vs. pristine batch (Figure 3-21).

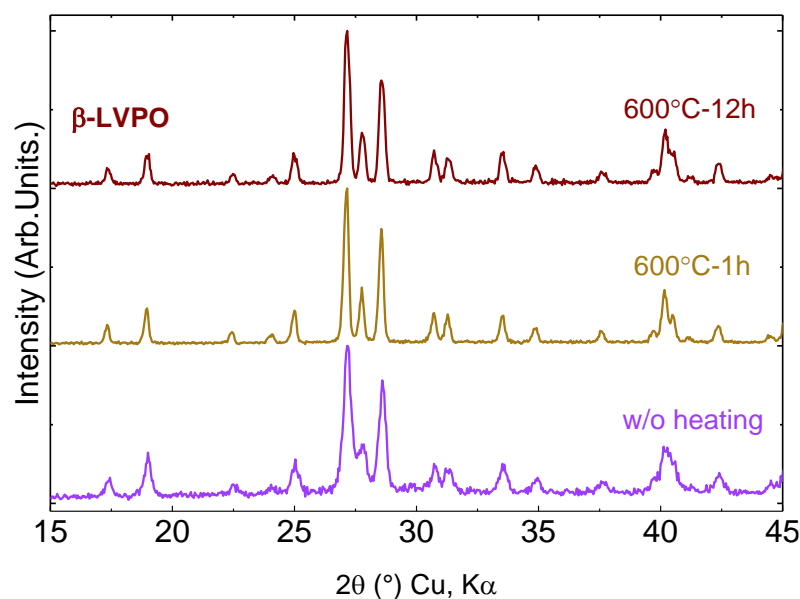


Figure 3-21 XRD patterns of the samples heat-treated at 600 °C for 1 h and 12 h, from the starting batch that was pre-treated at 600 °C-12 h (w/o heating pattern).

XRD phase analysis indicated β -LVPO phase as the product of the reaction according to Equation 3-4. However, the fate of fluorine needs to be investigated, as LiF was used as the precursor. To investigate the elemental composition, STEM-EDX analysis was performed on single particles of the β -LVPO phase. The results showed the presence of V, P and O, with no trace of F in the composition. Thus, it was confirmed that the product is a pure LiVPO_4O and not a solid solution as $\text{LiVPO}_4\text{O}_x\text{F}_y$. The absence of F in the synthesis product despite the use of LiF as the precursor was observed in some other studies related to the synthesis of ϵ -LVPO [Allen, 2011][Ateba Mba, 2013]. This was explained with the formation of HF during the reaction, which would consume the fluorine ions and leave Li ions to be used for LVPO formation. The formed HF could evaporate at high synthesis temperatures upon formation or react with the heating crucibles in minor amounts.

3.3.2. Crystal structure

The obtained LVPO phase was successfully refined in the orthorhombic lattice structure (Figure 3-22) with $Pnma$ space group (N°62). The inset shows the β -LVPO powder. It has a brighter shade of green color than ϵ -LVPO. The refined lattice parameters are shown in Table 3-3.

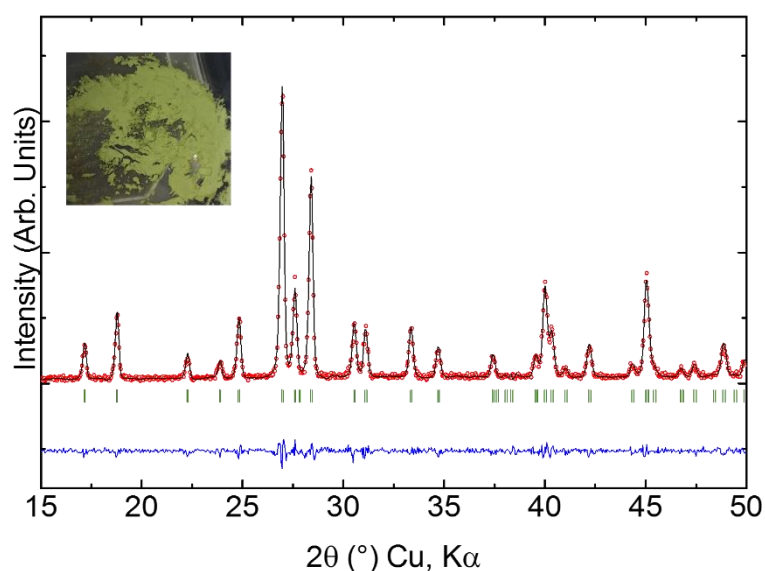


Figure 3-22 Fullpattern refinement matching of XRD pattern of β -LVPO using LeBail method. The observed, calculated and difference curves are presented as red dots, black line and blue lines, respectively. The Bragg positions are shown as green lines. The inset shows the synthesized powder.

Table 3-3 Structural parameters of the synthesized β -LVPO calculated by LeBail refinement matching method.

a (Å)	b (Å)	c (Å)	α (°)	β (°)	γ (°)	V (Å ³)
7.453(4)	6.286(5)	7.175(5)	90.00	90.00	90.00	336.220

The β -LVPO framework structure is closely related to the one of β -VPO (see section 3.1). This framework consists of infinite chains of corner-shared distorted VO_6 octahedra, which are cross-linked by corner-sharing PO_4 tetrahedra (Figure 3-23a). These chains are formed along the a direction and the equatorial V-O bonds are placed along the bc planes. Similar to ε -LVPO, the chain comprises alternative short (1.63 Å) and long (2.43 Å) V-O bonds (Figure 3-23b). The bond length difference is less than the one found in β -VPO (1.57 Å and 2.59 Å) due to lower valence state (V^{4+}). The V-O-V angles are larger in β -LVPO than β -VPO (see Figure 3-8b) to accommodate the additional Li ions. The Li ions are located at 1D channels in the a direction between V and P polyhedral [He, 2016].

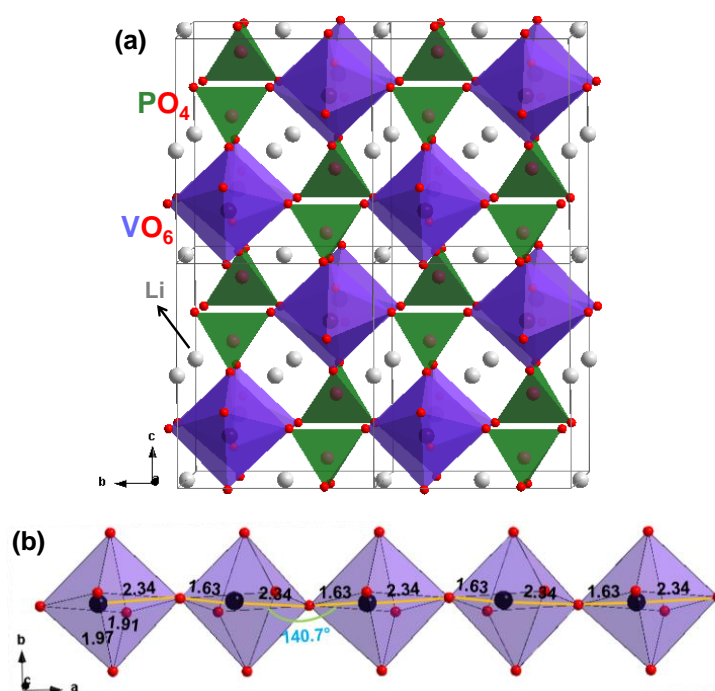


Figure 3-23 The crystal structure of β -LVPO; (a) interconnection of VO_6 and PO_4 tetrahedra and (b) octahedral chain formed from VO_6 .

3.3.3. Electrochemistry

As was discussed in section 3.2 for ε -LVPO, the lithium extraction/insertion into β -LVPO relies on the reversibility of the $\text{V}^{4+}/\text{V}^{5+}$ redox couple, in the high-voltage range. In the low voltage range, the lithium insertion/extraction from β -LVPO occurs with $\text{V}^{3+}/\text{V}^{4+}$ redox couple. The related electrochemical reactions can be summarized as Equation 3-13

and Equation 3-14, respectively. The theoretical capacity of LVPO in such reactions is 159 mAh/g.



The galvanostatic cycling behavior of β -LVPO was studied by using it as the cathode material in a half-cell battery with a current density corresponding to C/50 cycling rate. Second cycles at high-voltage range (3.0-4.5 V vs. Li/Li⁺) and low-voltage range (1.5-3.0 V vs. Li/Li⁺) are shown in Figure 3-24a, b, respectively. At high-voltage range, a rather flat plateau takes place at ~3.98 V vs. Li/Li⁺ for the Li extraction/insertion reaction. Almost 0.8 Li is exchanged during the reaction, which corresponds to ~127 mAh/g charge capacity and 506 Wh/kg energy density.

At low-voltage range (Figure 3-24b), a short semi-flat plateau is observed at ~2.2 V vs. Li/Li⁺ for the Li insertion/extraction reaction. In the rest of the potential window, reaction seems to proceed as a sloping voltage curve which can be indication of a solid-solution behavior. The high polarization observed at the low-voltage range brings about additional difficulty in any further interpretation. Nevertheless, this β -LVPO sample has a low electrochemical activity at the low-voltage range as only <0.2 Li could be inserted in β -LVPO structure. Harrison *et al.* have investigated the lithiation of β -LVPO in detail. They observed a longer plateau at 2.2 V until insertion of 0.6 Li and a sloping region for the rest of discharge [Harrison, 2013]. The differences in the observed electrochemical properties can arise from small variations in the structure which would limit the Li diffusion in the structure.

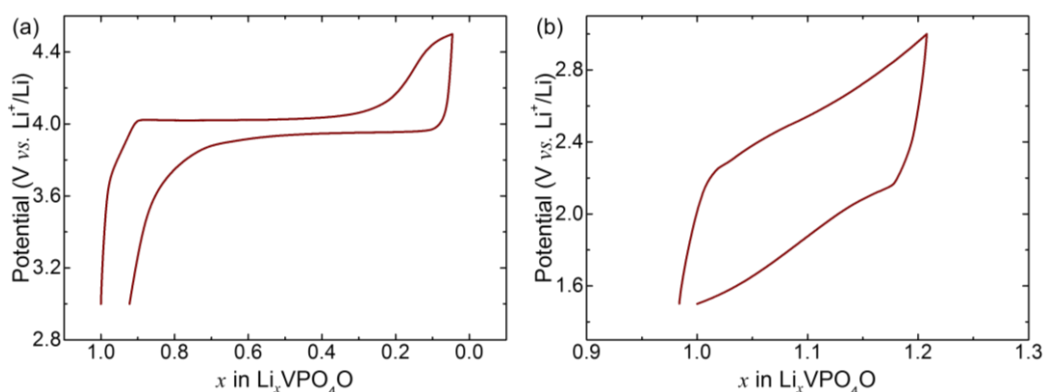


Figure 3-24 Galvanostatic cycling curve of β -LVPO at second cycle at (a) high-voltage range (3.0-4.5 V vs. Li/Li⁺) and (b) low voltage range (1.5-3.0 V vs. Li/Li⁺) with a current density corresponding to C/50 cycling rate.

Extraction of Li from β -LVPO and insertion of Li into β -VPO follow similar pathways. In Figure 3-25, the cycling curves for oxidation of β -LVPO (from Figure 3-24a) and reduction of β -VPO (from Figure 3-9) are compared. The reaction signature for the two different materials is very similar. Both reactions have an operating potential of ~ 3.98 V vs. Li/Li^+ and the polarization is almost identical in two curves. However, a higher amount of Li is exchanged in the reaction of β -LVPO starting material (solid red curve) than in the reaction of β -VPO (dashed purple curve) reaction than the one in β -VPO. This is presumed to be due to the better Li exchange kinetics of β -LVPO vs. β -VPO, since β -LVPO has already defined Li positions in the structure.

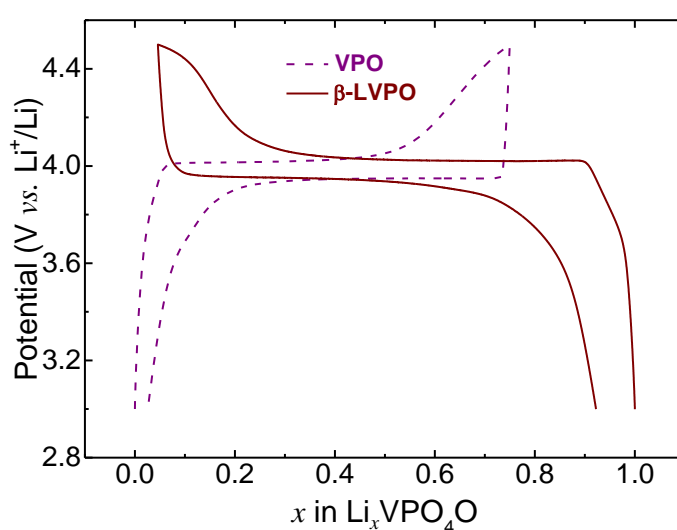


Figure 3-25 Comparison between galvanostatic cycling curves of β -VPO (starting with oxidation) and β -LVPO (starting with reduction).

As discussed in Chapter 1, the synthesis method can influence some electrochemical characteristics of this type of materials. The comparison between cycling signature of β -LVPO and ϵ -LVPO synthesized in this work is of interest, since similar methods were used for their preparation. Figure 3-26 shows the second cycle of galvanostatic cycling test for the $\text{V}^{4+}/\text{V}^{5+}$ redox couple for these two phases. β -LVPO has a slightly higher redox potential than ϵ -LVPO (3.98 V vs. 3.95 V), which is in good agreement with results obtained by Whittingham group [Hidalgo, 2019]. In addition, in these results, the exchanged Li amount is higher in β -LVPO phase. As was discussed in the first chapter, there is discrepancy in literature regarding the extracted capacity of these phases [He, 2018][Hidalgo, 2019]. However, a higher capacity observed in β -LVPO could be indicative of better kinetics during Li insertion/extraction reactions.

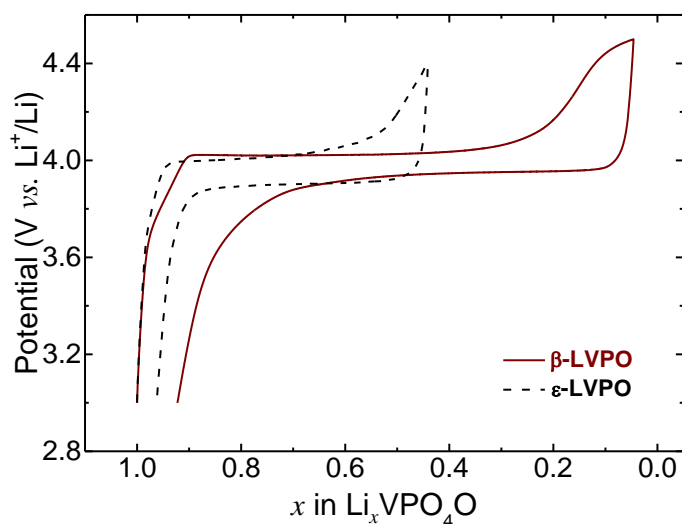


Figure 3-26 Comparison between galvanostatic cycling curves of β -LVPO and ϵ -LVPO.

3.4. LiVPO₄F

In this work, lithium vanadium fluoro-phosphate (LiVPO₄F) powder was prepared and characterized for the sake of comparison with vanadium oxy-phosphate materials. The synthesis was carried out according to the method reported by Barker et al. in which firstly an intermediate VPO₄ phase is obtained and then mixed with LiF to obtain LiVPO₄F [Barker, 2003]. The carbothermal synthesis of VPO₄ was already explained in section 3.1 for the synthesis of VPO.

In the next step, VPO₄ was mixed with lithium fluoride (LiF) according to Equation 3-8 and ground in an agate mortar for 15 mins to ensure well-mixing between the powders.



Then, pellets (8 mm in diameter) were pressed, which were then inserted in a golden tube inside a stainless-steel reactor. These reactors were sealed in the glovebox to maintain an Ar atmosphere inside the reactor. This prevents the oxidation of vanadium and formation of impurities such as Li₃V₂(PO₄)₃ in the final product. The reactors were then heated at 750 °C for 1 h and subsequently quenched in liquid nitrogen. The XRD pattern of the final product is shown in Figure 3-27, which matches well with the one of LiVPO₄F (abbreviated as LVPF). It has a Tavorite-type structure with a triclinic lattice described

in $P\bar{1}$ space group (N°2). No impurities such as $\text{Li}_3\text{V}_2(\text{PO}_4)_3$ were observed at the X-ray detection levels.

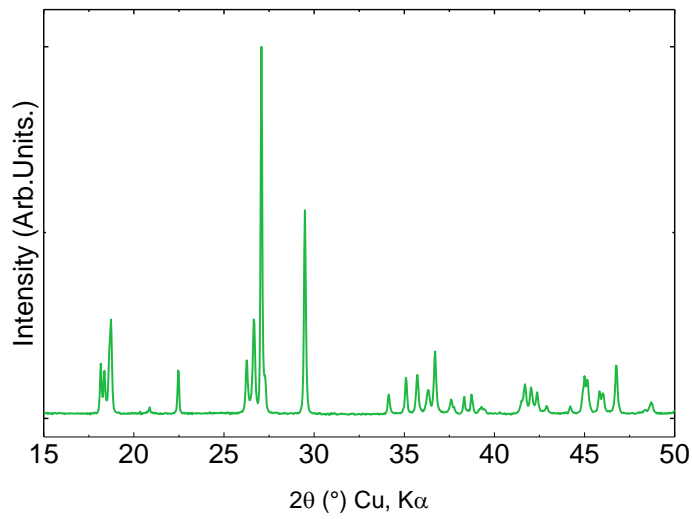


Figure 3-27 XRD pattern of synthesized LVPF sample.

The SEM micrographs of LVPF material at low and high magnifications are shown in Figure 3-28 a, b, respectively. Agglomerates in the size range of 10 μm are formed. These agglomerates consist of well-crystallized particles with the average size of 500 μm . The particle surfaces are highly covered with carbon particles, which are remaining from the synthesis process by using VPO_4 . The particle growth was limited even at high temperature of 750 $^{\circ}\text{C}$ most probably due to the presence of residual carbon throughout the synthesis process [Boivin, 2018].

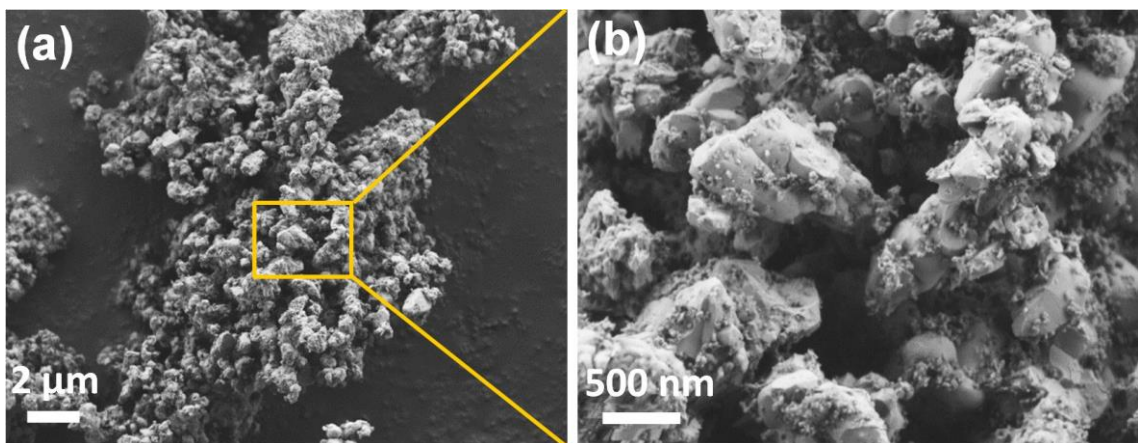


Figure 3-28 SEM micrographs of the LVPF sample, (a) at low magnification, showing the agglomerates and (b) at high magnification showing the single particles morphology.

The galvanostatic cycling of LVPF vs. Li/Li^+ was carried out with a current density of $C/50$ in a half cell battery. Figure 3-29 a, b show the cycling results at high-voltage ($\text{V}^{3+}/\text{V}^{4+}$ redox) and low-voltage ($\text{V}^{3+}/\text{V}^{2+}$ redox) ranges, respectively. At high-voltage range, a plateau is observed at around 4.26 V, with the presence of a step during charge, which is associated with the formation of $\text{Li}_{0.67}\text{VPO}_4\text{F}$ intermediate phase. Such phase does not appear during discharge. At low-voltage range, a plateau is observed at 1.79 V for the biphasic reaction of LVPF lithiation. Values very close to theoretical capacity can be obtained for this material, as is observed at both curves. For the $\text{V}^{3+}/\text{V}^{4+}$ redox couple, one Li is exchanged during the reaction leading to VPO_4F . For the $\text{V}^{3+}/\text{V}^{2+}$ redox couple, about 0.9 Li is inserted/extracted. In addition, the polarization is relatively small during cycling. The additional carbon from the synthesis process help in a better electronic conductivity and the small particle size improves the electrochemical wiring, thus lowering the polarization. The presence of F in the structure, in addition, helps in Li diffusion, leading to a higher charge/discharge capacity.

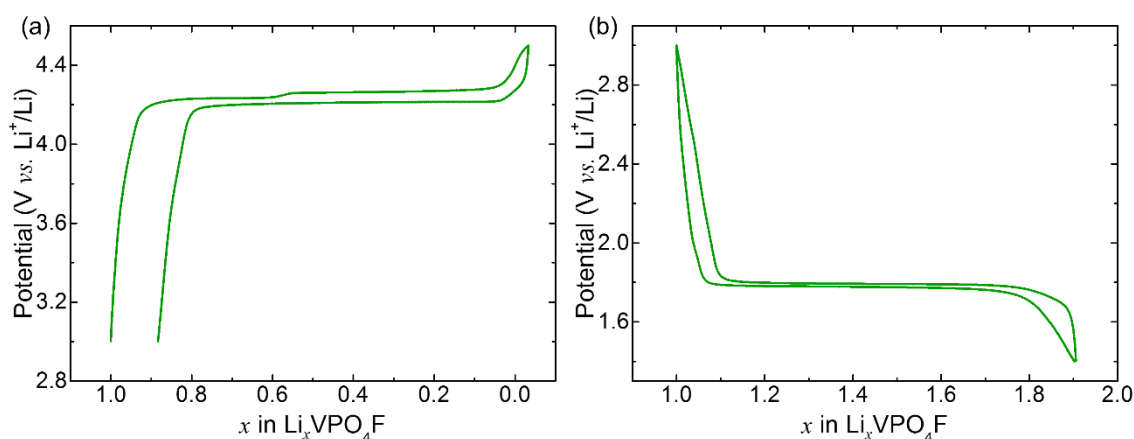


Figure 3-29 Galvanostatic cycling curve of LVPF at second cycle at (a) high-voltage range (3.0-4.5 V vs. Li/Li^+) and (b) low voltage range (1.5-3.0 V vs. Li/Li^+) with a current density corresponding to $C/50$ cycling rate.

3.5. Summary and Discussion

In this chapter, the synthesis, characterization and electrochemical behavior of (lithium) vanadium oxy-phosphate materials ($\text{Li}_x\text{VPO}_4\text{O}$ with $x=0,1$) were described. These compounds have several polymorphs. One vanadium oxy-phosphate polymorph, β -VPO, and two lithium vanadium oxy-phosphate polymorphs, ϵ -LVPO and β -LVPO, were synthesized in this work. Although these materials are well known in the literature, their

synthesis can be challenging. In this work, solid-state ceramic method was used for the synthesis of these materials. New synthesis routes using different precursors than reported in the literature was applied for the synthesis of some of the materials. The properties of such materials can highly depend on the applied synthesis method. Therefore, their characteristics including morphology, crystal structure and electrochemical signature of the synthesized materials were investigated and compared to the previously reported products, where necessary.

Firstly, the synthesis of β -VPO was discussed. Obtaining a single phase of VPO proved to be challenging. Different polymorphs tended to form simultaneously and controlling the purity of the synthesis products was difficult. Many parameters affected the synthesis such as temperature, heating duration, heating rate and atmosphere. Two routes were applied for the synthesis of β -VPO. For the synthesis of β -VPO using V_2O_3 precursor, temperatures as high as 740 °C and/or slow heating rates (0.5 °C/min) were required. The route including the oxidation of VPO_4 to form VPO gave the purest β -VPO products and most consistent results. This may be due to the higher tendency of $V^{3+}PO_4$ for being oxidized with respect to $V^{3+}_2O_3$ that provides a more straightforward route to phase formation. The synthesized β -VPO consisted of agglomerations of particles with not well-defined crystal shapes. The crystal structure was well-fitted with the reported orthorhombic *Pnma* structure. The operating potential of ~3.97 V vs. Li/Li^+ was recorded for V^{4+}/V^{5+} redox couple in the galvanostatic measurement. About 0.6 Li was exchanged during the redox reaction.

Secondly, the synthesis of ϵ -LVPO was described. The ceramic synthesis method using V_2O_3 as the vanadium precursor resulted in formation of ϵ -LVPO at ~500 °C. But, this phase formation was not always repeatable as the phase could form only at 700 °C at some experiments, while β -LVPO was formed at lower temperatures. However, in general this compound was easier to synthesize as a single-phase and without impurities compared to β -VPO. The synthesis at 700 °C-12h resulted in well-crystallized particles with 1-2 μm size. The triclinic lattice structure was fitted well with the previously-reported structure in the relevant ICSD card. At high-voltage range for V^{4+}/V^{5+} redox couple, the operating potential was ~3.95 V vs. Li/Li^+ , while at low-voltage range for V^{3+}/V^{4+} redox couple, 3 distinct plateaus at 2.48, 2.21, and 2.03 vs. Li/Li^+ took place. The presence of distinguishable plateaus at the lower range confirmed the well crystallization

of the lattice, where extraction/insertion of Li into the lattice was possible in defined potentials.

Thirdly, the synthesis procedure of β -LVPO polymorph was discussed. Here, $V^{5+}_2O_5$ was reduced in the presence of LiF to form the β -LVPO phase containing V^{4+} . Although a mixed-phase product was formed at some heat-treatment conditions, a pure phase was obtained at temperatures around 600 °C. The formed phase at lower temperatures (300 °C and 450 °C) consisted of stacked flakey/nano-sheet particles, which transformed to separated nano-sheets at higher temperatures. This phase had an operating potential ~ 3.98 V vs. Li/Li⁺ for V^{4+}/V^{5+} redox couple, which was slightly higher than ϵ -LVPO (3.95 V). V=O bond has higher covalency and shorter length in β -LVPO than ϵ -LVPO (1.63 Å vs. 1.71 Å). A higher covalency of the bond character usually implies a lower redox potential, due to a weaker inductive effect. Therefore, the bond length cannot explain the difference in the redox potential in this case. Another explanation is that the β polymorph is more prone to oxidation than the ϵ polymorph and the ϵ one contains O₂ vacancies. This results in a lower average valence state of V in ϵ -LVPO compared to β -LVPO, which in its turn, results in a lower redox potential vs. Li. In addition, β -LVPO showed higher charge/discharge capacity than ϵ -LVPO for V^{4+}/V^{5+} redox reaction, where almost 1 Li was exchanged during Li extraction/insertion reaction in β -LVPO compared to ~ 0.55 Li in ϵ -LVPO. This can be attributed to the better kinetics of Li diffusion and the higher rate capability on the surfaces of β -LVPO. The thin flakey morphology of the β -LVPO particles compared to ~ 2 μm -size prismatic particles of ϵ -LVPO also affected the ease of Li exchange during electrochemical cycling. On the other hand, β -LVPO had a much lower electrochemical activity compared to ϵ -LVPO (0.2 vs 0.9 Li insertion) for the V^{3+}/V^{4+} redox couple at low-voltage range. Therefore, the overall charge capacity during two redox reactions of V^{3+}/V^{4+} and V^{4+}/V^{5+} for two LVPO polymorphs were similar in amount.

CHAPTER4: FLUORINATION OF VANADIUM-OXY PHOSPHATES BY LiF

In this thesis, vanadium oxy-phosphate materials were subjected to fluorination with an aim to improve their electrochemical properties. The β -VPO and ε -LVPO phases were fluorinated using LiF. Usage of LiF as the fluorination resource was suggested in accordance to the successful formation of LiVPO_4F through fluorination of VPO_4 by LiF [Barker, 2003]. In this chapter, fluorination through incorporation of LiF is discussed.

4.1. Fluorination of β -VPO₄O by LiF

In this section, the results of the synthesis experiments on fluorination of β -VPO by LiF are described.

4.1.1. Synthesis and Characterization

β -VPO powder were mixed with LiF in stoichiometric amounts according to Equation 4-1:



The materials were ground and well-mixed using an agate mortar and pestle. Pellets were pressed with average weight of 150 mg using ~200 MPa pressure. The pellets were introduced in a golden tube placed in the stainless-steel reactor with ~2.5 mL inner volume. The reactors were sealed either under air or inside Ar-filled glovebox. Later, the reactors were inserted in furnaces at various temperatures (400-700 °C) and were heat-treated for one hour. The reactors were quenched in liquid nitrogen for 30 s.

The XRD patterns of the heat-treated samples (named VPOF) are shown in Figure 4-1. The XRD pattern of the VPO+LiF mix prior to heating is also added for comparison. The red dashed lines show the position of LiF phase peaks. At 400 °C (VPOF-400), no major

change was observed in the X-ray pattern and β -VPO and LiF remained with no visible reaction. A new phase formed at 500 °C (VPOF-500) and simultaneously, peaks of β -VPO and LiF reduced in intensity. The newly formed phase is not well-crystallized, which is evident from the broad peaks. This phase also formed at 600 °C (VPOF-600), together with an undefined second phase with peaks at e.g. 17° and 33°. At 700 °C (VPOF-700), the peaks of reactants, β -VPO and LiF, almost disappeared and the new crystalline phase appeared without significant amount of impurities. This sample had a dark grey color. It should be noted, that synthesizing at higher temperatures resulted in melting of the mixture pellet.

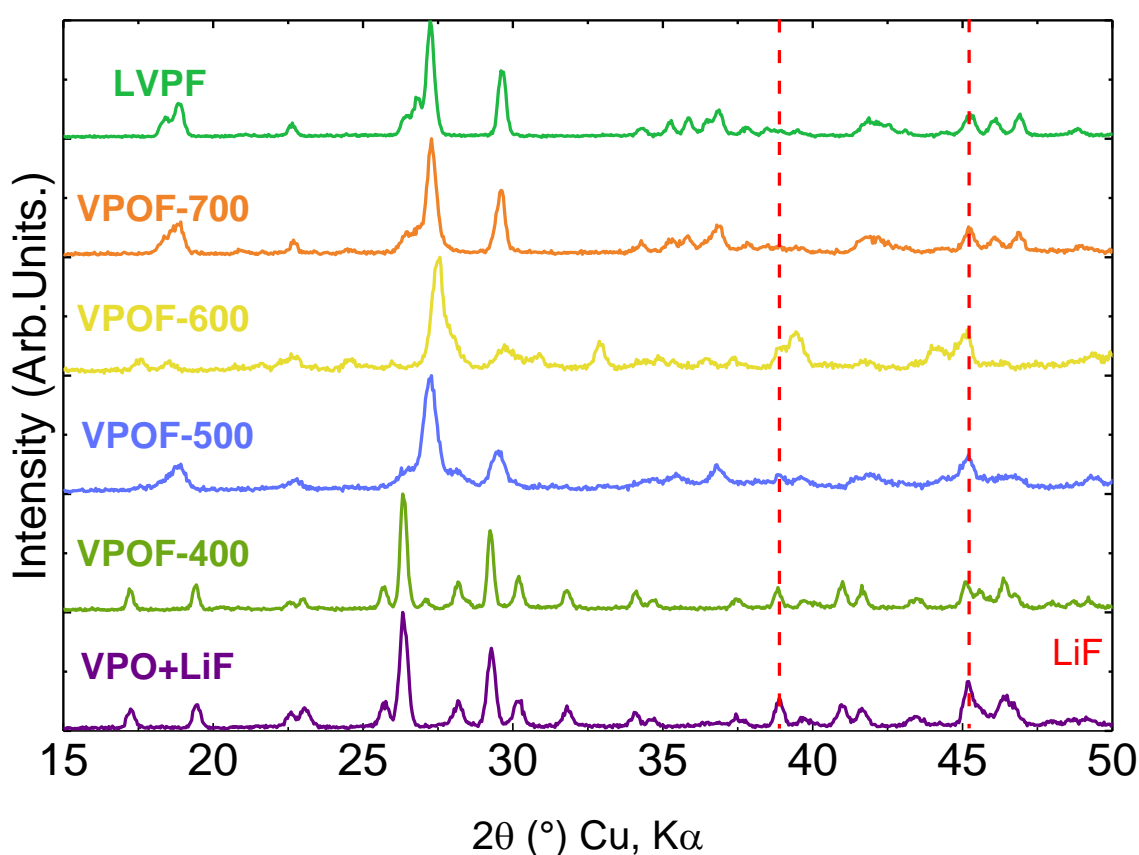


Figure 4-1 XRD patterns of β -VPO+LiF (VPOF) samples at RT and heat-treated at 400-700 °C. The red dashed lines show the position of LiF phase peaks.

The XRD patterns of the new phase in VPOF-700 sample and of LVPF are compared to each other in Figure 4-2. A lot of peaks from these two samples overlap. This shows that the newly-formed phase has a structure similar to LVPF (triclinic Tavorite framework). However, there are some differences in exact peak positions and intensities of LVPF and the new VPOF phase. This can indicate some possible structural differences between these two phases.

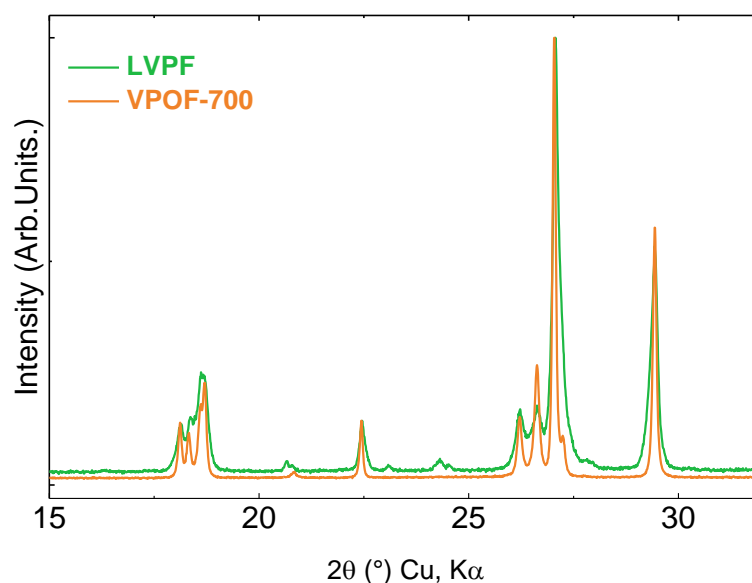


Figure 4-2 Comparison of XRD patterns of VPOF-700 and LVPF.

Microstructure of the VPOF-700 sample was comprised of large agglomerates of $>20\ \mu\text{m}$, which consisted of $1\text{-}2\ \mu\text{m}$ primary particles (Figure 4-3). These particles did not have any defined crystalline shapes and were formed in various and mostly undefined shapes. This followed the trend from precursor VPO, in which most of the particles did not have well-defined prismatic morphologies (Figure 3-6).

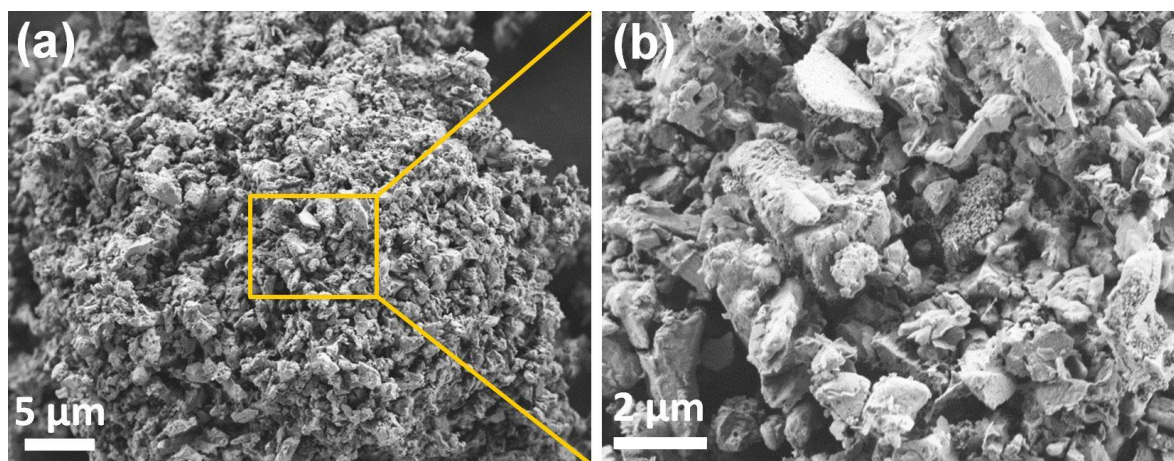


Figure 4-3 SEM micrographs of the sample VPOF-700, (a) at low magnification, showing the agglomerates and (b) at high magnification showing the single particles morphology.

For further analyzing the characteristics of the LiF-incorporated sample (VPOF-700), ^6Li MAS-NMR and ^{31}P MAS-NMR measurements were performed. In ^{31}P NMR (Figure 4-4a), a unique signal at 3870 ppm is observed. The spinning side bands are marked by asterisks. This signal is similar to the one from LVPF and shows that P has a similar

environment in VPOF-700 as in LVPF. Therefore, it can be claimed that the synthesized VPOF-700 has an LVPF-type structure, as was seen in the XRD results. In ^6Li NMR spectra, an intense signal is centered at 117 ppm (Figure 4-4b). This signal arises from Li environments associated with a unique Li crystallographic site and it is similar to the one from LVPF. Therefore, Li has a similar environment in both materials, which confirms the LVPF-type structure of the VPOF-700 phase. The signal at 0 ppm corresponds to the residual LiF impurity that was not detected by XRD due to its small quantity. The signals at 84 ppm and 186 ppm are assigned as vanadyl-type defects [Messinger, 2015], which means that this phase contains a significant amount of these defects in the structure that affect the Li environments. The signal at 150 ppm was also observed by Messinger *et al.* and was assigned to defects, but no further explanation was given. We suggest that this signal can also be due to Li-containing unknown impurities.

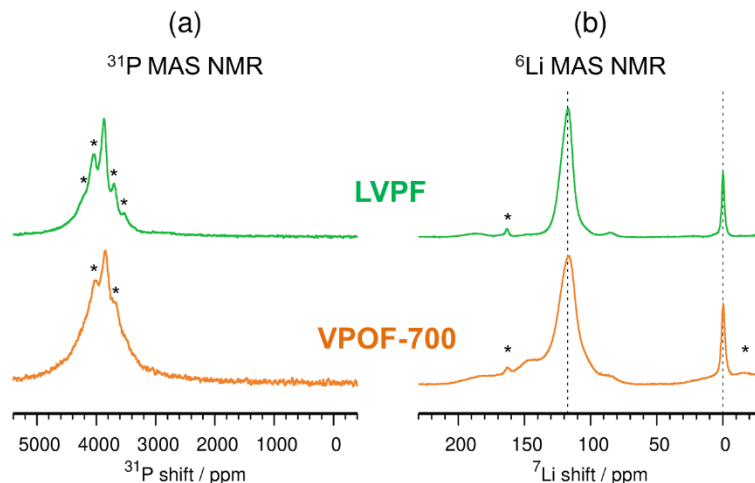


Figure 4-4 (a) ^{31}P MAS-NMR and (b) ^6Li MAS-NMR spectra of sample VPOF-700 in comparison to LVPF. The asterisks mark the position of spinning side-bands.

4.1.2. Electrochemical Analysis

The electrochemical properties of VPOF-700 sample were investigated by testing it as the cathode material in a half-cell using galvanostatic cycling. The second charge/discharge cycle performed with a C/50 cycling rate at high-voltage range and low-voltage range are shown in Figure 4-5a,b, respectively.

At high-voltage range (Figure 4-5a), Li extraction/insertion seems to take place at 3 steps, including two plateaus and a sloping voltage region. The first extraction/insertion plateau occurred at 4.04 V and continued for the exchange of $\sim 0.25 \text{ Li}^+$ that corresponded to $\sim 30\%$ of the whole capacity. The second step of Li exchange took place for about 0.15

Li^+ during a sloping voltage and the third extraction/insertion occurred at 4.21 V. The third step was the longest and about 0.45 Li^+ was exchanged during this reaction. The occurrence of these steps can indicate various reactions and possibly various phases within the active material. The first reaction at lower potential (4.04 V) can be attributed to an LVPO-type phase, although it has higher voltage than LVPO (3.95 V). This may be explained as a partially-fluorinated phase of LVPO. The associated reaction took place at a flat plateau which signifies a biphasic reaction. Therefore, such fluorinated phase formed as a single phase. However, the second Li extraction/insertion reaction occurred in a sloping voltage, which is indicative of solid-solution-type reaction. Finally, an LVPF-type phase was activated at the potential of 4.21 V during another biphasic reaction. The polarization in this region is comparable to the one from LVPF (Figure 3-29a). This observation is significant since it shows an effective intrinsic conductivity of this phase despite not having the additional carbon layer and larger particle size compared to LVPF (see SEM images of Figure 4-3 and Figure 3-28 for VPOF-700 and LVPF, respectively).

The charge/discharge cycle at low-voltage range is shown in Figure 4-5b. The main reaction took place at a potential of 1.8 V, which signifies once more the presence of LVPF-type phase (see Figure 3-29b). In addition, a sloping voltage reaction occurred in an insignificant amount of the cycling process that can be again attributed to a solid-solution phase.

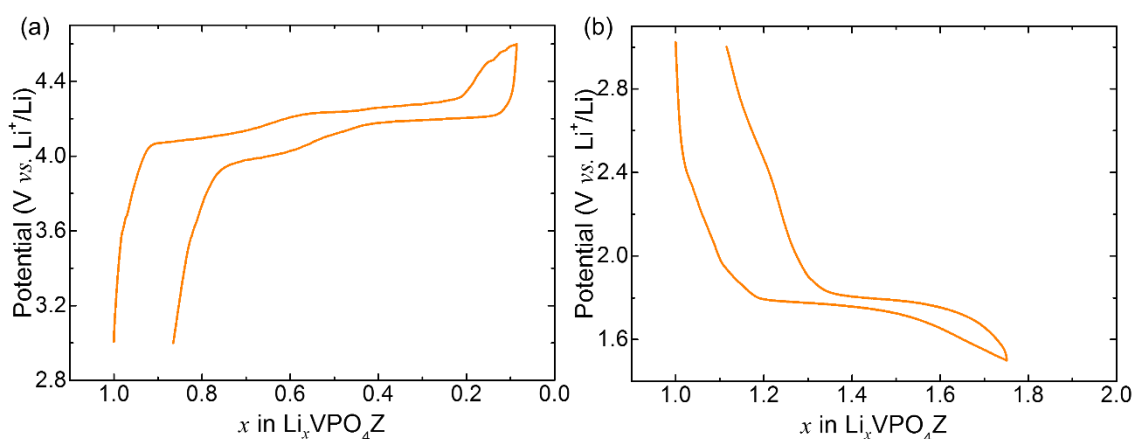


Figure 4-5 Galvanostatic cycling curve of the sample VPOF-700 at second cycle at (a) high-voltage range (3.0-4.5 V vs. Li/Li^+) and (b) low voltage range (1.5-3.0 V vs. Li/Li^+) with a current density corresponding to C/50 cycling rate.

In summary, a characteristically similar phase to LVPF was obtained as the main phase through incorporation of LiF in β -VPO. However, it was difficult to control the quality

of the obtained product. Various attempts were implemented to reproduce the synthesis in similar conditions that ended in different results. Therefore, an experiment was performed in order to tackle the irreproducibility issue. In this experiment, β -VPO sample was placed in the stainless-steel reactor and was heated for one hour at 700 °C. The XRD pattern of the sample after heat-treatment is shown in Figure 4-6. Phase matching showed no presence of β -VPO and instead two phases, namely VPO_4 and $(VO)_2P_2O_7$ were formed. These two phases respectively contain vanadium in +3 and +4 oxidation state, which are lower than +5 oxidation state in β -VPO. Therefore, β -VPO actually undergoes a vanadium reduction decomposition in the synthesis medium of the stainless-steel autoclave. Reduction of β -VPO causes a different reaction path in the presence of LiF than intended. In addition, it makes the synthesis rather uncontrollable and dependent on the degree of decomposition. The obtained VPOF phase is an LVPF-type phase, having a +3 vanadium oxidation state, which most likely have formed upon the reaction of decomposition product VPO_4 and LiF.

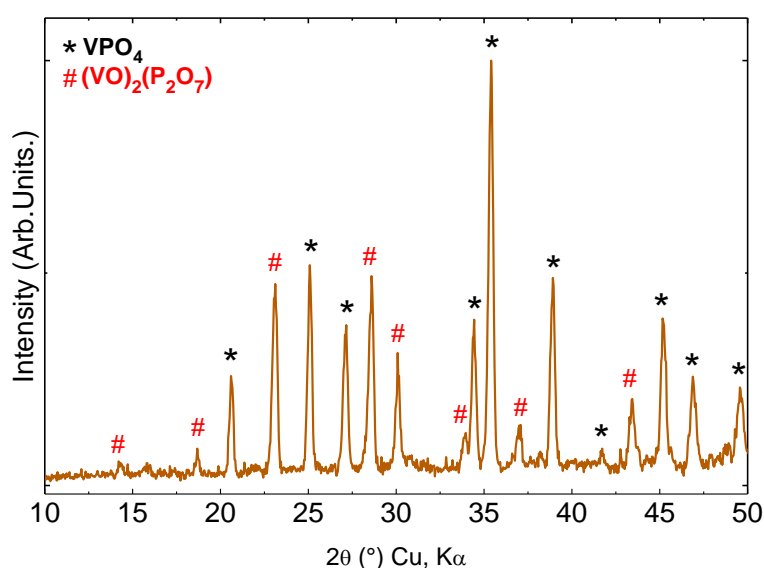


Figure 4-6 XRD pattern of the product obtained through heat-treatment of β -VPO in the stainless steel reactor.

4.1. Fluorination of ϵ -LiVPO₄O by LiF

The second vanadyl phosphate used for fluorination through incorporation of LiF was ϵ -LVPO. ϵ -LVPO has a Tavorite-type structure similar to LVPF. Therefore, its fluorination by LiF can give significant insights in the fluorination mechanism, phase formation and the effect of fluorine on the material properties in direct comparison with LVPF. In this

section, results of such synthesis process with structural and electrochemical characterization of the materials are presented.

4.1.1. Synthesis and Characterization

The as-synthesized ϵ -LVPO powder (at 700 °C, 12 h) was mixed in stoichiometric amounts with LiF (Equation 4-2) and ground using a mortar and pestle. Then pellets with the typical weight of 150-200 mg were pressed with ~200 MPa pressure. The pellets were subsequently introduced into a golden tube inside the stainless-steel reactor, which was sealed inside an argon-filled glovebox. The heat-treatments were carried out at various temperatures of 600 °C (LVPOF-600), 700 °C (LVPOF-700) and 800 °C (LVPOF-800) for 1 h and then the reactors were immediately quenched in liquid nitrogen for 30 s.



The color of the powders recovered after heat treatment was brown, ranging in the light to dark shades, with light shades corresponding to lower and dark to higher synthesis temperature. The XRD patterns of synthesized powders (LVPOF-600, LVPOF-700 and LVPOF-800) are presented in Figure 4-7 in selected 2θ regions chosen to emphasize the main peaks. For the sake of comparison, XRD patterns of unheated mixture of ϵ -LVPO and LiF as well as of LVPF are shown. An increase in temperature from 600 °C to 800 °C resulted in a decrease in the intensity of LiF and ϵ -LVPO peaks (marked respectively by circles and asterisks on the ϵ -LVPO+LiF pattern). Simultaneously, peaks of a new phase appeared (blue vertical dashed lines), which increased in intensity from LVPOF-600 to LVPOF-800. At the highest heating temperature of 800 °C (LVPOF-800), the pattern comprises mainly of the new phase with only minor impurities in the form of LiF, ϵ -LVPO and Li_3PO_4 phases. Note, that the XRD pattern of the newly formed LVPOF phase is noticeably different from that of the LVPF phase (green pattern in Figure 4-7). The nominal composition of the expected product of complete reaction according to Equation 4-2 was $\text{Li}_2\text{VPO}_4\text{OF}$. However, the presence of the LiF peaks in the XRD pattern implied an incomplete LiF consumption during the synthesis. Therefore, the amount of LiF is noted as x (with $x < 1$) in Equation 4-3, which is a more accurate representation of the reaction taken place.



The chemical formula of the new phase (LVPOF) can be defined as $\text{Li}_a\text{VPO}_4\text{O}_b\text{F}_c$ ($a \geq 1$, $b, c < 1$). The exact amounts of a , b and c values are not definite and could undergo minor variation depending on the synthesis temperature. The presence of trace impurities prevented accurate measurement or calculation of composition.

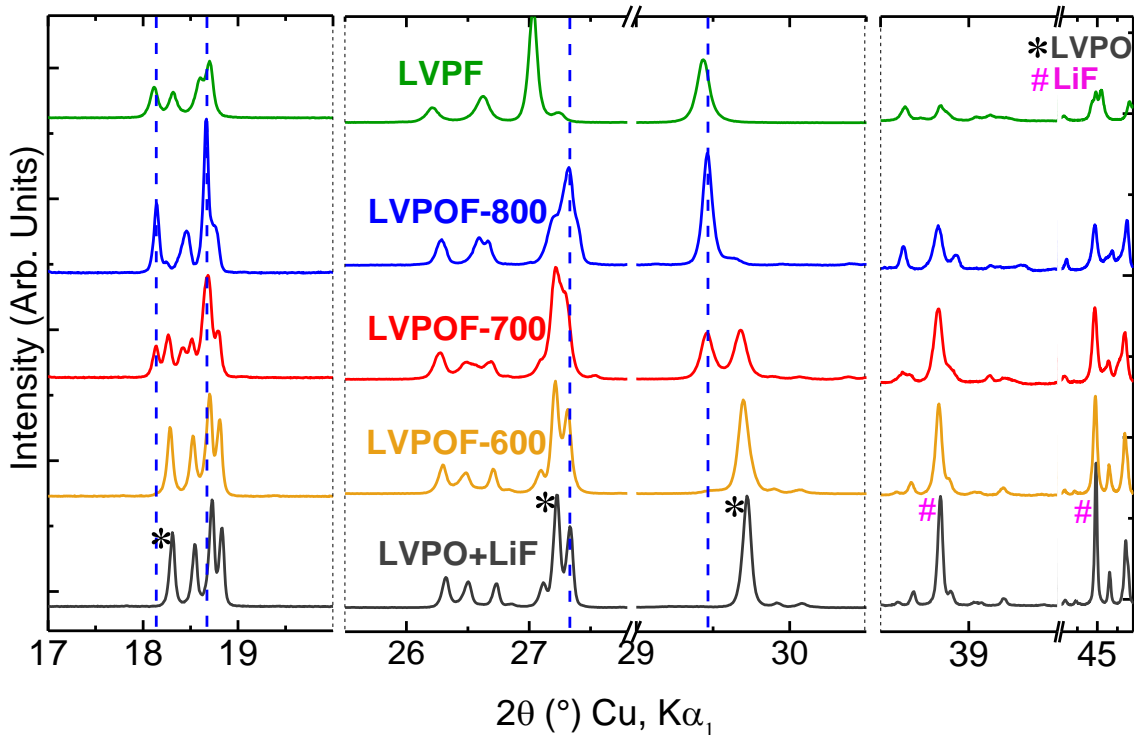


Figure 4-7 XRD patterns of LVPOF samples heat-treated at 600 °C, 700 °C and 800 °C (LVPOF-600, LVPOF-700 and LVPOF-800, respectively) in a comparison with LVPO+LiF and LVPF samples. The patterns are shown in the selected 2θ regions chosen to emphasize the main peaks. Asterisks represent some of ϵ -LVPO peaks and hashes represent LiF peaks. Blue dashed lines show the location of LVPOF peaks, adapted from [Semsari Parapari, 2020].

The lattice parameters of all three samples (LVPOF-600, LVPOF-700 and LVPOF-800) were refined starting from the lattice parameters of ϵ -LVPO (ICSD#: 184602). Note, that the refinement performed starting with the lattice parameters of LVPF (ICSD#: 184601) did not converge to acceptable reliability factors. The lattice parameters of LVPOF phase in each sample are reported in Table 4-1. The refinement results showed that the evolution of the cell parameters does not follow a specific trend. However, the unit cell volume of the LVPOF phase in all three samples was higher than in the precursor ϵ -LVPO phase. This was an expected result of the LiF incorporation into the ϵ -LVPO structure. Moreover, the unit cell volume of the LVPOF phase increased with the increase of temperature from 600 °C to 800 °C. This indicates that by applying higher temperature

while keeping the same heat-treatment time, the incorporation of the LiF into the structure was promoted. However, further increase of the temperature resulted in melting of ϵ -LVPO and LiF mixture.

Table 4-1 Lattice parameters of LVPOF phase in LVPOF-600, LVPOF-700 and LVPOF-800 samples, determined from LeBail refinement.

	LVPOF-600	LVPOF-700	LVPOF-800
a (Å)	6.806(4)	6.809(7)	6.810(9)
b (Å)	7.172(9)	7.173(5)	7.182(6)
c (Å)	7.931(1)	7.927(9)	7.928(6)
α (°)	89.96(4)	89.979(1)	89.943(7)
β (°)	91.454(3)	91.479(6)	91.475(9)
γ (°)	117.28(5)	117.21(8)	117.249(6)
V (Å ³)	344.15(9)	344.24(6)	344.68(1)

The morphology and particle size of the synthesized powders were examined by SEM. Figure 4-8 shows the SEM micrographs of LVPOF samples. LVPOF-600 did not differ much from ϵ -LVPO (Figure 3-12) in size and morphology of particles. The SEM images of the LVPOF-700 sample exhibited a slightly different morphology. The particles mostly lack the defined shape seen in the precursor ϵ -LVPO sample. Furthermore, the LVPOF-800 sample constituted mainly of poorly defined particles, although larger in size (up to 10 μm). In general, there was a wider range of particles size in this sample. It should be noted that in the SEM images, the impurities such as LiF and Li_3PO_4 cannot be distinguished from the main LVPOF phase particles. In addition, LVPOF sample particles differed tremendously in size from LVPO sample, where the average particle size was below 1 μm (Figure 3-28).

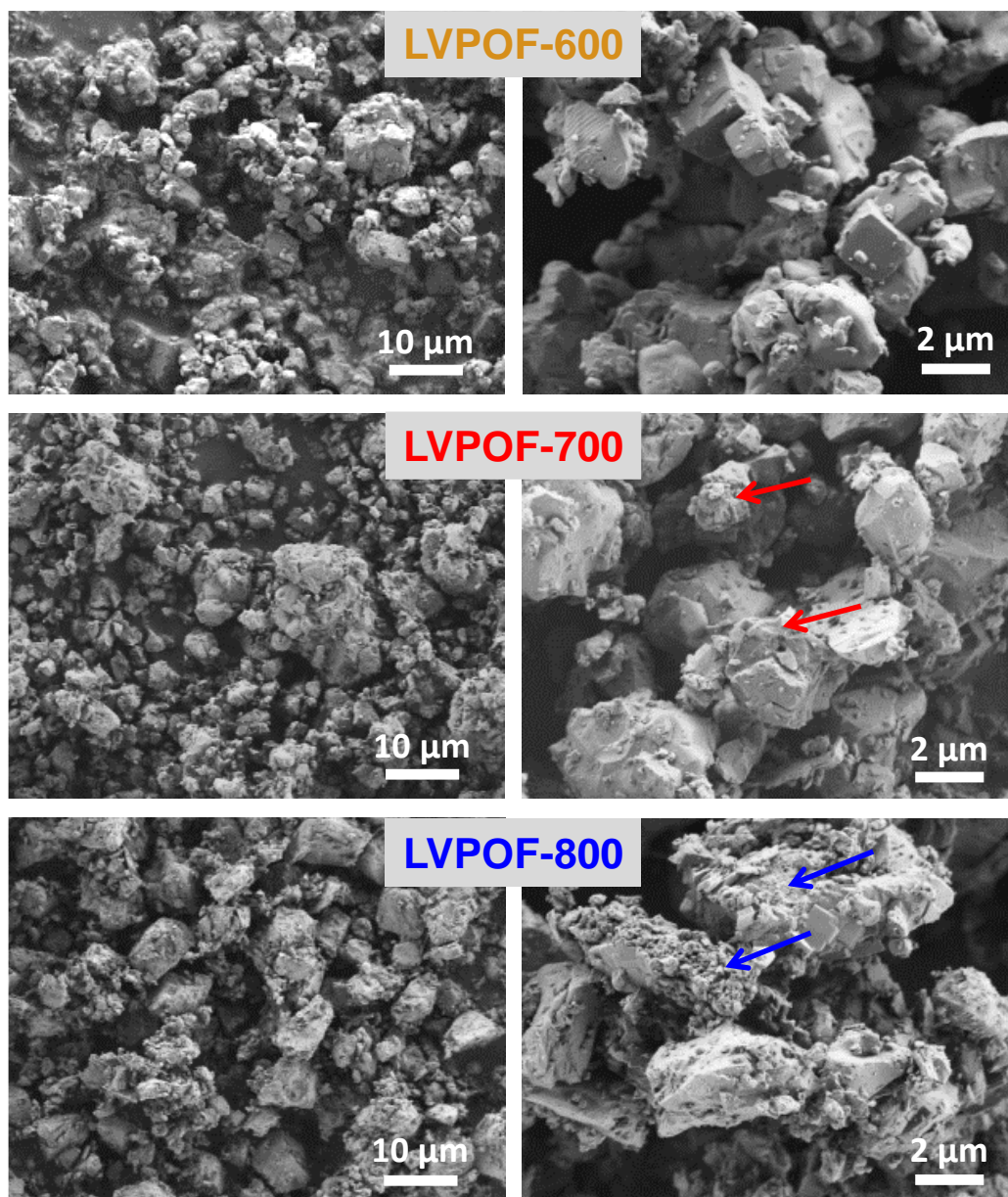


Figure 4-8 SEM micrographs of LVPOF-600, LVPOF-700 and LVPOF-800 powder samples in two different magnifications (left, lower and right, higher magnification). The arrows show the new LVPOF phase, adapted from [Semsari Parapari, 2019].

Prior to the detailed analysis of XRD patterns, XANES experiments were performed in order to assess the average oxidation state of V and its local symmetry as well as to evaluate the effects of fluorination. For that, the V K-edge XANES spectra were taken from all three LVPOF samples in addition to ϵ -LVPO and LVPF samples (Figure 4-9a). The shape of the edge profile and the pre-edge peaks are correlated with the local symmetry of vanadium sites, while their energy positions are correlated with the valence state of V cations [Boivin, 2018][Wong, 1984][Dominko, 2011][Pivko, 2012]. Octahedrally-coordinated vanadium cations that possess an inversion center (for example

in V_2O_3 [Wong, 1984] or LVPF [Kim, 2017]) exhibit a weak triplet resonance structure in the pre-edge region. On the other hand, vanadium cations located at sites without an inversion center (for example tetrahedrally-coordinated in $CrVO_4$ [Wong, 1984], square pyramidal in V_2O_5 [Wong, 1984], or distorted octahedrally-coordinated in V_2O_4 [Wong, 1984], Li_2VTiO_4 [Dominko, 2011] or LVPO [Kim, 2017]) exhibit a characteristic isolated pre-edge peak. The pre-edge feature is assigned to 1s to 3d transition, which is forbidden in perfectly regular vanadium octahedron. This transition becomes dipole allowed with the distortion of the local symmetry around vanadium cations, which leads to 3d–4p orbital mixing. As demonstrated by Boivin *et al.* [2018], the intensity of the pre-edge peak is highly sensitive to the local distortions around vanadium in the LVPF-type $LiVPO_4F_{1-y}O_y$ system and gives insights into its local environments. The XANES spectra of LVPOF-600, LVPOF-700 and LVPOF-800 samples (Figure 4-9a) exhibited edge profiles with a pre-edge peak. Comparison of the XANES spectra showed gradual decrease of the pre-peak intensity with increasing synthesis temperature. LVPOF-600 exhibited almost the same pre-edge peak intensity as ϵ -LVPO sample, while in LVPOF-800, the intensity of the pre-edge peak was reduced almost to half of ϵ -LVPO value. Such decrease in the intensity of pre-edge peak is ascribed to the increasing ϵ -LVPO fluorination, which imposes higher symmetry *i.e.* lower distortion in V octahedra.

In addition to the pre-peak intensity, the energy shift of the vanadium absorption edge that commonly correlates with V valence was also evaluated from the XANES spectra. Generally, the increase in the V valence state is associated with the shift of the edge towards higher energies, with a shift of about 2.5 eV per valence in case of vanadium oxides [Wong, 1984][Pivko, 2012]. The absorption edges in LVPOF-600 and LVPOF-700 were found to be very close to the energy position of ϵ -LVPO sample (see Figure 4-9a), while LVPOF-800 edge was shifted ~ 0.8 eV to lower energies. This would imply a general trend of the reduction in V valence state of LVPOF samples coinciding with the increase in heat treatment temperature. The LVPF sample exhibited shift of 1 eV compared to ϵ -LVPO, which correlates with lower V valence in this structure. It should be noted, however, that the energy shifts of the absorption edge are additionally affected by the electronegativity of the ligands and the local structure of V cations [Wong, 1984][Dominko, 2011][Pivko, 2012].

XANES spectra of the reference samples (Figure 4-9b) showed that the V absorption edge position correlation in vanadium oxy/fluoro-phosphate compounds cannot be done

unambiguously. Spectrum of VO_2F (V^{5+}) fluoride reference sample revealed the -0.5 eV edge shift to the lower energies compared to the spectra of the V_2O_5 (V^{5+}) and VPO_4O (V^{5+}) oxides due to a presence of F in the neighborhood of vanadium. Furthermore, VF_3 (V^{3+}) edge is overlapping with the precursor ϵ -LVPO (V^{4+}), while reference LVPF (V^{3+}) edge is shifted about -0.5 eV relative to VF_3 (V^{3+}). Therefore, the shifts in the V absorption edge position cannot be related only to V average valence state without considering the differences in the structure and ligands (fluorination) of compared materials. The observed shifts of vanadium edge to lower energies with increasing treatment temperature in samples LVPOF-600, LVPOF-700 and LVPOF-800 can be ascribed partially to the reduction of vanadium and partially to the effect of increased fluorination at higher temperatures.

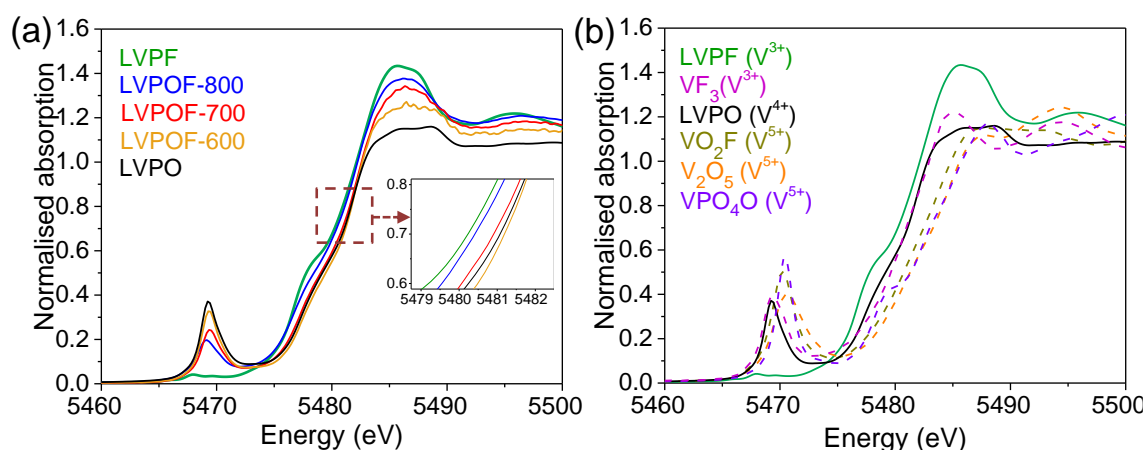


Figure 4-9 V K-edge XANES spectra of (a) LVPOF-600, LVPOF-700, and LVPOF-800 samples in a comparison to ϵ -LVPO precursor and LVPF; and (b) reference VO_2F , V_2O_5 , VPO_4O , VF_3 and ϵ -LVPO and LVPF samples [Semsari Parapari, 2019].

Further, to explore the local environment of atomic species, ^{31}P MAS NMR and ^7Li MAS NMR spectroscopy measurements were performed. In Figure 4-10a, ^{31}P MAS NMR spectra of LVPOF-600, LVPOF-700 and LVPOF-800 samples are compared to the spectra of ϵ -LVPO precursor and LVPF. The two signals at 1600 ppm and 1420 ppm suggested the presence of two different types of P, which is in accordance with the two crystallographic sites observed in the pure ϵ -LVPO [Ateba Mba, 2013]. This pointed out that after the incorporation of LiF in LVPO, the host structure of ϵ -LVPO was maintained. Note that both LVPOF and ϵ -LVPO phases present in the samples contributed to these signals. The ^{31}P MAS NMR spectrum of the LVPOF-800 sample showed a sharp and rather intense signal at 0 ppm, corresponding to a diamagnetic impurity, Li_3PO_4 , and also

a very weak, broad signal at about 3900 ppm, indicating the presence of a small fraction of a LVPF-type phase [Messinger, 2015].

^7Li MAS NMR spectra of the LVPOF-600, LVPOF-700 and LVPOF-800 samples showed a sharp peak at -2 ppm (Figure 4-10b), corresponding to the remaining LiF (and of Li_3PO_4 in case of LVPOF-800). All the three samples exhibited a signal at about 80 ppm, which can be assigned to Li nuclei in the ϵ -LVPO type of environment. Indeed, Li atoms occupy two different crystallographic sites in LVPO, but their ^7Li NMR signals cannot be resolved, because the two local environments are similar [Ateba Mba, 2013].

A closer look at the ^7Li MAS NMR spectra of LVPOF-600, LVPOF-700 and LVPOF-800 (Figure 4-10c) showed how LVPOF gradually transformed from a structure in which Li nuclei occupied only typical ϵ -LVPO sites and exhibit NMR signal at ~ 80 ppm (LVPOF-600), to a structure in which numerous different Li environments could be found (LVPOF-800). Li nuclei experiencing these different environments gave rise to a set of strongly overlapped signals resonating between 75 ppm and 190 ppm. Qualitatively, the ^7Li MAS NMR spectrum of LVPOF-800 has similarities to the spectrum of previously reported $\text{LiVPO}_4\text{F}_{0.25}\text{O}_{0.75}$ material [Boivin, 2017]. The contribution resonating close to 120 ppm most probably corresponds to Li within the LVPF type of environment (this phase was already detected by ^{31}P NMR). The assignment of the overlapped signals at about 75, 90, 150 and 190 ppm was not clear. Whereas signals at 84 and 186 ppm were assigned to vanadyl-type defects, the above listed various contributions to the ^7Li MAS NMR spectrum of LVPOF-800 could stem from variations in Li environments. This can be small shifts of the existing positions of Li atoms due to F introduction, i.e. different distances in their neighborhood. Other possibilities include Li nuclei seeing vanadium centers in different oxidation states which is known to be possible [Bianchini, 2014] and/or incorporation of additional Li atoms stemming from LiF into new sites in LiVPO_4O -type structure. Either of these could lead to differently strong hyperfine interactions between the electronic spins of vanadium centers and lithium nuclei and thus to significant shifts of the NMR resonances. Note that the relative intensities of the shifted signals were at least comparable to the intensities of the 80 ppm and 120 ppm signals (corresponding to the typical ϵ -LVPO and LVPF sites, respectively), meaning that in LVPOF-800 there were significant fractions of different lithium environments.

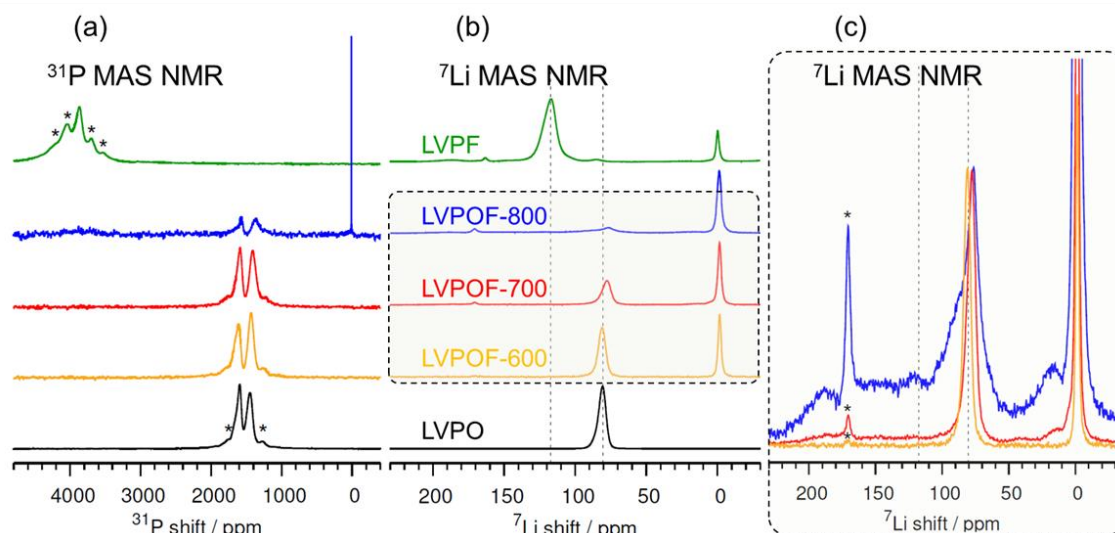


Figure 4-10 ^{31}P (a) and ^7Li (b) and (c) MAS NMR spectra of LVPOF-600, LVPOF-700, and LVPOF-800 samples in comparison to ε -LVPO precursor and LVPF. Asterisks denote spinning sidebands. In (b), ^7Li NMR spectra are vertically scaled so that the highest signals of different spectra are equally high, whereas in (c) they are scaled so that the signals at cca 80 ppm within the different spectra are equally high. Vertical dotted lines mark the positions of the ^7Li resonances of ε -LVPO and LVPF [Semsari Parapari, 2019].

The XRD and NMR findings showed that the crystal structure of the precursor ε -LVPO is maintained after LiF incorporation. Therefore, the precursor ε -LVPO and the synthesized LVPOF are isostructural. ε -LVPO phase crystallizes in Amblygonite type structure due to the small α angle, which differs from the isostructural Montebasite structure. ($\alpha_{\text{Amblygonite}} < 90^\circ < \alpha_{\text{Montebasite}}$) [Groat, 1990][Groat, 2003].

The atomic parameters were refined for the LVPOF-800 sample by Rietveld method starting from the structural model of ε -LVPO (ICSD No. 184602) (Figure 4-11 and Table 4-2). In LVPOF structure, one can expect the presence of randomly distributed F atoms as the ligand bridging two V octahedra along the b axis. In order to take into account the presence of fluorine in the LVPOF-800 sample, the refinement was carried out assuming F substitution *i*) in either O(5) or O(6) and *ii*) in both O(5) and O(6). In the first case of substitution (either O(5) or O(6)), the refinement of the XRD data delivered poor reliability factors for the minimization of the intensity difference. In the second case, where both O(5) and O(6) positions were substituted with F, reliability factor reached satisfactory values. The best fit was achieved when the occupancy factor of O(5) and O(6) were respectively linked to F(1) and F(2). The occupancy factor for O(5), O(6), F(1) and F(2) were obtained respectively as 0.750(3), 0.846(1), 0.250(3) and 0.153(8). The

substitution of F in the defined O positions of the octahedral ligands showed that b and c values in Equation 4-3 are linked to each other in the suggested chemical notation ($\text{Li}_a\text{VPO}_4\text{O}_b\text{F}_c$) in the synthesis section. Thus, it is safe to reformulate the chemical notation of the LVPOF phase as $\text{Li}_a\text{VPO}_4\text{O}_b\text{F}_{1-b}$ ($a \geq 1$, $b < 1$), which according to the refined values can then be estimated as $\text{Li}_a\text{VPO}_4\text{O}_{0.8}\text{F}_{0.2}$ for LVPOF-800 phase. The O and F values are calculated as the average amounts obtained for refinement of O(5), O(6), F(1) and F(2). Note, that Li position was not refined due to its low X-rays atomic scattering factor.

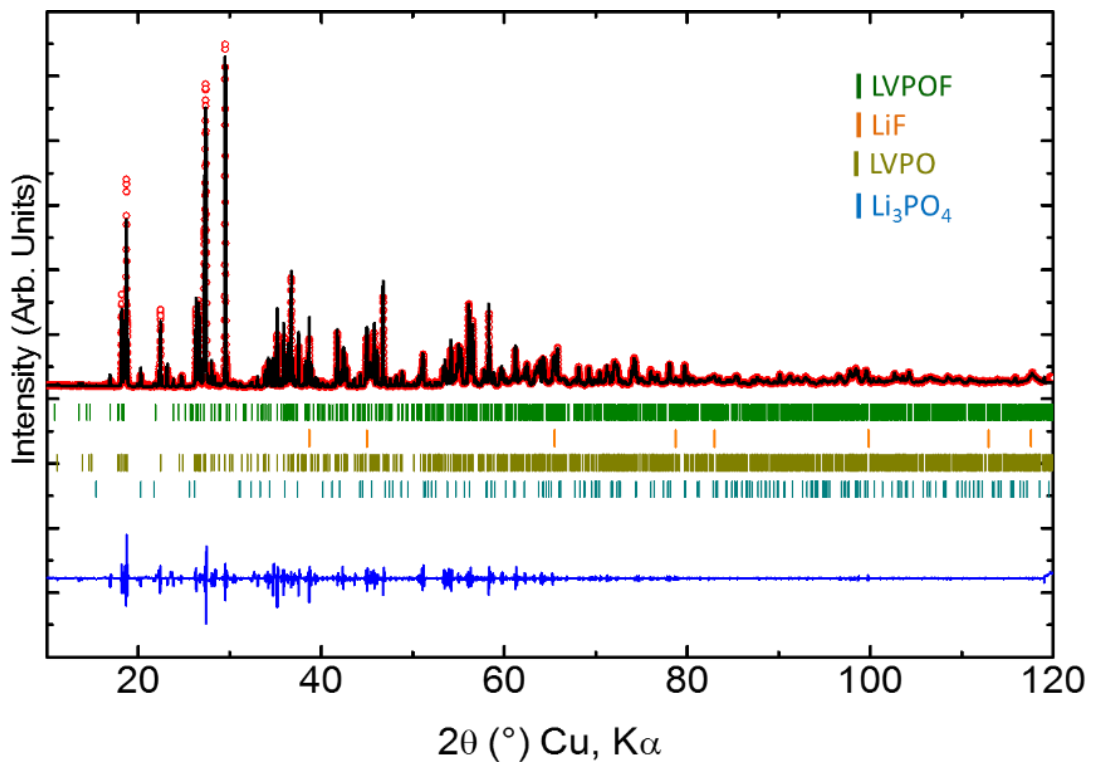


Figure 4-11 Rietveld refinement of LVPOF-800 sample based on X-ray powder diffraction pattern. The observed, calculated and difference curves are presented as red dots, black line and blue lines, respectively. The theoretical Bragg positions of LVPOF (green), LiF (orange), ϵ -LVPO (dark yellow) and Li_3PO_4 (blue) are also shown [Semsari Parapari, 2019].

Table 4-2 Atomic parameters obtained by Rietveld refinement of XRD pattern of LVPOF-800 sample (the structure of ϵ -LVPO phase was used for refinement) [Semsari Parapari, 2019].

Atomic parameters					
Atoms	Wyckoff position	Atomic position			Occ
		x/a	y/b	z/c	
V(1)	2i	0.2581(9)	-0.0027(8)	0.7403(2)	1
V(2)	2i	0.2617(2)	-0.5283(4)	0.7457(8)	1
P (1)	2i	0.2205(5)	-0.2558(9)	0.0766(4)	1
P(2)	2i	0.2989(3)	-0.7197(8)	0.3982(3)	1
O(1)	2i	0.5890(1)	0.1209(3)	0.7974(9)	1
O(2)	2i	0.1254(2)	-0.1138(7)	0.9936(1)	1
O(3)	2i	-0.0776(4)	-0.1272(9)	0.6812(5)	1
O(4)	2i	0.3757(2)	0.138(1)	0.5082(4)	1
O(5)	2i	0.2533(2)	-0.2775(8)	0.6458(1)	0.750(3)
F(1)	2i	0.2533(2)	-0.2775(8)	0.6458(1)	0.250(3)
O(6)	2i	0.2852(2)	0.2302(8)	0.8096(7)	0.846(1)
F(2)	2i	0.2852(2)	0.2302(8)	0.8096(7)	0.153(8)
O(7)	2i	0.0809(0)	-0.3847(9)	0.2307(2)	1
O(8)	2i	0.3089(1)	-0.3815(1)	-0.0149(4)	1
O(9)	2i	0.3940(8)	-0.6582(8)	0.2174(2)	1
O(10)	2i	0.1809(5)	-0.6250(6)	0.5133(3)	1
Li(1)	2i	0.204(0)	-0.688(0)	0.075(0)	1
Li(1)'	2i	0.273(0)	-0.207(0)	0.409(0)	1

The Tavorite-type structure of LVPOF phase is shown in Figure 4-12a, where VO_4X_2 octahedra (with $\text{X}=\text{O}/\text{F}$) are connected through corner-sharing with PO_4 tetrahedra. The vanadium octahedra are connected to each other via O/F ligands.

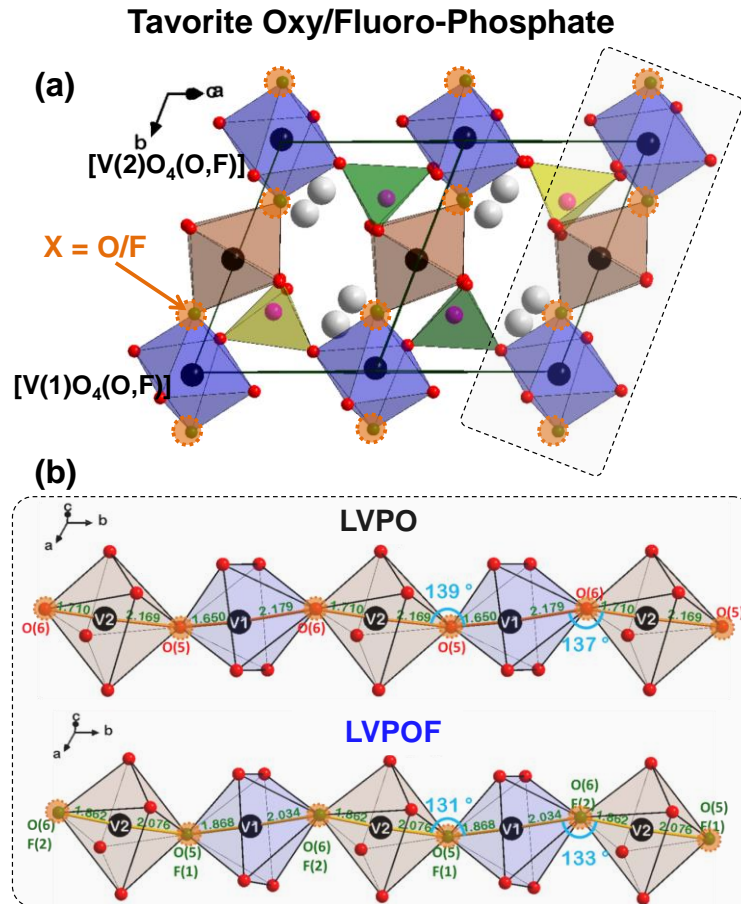


Figure 4-12 a) Representation of Tavorite-type structure of LVPOF. b) Comparison of chains of $\cdots[V(1)O_4X_2]-[V(2)O_4X_2]\cdots$ (with $X=O, O/F$) in ϵ -LVPO and LVPOF [Semsari Parapari, 2020].

The V octahedral chains (VO_4X_2 (with $X = O$ or F ligand)) in ϵ -LVPO are compared to the ones in LVPOF phase in Figure 4-12b. The V1-O/F and V2-O/F long bonds in corresponding $V(1)O_4X$ and $V(2)O_4X$ octahedra in LVPOF are shorter than those in ϵ -LVPO, while the V1-O/F and V2-O/F short bonds are longer. This leads to a higher general symmetry of the V-X bonds in VO_4X_2 octahedral chains of LVPOF. The higher symmetry of the V octahedra was also observed previously in XANES results as the lower pre-edge intensity in the spectrum of LVPOF sample compared to the one for ϵ -LVPO sample. Furthermore, it can be noted from comparing the bond lengths in Figure 4-12b, that F substitution of O has a higher impact on the elongation of strongly covalent $V=O$ vanadyl bond, rather than on the shortening, *i.e.* strengthening, of the weaker V-O bond. In addition, the V-X-V angles in LVPOF are smaller (131° and 133°) than the ones in ϵ -LVPO (139° and 137°). This indicates a shrinking of the octahedral chains in the b direction in LVPOF compared to LVPO.

4.1.1. Electron microscopy

The crystal structure and atomic arrangements of both ϵ -LVPO and LVPOF-800 were investigated by means of SAED and STEM imaging. The LVPOF-800 sample was chosen for more thorough investigations since it had the highest amount of the new LVPOF phase with the least amount of impurities. The SAED patterns collected from the single LVPOF and ϵ -LVPO particles confirmed the high crystallinity of the material (Figure 4-13a, b). Both diffraction patterns were simulated using the *JEMS* software [Stadelmann, 2011]. Corresponding structure models, *i.e.* ICSD No. 184602 for the LVPO, and the new experimentally derived (XRD) crystallographic information file (CIF) for the LVPOF were used as the input structures. The ϵ -LVPO pattern showed a good fit, while small displacements between the *JEMS* simulated (inset in Figure 4-13a) and the experimental LVPOF pattern were detected already in the second order SAED reflections. Since XRD pattern is collected from a millimeter-scale area of the sample, its information on the crystal structure is much less spatially resolved compared to the TEM-SAED. Therefore, the differences between the LVPOF SAED pattern and the experimental CIF file can be attributed to the nanometers-scale variations of the crystal structure due to the distribution of the O/F ligand. This goes in accordance with the previously described results of XRD, XAS and NMR.

The STEM-HAADF images of LVPOF-800 and ϵ -LVPO (Figure 4-13c and Figure 4-13d respectively), also confirmed a high crystallinity of both materials. Both images were taken in the same $[-101]$ zone axis but with different structure rotation (yellow dashed line in Figure 4-13c, d, e denotes the same structural plane). The contrast variations in the STEM-HAADF images correspond to the differences in the atomic numbers of the V and P (23 and 15, respectively), with the V atomic columns producing higher intensity. Model of the LVPOF atomic structure in the $[-101]$ zone axis is shown in Figure 4-13e, f. The sizes of the Li, O, F, P and V atoms in the atomic structure drawing were normalized according to the atomic number, with V being the highest. A uniform contrast of the V and P atomic columns implies that there were no detectable defects on the V and P sublattices. The intensity line profile insets in Figure 4-13c, d were taken along the yellow dashed lines, which run along the plane that consists of slightly overlapping V and O atomic columns. O columns are invisible in this case due to the small distances and vicinity of the heavier V columns that produce higher intensity (Figure 4-13e, f). The direct visualization of the O/F ligand atomic columns was not possible neither by HAADF

nor by ABF STEM-imaging due to the very dense atomic packing observed in the $[-101]$ zone axis (Figure 4-14). Therefore, further STEM-EDS and STEM-EELS studies were performed to assess the local elemental composition as well as the electronic surrounding of the vanadium.

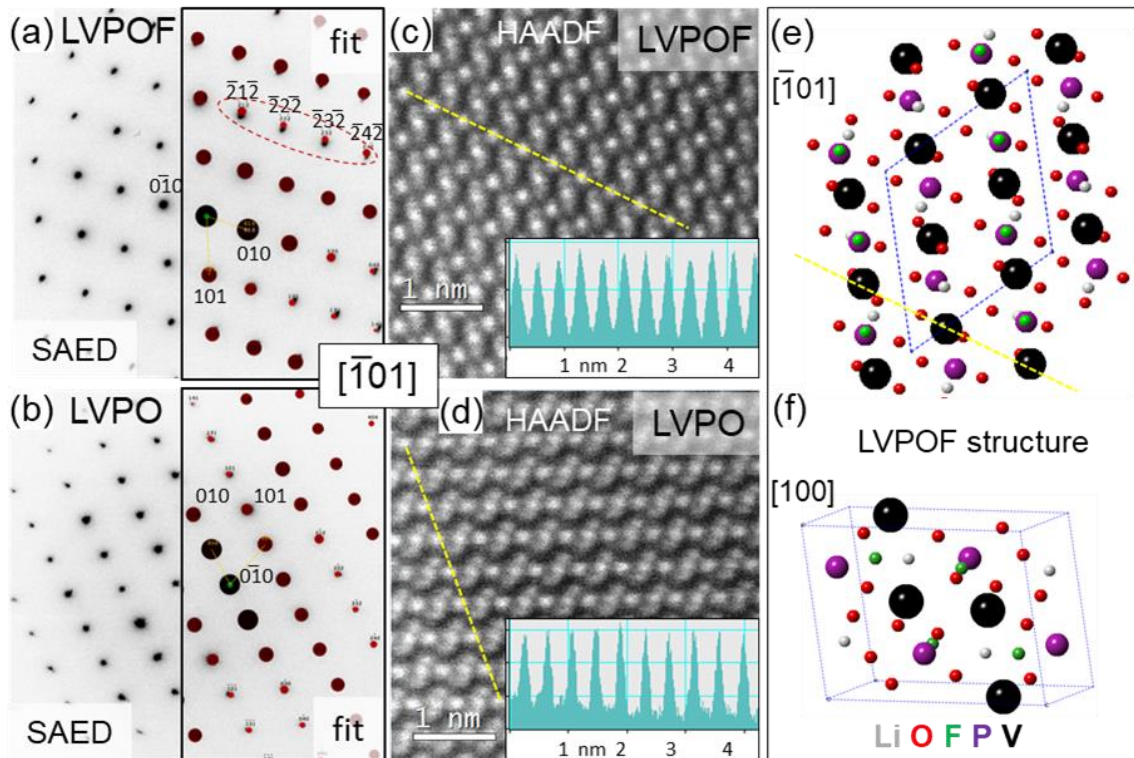


Figure 4-13 (a, c) SAED experimental patterns along with patterns simulated using *JEMS* software (Stadelmann, 1999) for LVPOF-800 and ϵ -LVPO samples, respectively. STEM-HAADF images of (b) LVPOF-800 and (d) ϵ -LVPO samples, with the line intensity profiles in the insets. Yellow dashed line denotes the intensity profile position. (e) Atomic structure of the LVPOF phase viewed in the $[-101]$ direction along with the (f) unit cell atomic structure of LVPOF phase pictured close to $[100]$ direction, with blue dashed lines denoting unit cell borders [Semsari Parapari, 2020].

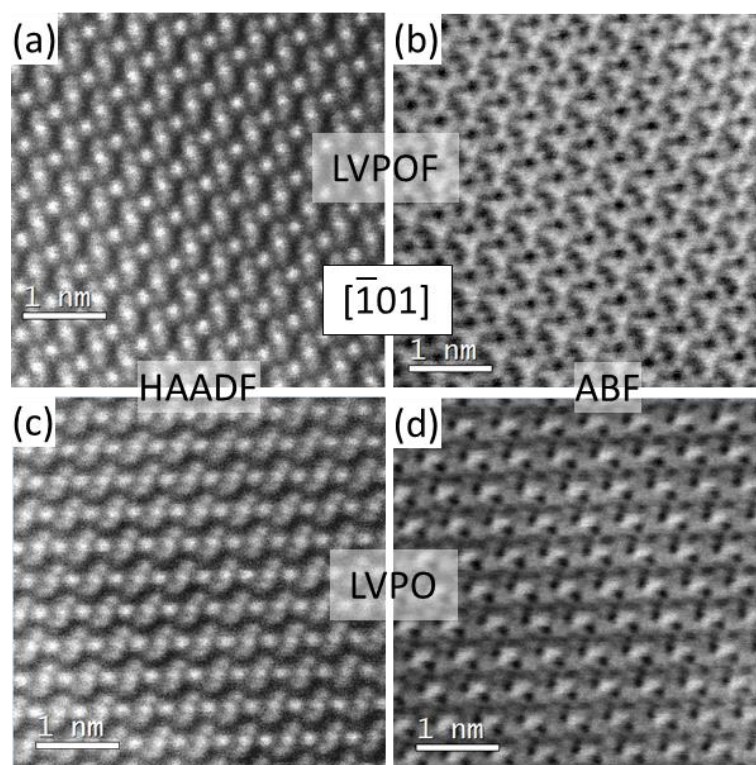


Figure 4-14 STEM-HAADF and corresponding STEM-ABF images of LVPOF-800 (a,b) and ϵ -LVPO (c,d) samples [Semsari Parapari, 2020].

The homogeneity of the F incorporation on the nano-scale as well as overall chemical composition was studied by STEM-EDX analysis of individual particles of LVPOF-800 sample. The STEM-EDX mapping of V, P, and O taken from a single particle shown in Figure 4-15 confirmed a homogeneous distribution of these elements. Note that Li is not detectable by the EDX technique.

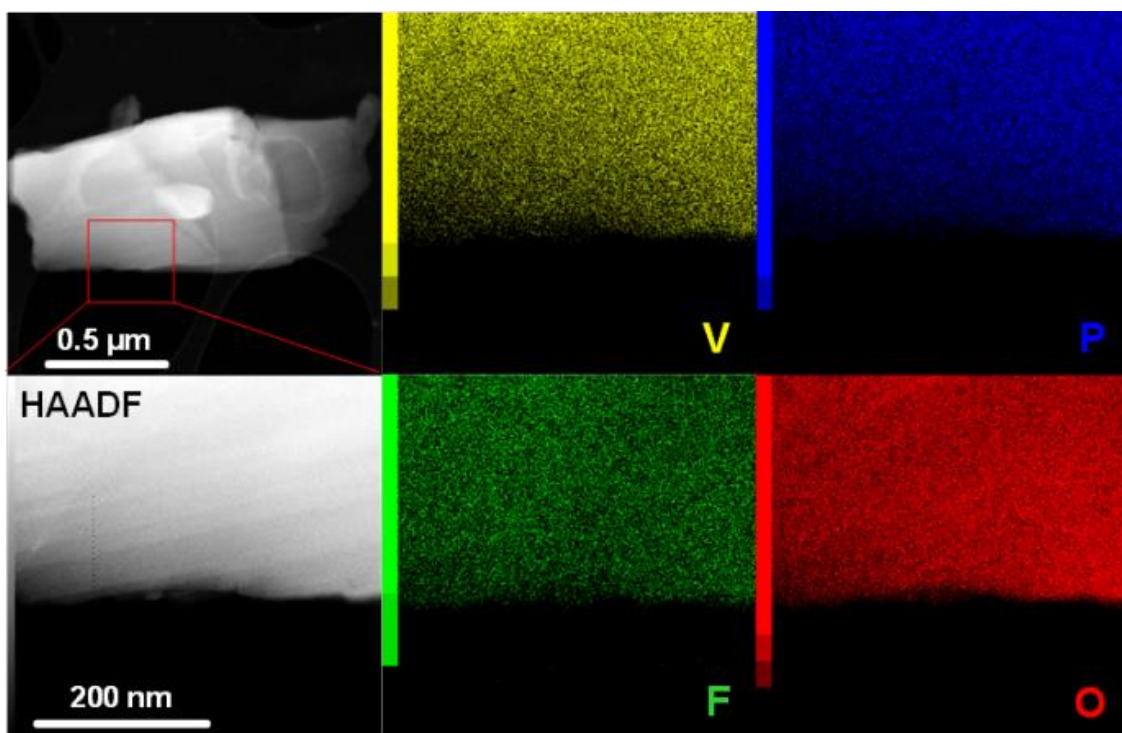


Figure 4-15 STEM-HAADF image and EDS mapping of V, P, F and O elements on a single particle of LVPOF-800 sample [Semsari Parapari, 2020].

To assess the nature of the F incorporation, *i.e.* whether it is homogeneously distributed throughout the particles or mainly incorporated into the particle's near-surface region (core-shell structure), cross-section of a particle was needed. FIB-SEM dual microscope was used to cut out the sample using high-energy ions. Since it was not possible to prepare a sintered pellet for this experiment, LVPOF-800 powder was placed on a carbon tape. To be able to cut any lamella from powder, particles larger than 20 μm in diameter are needed. Therefore, a big particle of $\sim 30 \mu\text{m}$ was chosen and the ion milling was started after deposition of a Pt layer (Figure 4-16a). Upon cutting the first layer of particle, a cross-section with areas of varying color contrast appeared (Figure 4-16b). Since ion-beam microscopy is sensitive to atomic weight of compounds, the difference in contrast corresponded to the presence of various phases. In other words, the seemingly single particle was in fact a composite of particles with different compositions. This was, in addition to XRD phase analysis, an indication of impurities within the material. EDX mapping (Figure 4-16c) showed the distribution of elements (V, O, F and P) in various particles of the agglomerate. Higher contrast of F is indicative of LiF particles, while higher P and O regions correspond to Li_3PO_4 impurity particles. The regions with a homogeneous distribution of all four elements represent the LVPOF-800 particles.

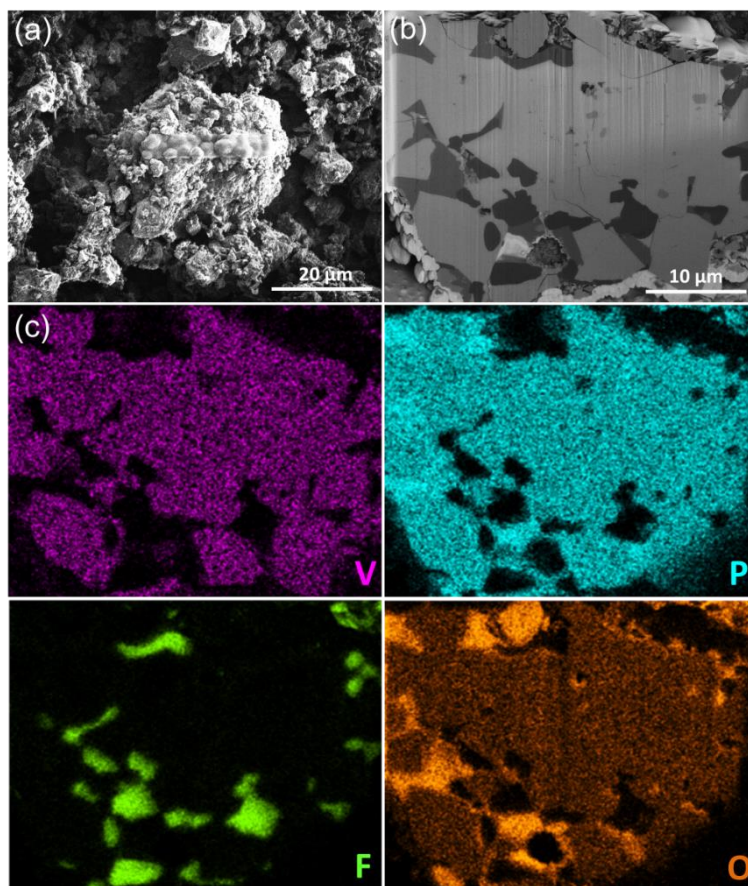


Figure 4-16 FIB-cutting from an agglomerate of LVPOF-800 sample; (a) Pt-deposited particle agglomerate, (b) FIB-cut agglomerate, (c) EDX elemental mapping and (d) elemental values for 3 phases.

With more attempts, we were able to locate a single particle of LVPOF phase with the diameter of $\sim 25 \mu\text{m}$, from which, a lamella was cut out through several steps, as was shown in Figure 2-6 in Chapter 2.

The STEM-EDX mapping performed on this FIB-lamella confirmed a homogeneous incorporation of F into the large particles (Figure 4-17). Additionally, the STEM-EDX spectra were taken from similar thickness areas from a number of various particles, and average elemental composition was determined to be $\text{V}=11.7\pm 2.6 \text{ at. } \%$, $\text{P}=15.5\pm 1.8 \text{ at. } \%$, $\text{O}=61.8\pm 1.5 \text{ at. } \%$, and $\text{F}=9.5\pm 2.5 \text{ at. } \%$. The calculated composition through these values for the LVPOF phase is $\text{Li}_a\text{VPO}_4\text{O}_{0.3}\text{F}_{0.7}$ ($a \geq 1$). However, this notation is not representative of the actual chemical formula due to varying F content. In addition, generally smaller particles were examined during STEM-EDX analysis due to the nature of the TEM sample preparation and measurement. The exclusion of large particles in the analysis may give rise to different values between locally-obtained versus average values. Additionally, comparing the absolute errors (1σ) given for each individual element of

LVPOF-800, precursor ϵ -LVPO and reference LVPF (see Table 4-3), one can see that compositional variations in all of the involved elements are highest for the LVPOF-800 sample.

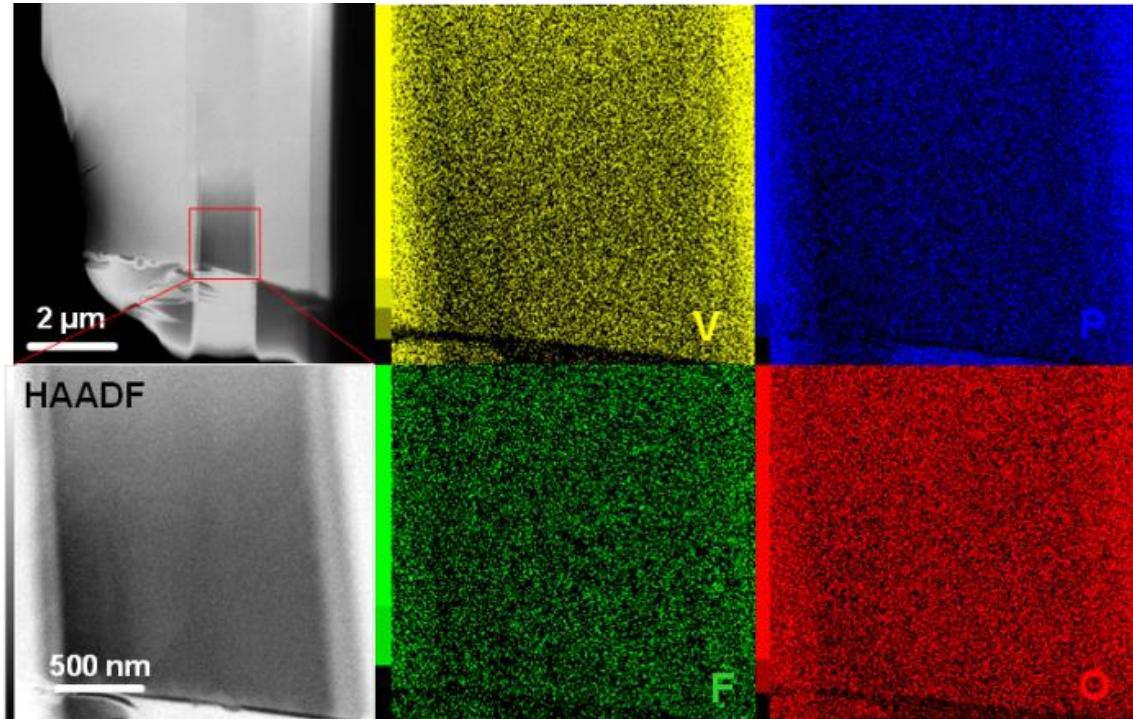


Figure 4-17 STEM-HAADF image and EDS mapping of P, V, F and O elements on the FIB-cut lamella of a particle of LVPOF-800 sample [Semsari Parapari, 2020].

Table 4-3 STEM-EDS chemical composition analysis of LVPOF-800, precursor ϵ -LVPO and reference LVPF samples. The values represent the average atomic percentage and standard deviations of V, P, O and F elements over 20 particles.

	LVPO	LVPOF-800	LVPF
V (at %)	18.4±1.1	11.7±2.6	15.3±1.3
P (at %)	16.8±1.3	15.5±1.8	14.0±1.2
O (at %)	63.6±1.9	61.8±1.5	52.7±1.7
F (at %)	-	9.5±2.5	17.1±0.4

The EELS measurements were used to probe the oxidation state of the vanadium atoms within various samples at the nano-scale through monitoring V-L₂ and V-L₃ edges (Figure 4-18a). The edge onset energy and L₃/L₂ peaks intensity ratio (so-called white-line ratio) are related to the oxidation state of the vanadium atoms. Generally, there are two methods for determination of the elemental valence from the EEL spectrum. In the white-line ratio method, the integral intensity ratio of the V-L₃ and V-L₂ excitation peaks is correlated to

its oxidation state. The other method involves examination of displacement of excitation energy (shift of the edge onset) or so-called chemical shift. The latter method is in general more suitable for V oxide materials due to the overlapping of V-L_{2,3} and O-K edges. However, both methods should be examined for analyzing the oxidation state and local atomic environment [Tan, 2012]. It can be seen in Figure 4-18a that the V edge onset undergoes a shift towards lower energies, as well as a reduction in L₃/L₂ white-line ratio, from precursor ε-LVPO through LVPOF-800 to LVPF. This observation is in agreement with the XANES results (Figure 4-9), in which a shift in edge position toward lower energies was seen in similar order. The physical phenomena probed by the XANES and EELS techniques are of the same nature differing only in the probed area. Consequently, the shifts of the V-L_{2,3} edge position in EEL spectra are as well due to the contributions of both varying F content and V valence changes. With the EELS analysis we could concentrate on the effect of the F amount increase in the LVPO-type structure.

STEM-EELS analysis, due to its nature, is performed with much higher spatial resolution than XANES, allowing the assessment of the electronic properties at the nanometer scale. The edge behavior in spectra taken from four different LVPF reference sample particles was rather stable (Figure 4-18b), whereas there were clear variations in edge onset positions in LVPOF-800 and ε-LVPO particles' spectra (Figure 4-18c, d). The occurrence of these variations in the ε-LVPO precursor could be attributed to the presence of the O vacancies in the lattice. Such a defective O sublattice in the precursor material could promote the F incorporation into the structure. The variations in the LVPOF-800 spectra could be ascribed to the residual O vacancies as well as to the local variations in the incorporated F content among the particles. To evaluate this, the amount of the incorporated F in the LVPOF-800 sample was correlated to the edge onset position via performing simultaneous STEM-EDS and EELS analysis. All of the measurements were carried out with similar conditions in the microscope, such as acceleration voltage, probe current, examined region of interest and data collection time. Figure 4-18c shows the EEL spectra taken from four different LVPOF-800 particles along with EDS defined F content of 7%, 8%, 11% and 12%. Higher F amount resulted in a V L_{2/3} edge onset shift towards lower energies as well as in a decrease in L_{2/3} white-line ratio (lower valence state). This further confirmed the impact of F and its amount in V edge shift, observed also through XANES results. The varying F amounts were indicative of a range of solid solution phase

rather than a single phase at the single particle scale, which in its turn would influence the resulting electrochemical properties.

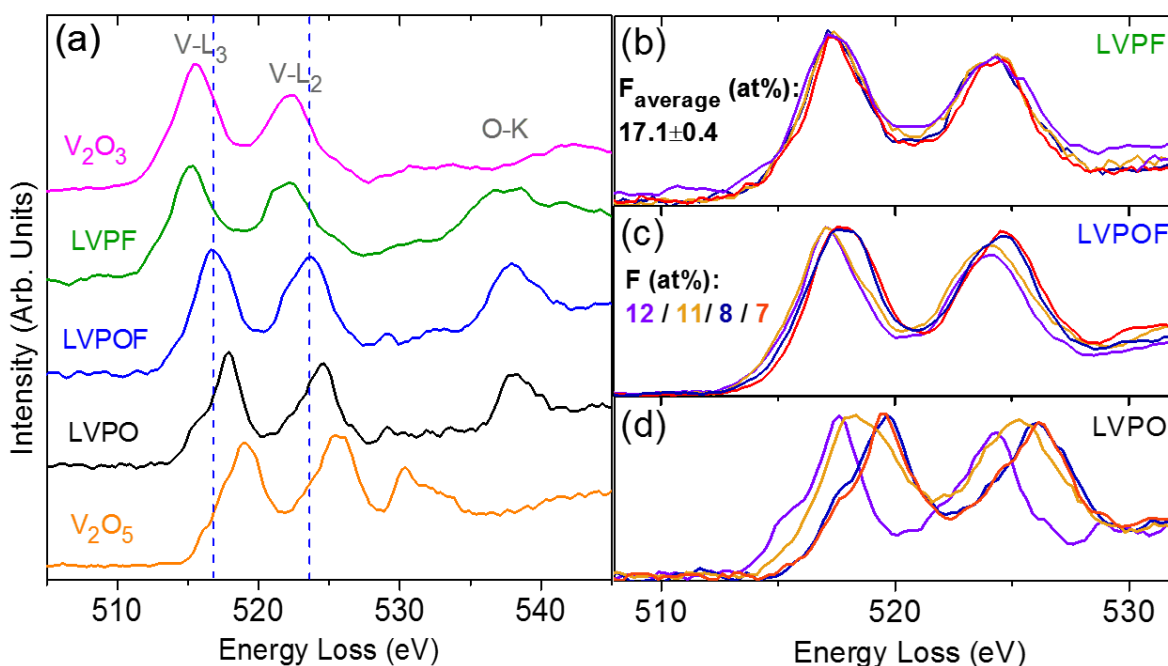


Figure 4-18 EELS spectra obtained at 80kV electron beam energy (a) comparison of LVPO, LVPOF-800, LVPF and reference V_2O_3 and V_2O_5 samples; (b) comparison of four different particles of (b) LVPF, (c) LVPOF-800 and (d) LVPO [Semsari Parapari, 2020].

4.1.2. Electrochemical Analysis

The galvanostatic charge/discharge (Li extraction/insertion) signature of LVPOF samples was investigated and compared to ϵ -LVPO precursor and LVPF by testing them as cathode material in a half-cell battery configuration. Figure 4-19a compares the galvanostatic cycling curves of LVPOF-600, LVPOF-700 and LVPOF-800 samples at high-voltage range (3.0-4.5 V vs. Li/Li⁺) with a current density corresponding roughly to C/50 cycling rate. The electrochemical signature of LVPOF-600 was similar to ϵ -LVPO phase (Figure 4-19b); a biphasic reaction at ~3.95 V involving V⁴⁺/V⁵⁺ redox couple. The same redox couple can be encountered in the LVPOF-700 sample. However, here the ϵ -LVPO phase contributed to only about half of the overall capacity. The other half, therefore, can be attributed to the new LVPOF phase with a higher potential of 4.18V. LVPOF-800 was mainly composed of the LVPOF phase contributing to the electrochemical performance, although an insignificant feature of the ϵ -LVPO phase (short plateau at ~3.95 V) can still be seen. Lithium extraction/insertion proceeded

through a sloping voltage profile which could be an indication of a solid solution-like mechanism. The appearance of such solid solution-like behavior can originate from the presence of the defects detected by EELS analysis. Literature reports that in the case of the defect-free LiFePO_4 material, a biphasic mechanism (well-defined plateau) takes place, whereas for the defective LiFePO_4 , a sloping curve characteristic of solid-solution mechanism occurs [Gibot, 2008][Mestre-Aizpurua, 2010].

The low specific capacity observed for LVPOF-600 and LVPOF-700 (Figure 4-19a) are correlated to the large amount of ϵ -LVPO phase present in both samples, which has been reported to present a poor charge/discharge capacity [Bianchini, 2014][Ateba Mba, 2013]. Figure 4-19b shows the galvanostatic cycling curves of LVPO, LVPOF-800 and LVPF obtained at high-voltage range. The extraction/insertion of Li in LVPOF-800 took place at around 4.12 V vs. Li/Li^+ (for mixed $\text{V}^{3+}/\text{V}^{4+}$ and $\text{V}^{4+}/\text{V}^{5+}$ redox couples), which differed from ϵ -LVPO (3.95 V for $\text{V}^{4+}/\text{V}^{5+}$ redox couple) and LVPF (4.26 V for $\text{V}^{3+}/\text{V}^{4+}$ redox couple). An increment of the working potential in LVPOF-800 with respect to the precursor ϵ -LVPO was expected due to the inductive effect of the incorporated F, which would increase the ionic character of V-O/F with respect to V-O bonds in ϵ -LVPO. In addition, LVPOF showed higher charge/discharge capacity compared to LVPO. We believe that F incorporation can improve the low kinetics of Li diffusion in ϵ -LVPO structure and therefore allow for a higher Li exchange during electrochemical cycling. The polarization of the LVPOF-600 followed the pattern observed in the ϵ -LVPO sample (Figure 4-19b). In the LVPOF-700, the polarization changes were due to the presence of two phases, ϵ -LVPO and LVPOF. Polarization of LVPOF phase in LVPOF-700 sample is much lower than ϵ -LVPO. This enhancement can be partly related to the mixed valence state, $\text{V}^{3+}/\text{V}^{4+}$, which was a result of fluorine substitution in V-O ligands of $[\text{VO}_6]$ octahedral chains. The higher charge transfer and enhanced hopping process between V^{3+} and V^{4+} cations in LVPOF could lead to higher conductivity and thus, lower polarization [Kim, 2017][Chung, 2002]. However, the polarization of LVPOF phase here differed from that observed in LVPOF-800 sample, where LVPOF was the main contributing phase. The reason for that can be the particle size difference of between the two samples.

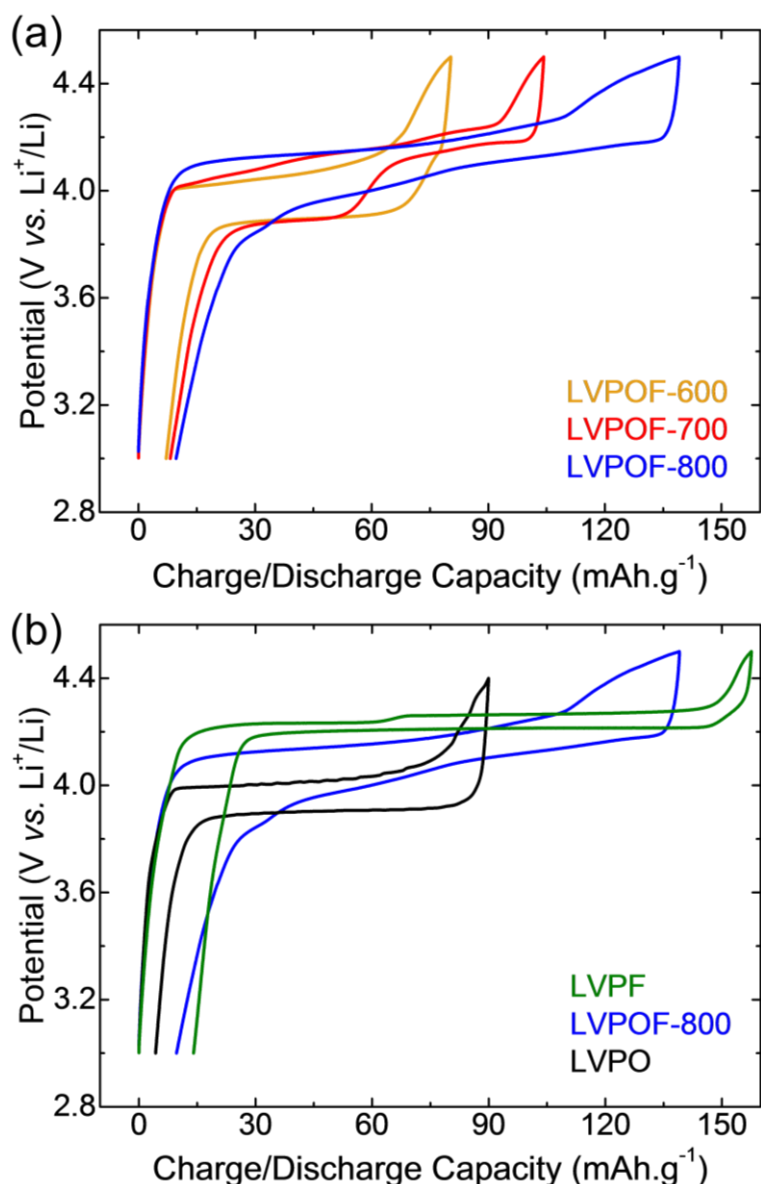


Figure 4-19 Galvanostatic cycling curves obtained vs. Li at a C/50 rate for (a) LVPOF-600, LVPOF-700 and LVPOF-800 samples; and (b) ϵ -LVPO, LVPOF-800 and LVPF, in the high-voltage range (*i.e.* between 3.0 and 4.5 V vs. Li/Li⁺) [Semsari Parapari, 2020].

The galvanostatic cycling curves of LVPOF-600, LVPOF-700 and LVPOF-800 samples at low-voltage range (*i.e.* between 1.5 and 3 V vs. Li/Li⁺) are shown in Figure 4-20. LVPOF-600 showed similar electrochemical signature as ϵ -LVPO [Ateba Mba, 2012], also for the insertion reaction of Li into the structure. This reaction proceeded through a series of phase transitions at 2.47, 2.21, and 2.03 V vs. Li/Li⁺ involving V^{IV}/V^{III} redox couple, which would lead to formation of Li₂VPO₄O. This behavior was also observed for LVPOF-700, however, an additional plateau appeared at ~1.78 V. The specific capacity of LVPOF-700 for the insertion of Li is almost half of the one for LVPOF-600.

The reduction of specific capacity is linked to the presence of LVPOF phase, since LVPOF-800 showed even lower Li insertion capacity during a sloping voltage cycling curve. This curve resembles the cycling signature of LVPO, even though it lacks the biphasic steps and this can be another indication of LVPO-type structure. The low activity of LVPOF phase, which led to low specific capacity, can be attributed to the extra Li in $\text{Li}_a\text{VPO}_4\text{O}_b\text{F}_{1-b}$ compound. It is presumed that the extra Li ions occupy the available Li sites and only limited amount of additional Li ions can be inserted.

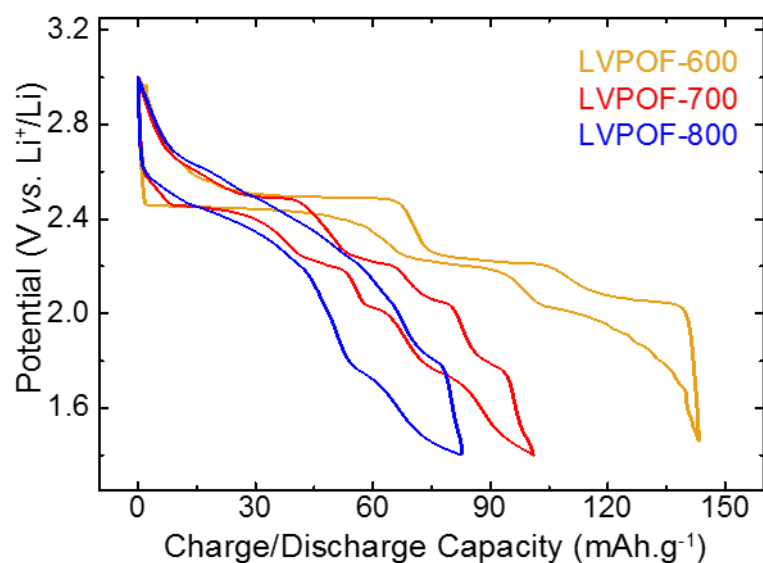


Figure 4-20 Galvanostatic cycling curves obtained vs. Li at a C/50 rate for LVPOF-600, LVPOF-700 and LVPOF-800 samples, in the low-voltage range (*i.e.* between 1.5 and 3.0 V vs. Li/Li⁺) [Semsari Parapari, 2020].

4.2. Summary and Discussion

In this chapter, the synthesis, characterization and electrochemical properties of β -VPO and ϵ -LVPO phases fluorinated by LiF was discussed. A sealed stainless steel reactor filled with Ar was utilized in order to perform the synthesis at high temperatures.

The incorporation of LiF in β -VPO at temperatures above 500 °C resulted in formation of a triclinic-structured vanadyl phosphate phase. Increasing the temperature to 600 °C and then 700 °C increased the LiF consumption in the reaction, leading to shifts in XRD peaks of the formed phase. The peak shifts were attributed to higher amount of fluorination, which at 700 °C, resulted in formation of an LVPF-type phase, with similar peak positions as LVPF material. This was confirmed through NMR results, since the ^6Li and ^{31}P shifts of the two phases appeared in similar positions on the spectra. The

electrochemical signature of the fluorinated VPOF material was composed of various steps, which could correspond either to the presence of similar phases in the product or several steps in the electrochemical reaction itself. The reproducibility of these reactions was challenging. This was attributed to the instability of the β -VPO phase during the high-temperature reaction in the reactor, which apparently leads to decomposition to phases with lower vanadium oxidation state, such as VPO_4 . It is therefore assumed that the appearance of an LVPF-type phase could be due to the reaction of LiF with the decomposition products. This is suggested based on a comparison to the synthesis process of LVPF (see Chapter 3), in which, LVPF is produced through the reaction of VPO_4 and LiF, through a similar process. Therefore, for any further studies, other approaches must be applied, in which, the β -VPO phase would not undergo intrinsic changes during the reaction.

The fluorination of ϵ -LVPO by incorporation of LiF took place at temperatures above 600 °C. At 700 °C, the synthesized material was a composite of precursor ϵ -LVPO and new LVPOF phase, while at 800 °C, LVPOF was the main phase. This showed the temperature dependency of the phase formation in this synthesis. The LVPOF phase preserved the framework structure of ϵ -LVPO and F atoms substituted the O atoms in the V-X ligands of octahedral chains in the structure. Structural refinement showed that F atoms substituted in average about 20% of O atoms. Spatially-resolved STEM-EDS analysis, on the other hand, gave quantities in the order of 70% average atomic substitution of F for O in measurements on single LVPOF particles. However, the F content varied among different particles ($F=9.5\pm 2.5$ at. %) and this number (70%) cannot be representative of an actual amount. In addition, generally smaller particles were examined during STEM-EDX analysis due to the nature of the TEM sample preparation and measurement. The exclusion of large particles in the analysis may give rise to different values between locally-obtained versus average values. XANES analysis showed that vanadium in LVPOF had a mixed $3+/4+$ valence state. However, the exact value could not be assessed due to the effect of F (ionicity of V-F bond) on the edge absorption of spectrum. This was investigated by comparing several standard V-containing materials, with and without F in their composition. The distortion of VO_6 octahedra in ϵ -LVPO was reduced in LVPOF. The presence of F resulting in V reduction caused a higher symmetry in octahedra. In general, lower V valence state increases the symmetry of the V polyhedra in polyanion materials. The LiF-incorporated phase showed

distinct electrochemical behavior than ϵ -LVPO, with higher operating potential and higher charge capacity. The higher ionicity of V-F bonds in LVPOF compared to V-O and highly covalent V=O bonds in ϵ -LVPO affected the lithium extraction/insertion reaction during electrochemical cycling. Another important observation in this part of the study was the variations confronted at micro- and nano-scale measurements. The systematic characterization of the synthesis products allowed insights on general material properties and also on local changes within the material. The results showed the importance of multi-level characterization, since the average properties through larger-size samples could not always be representative for the local variations.

CHAPTER 5: FLUORINATION OF VANADIUM OXY-PHOSPHATES BY PTFE

As a second source of fluorine in this work, PTFE (also known as Teflon trademark) powder was used. The intermediate phosphate materials (β -VPO and ε -LVPO) were mixed with stoichiometric amounts of PTFE dry powder and ground together using a mortar and pestle. Pellets were pressed with ~ 200 MPa pressure for 1 min. The weight of each pellet was kept below 100 mg in order to avoid the possible damage from formation of CO_2 in a closed system. The pellets were put inside of the stainless steel reactor and the reactors were sealed inside of the glovebox with Ar atmosphere.

The pellets were heat treated at various temperatures to follow the reactions ex-situ.

5.1. Fluorination of VPO_4O by PTFE

A reaction according to Equation 5-1 was expected to take place at high-temperature heating of VPO_4O and PTFE mixture:



Figure 5-1 shows the XRD results after heat-treatment of the β -VPO and PTFE mixture at 500 °C, 600 °C and 700 °C (named VPO/T) in comparison to β -VPO pattern. At 500 °C (VPO/T-500), peaks of β -VPO and PTFE are present. PTFE decomposes at ~ 500 °C in the inert atmosphere. Therefore, no reaction started in this temperature between the reactants. At 600 °C (VPO/T-600), peaks of precursors disappeared and peaks of a new phase appeared on the pattern. Simple phase matching showed that the new phase is $(\text{VO})_2\text{P}_2\text{O}_7$. This phase was also the product of synthesis at 700 °C (VPO/T-700). EDX analysis on the particles of these samples showed no presence of fluorine in the elemental composition.

The complete phase change during this synthesis was attributed to the instability of β -VPO in the reactor at high temperatures, as was shown previously in Chapter 4. Thus, this synthesis was ceased at this point and the experiments continued with ϵ -LVPO as the precursor, which is the subject of following section.

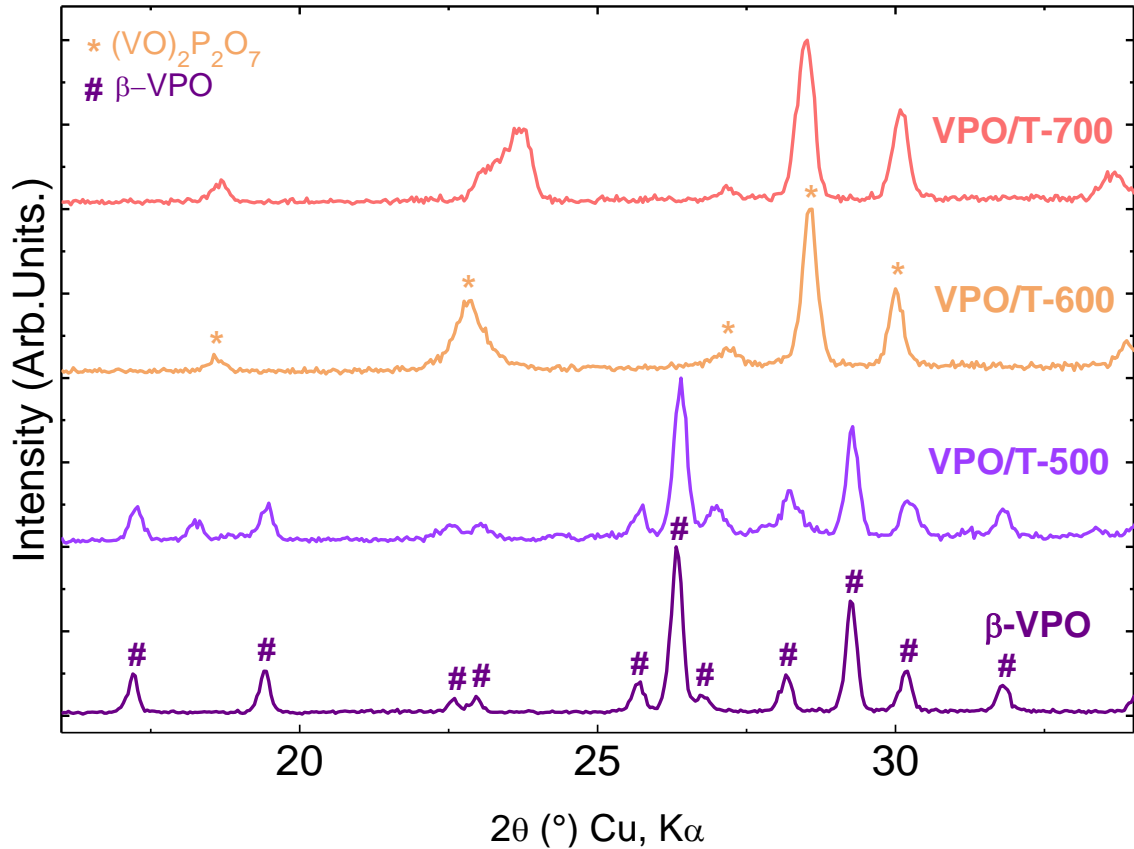


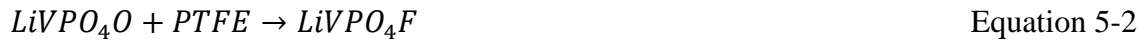
Figure 5-1 XRD patterns of VPO+PTFE mixture (VPO/T) at RT and heat-treated at 500, 600, and 700 °C. $(VO)_2P_2O_7$ and β -VPO peaks are marked by asterisk and hash signs on the figure, respectively.

5.2. Fluorination of ϵ -LiVPO₄O by PTFE

Two sets of experiments were performed. In the first experiment, a stoichiometric amount of ϵ -LVPO and PTFE powders were mixed and used in the synthesis process. In the second experiment, PTFE was used in excess amounts in order to provide a stronger fluorinating atmosphere. The results obtained for both of the experiments are described below.

5.2.1. Stoichiometric Mix: Synthesis and Characterization

The stoichiometric mixture of ϵ -LVPO and PTFE was mixed according to Equation 5-2 and heated at various temperatures.



Considering the decomposition temperature of PTFE (~ 500 °C), 600 °C was chosen as the lowest heat treatment temperature. Figure 5-2 shows the XRD results obtained for the synthesized materials at 600-800 °C (named LVPO/T) in comparison to pure ϵ -LVPO and LVPF. The black and green dashed lines respectively show the location of LVPO and LVPF peaks. Some of ϵ -LVPO peaks start to shift by heating up the mixture. The change in peak positions starts already at 600 °C (LVPO/T-600). The peaks at 27° and 30° shift towards lower angles. Such 2θ shifts are more pronounced at 700 °C (LVPO/T-700). At 800 °C (LVPO/T-800), the material completely transformed to another vanadium phosphate phase, $Li_3V_2(PO_4)_3$. This phase is known to form during the synthesis of LVPF using the autoclave, either as an impurity or as the main phase. Controlling the synthesis conditions such as heating rate, cooling rate, the sealed atmosphere and the amount of surrounding carbon (especially in CTR reaction) is critically important in this type of synthesis [Barker, 2003][Ateba Mba, 2012]. Therefore, we can presume that the same phenomena happened during this synthesis, meaning that the formation of $Li_3V_2(PO_4)_3$ is a side-reaction during LVPF formation through fluorination of LVPO.

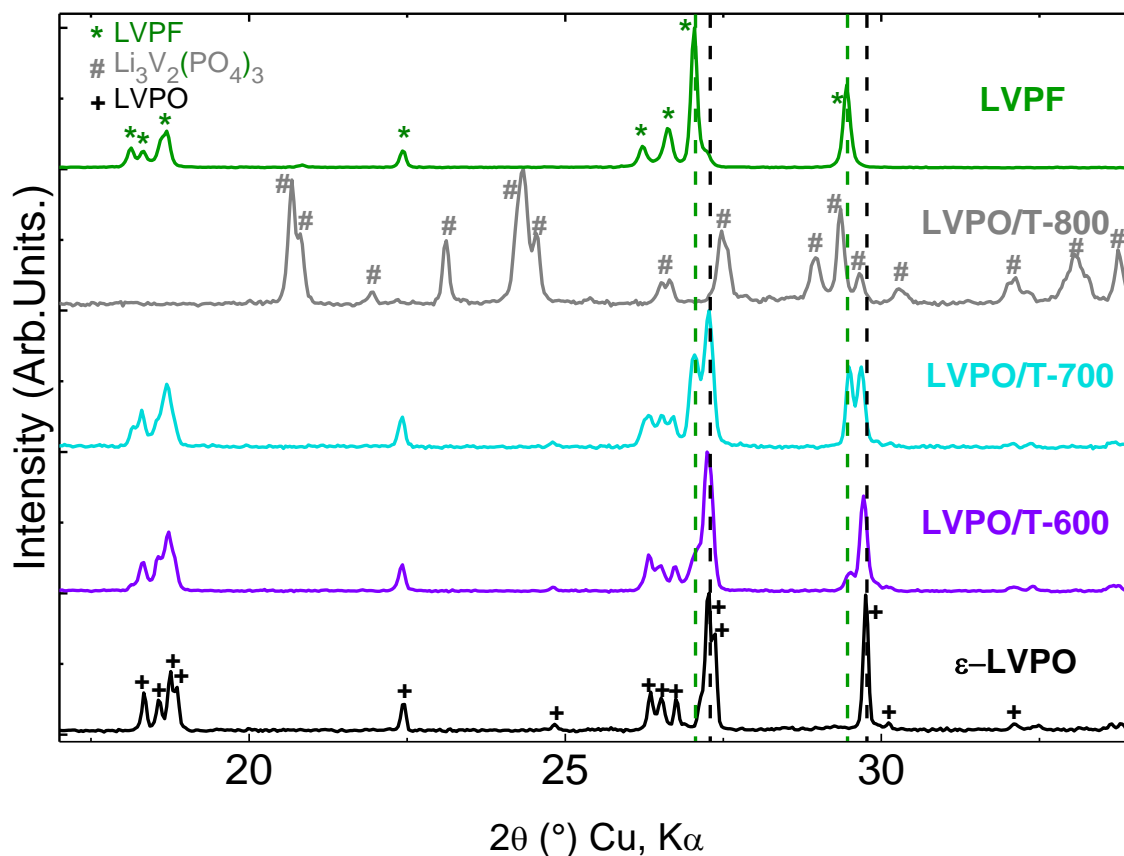


Figure 5-2 XRD patterns of ϵ -LVPO+PTFE mixture (LVPO/T) at RT and heat-treated at 600, 700 and 800 $^\circ$ C. The black and green dashed lines respectively show the location of LVPO and LVPF main peaks. The LVPF, Li₃V₂(PO₄)₃ and LVPO phases are marked by asterisk, hash and plus signs, respectively.

In order to assess the possibility of a more efficient fluorination at longer reaction durations, a synthesis was performed, in which, the LVPO+PTFE mixture was heated at 700 $^\circ$ C for 5h. The XRD pattern of the product is compared to the one obtained at 0.5h heating duration in Figure 5-3. Comparing the features of the patterns such as peak positions showed that the fluorination efficiency did not increase by longer heating times.

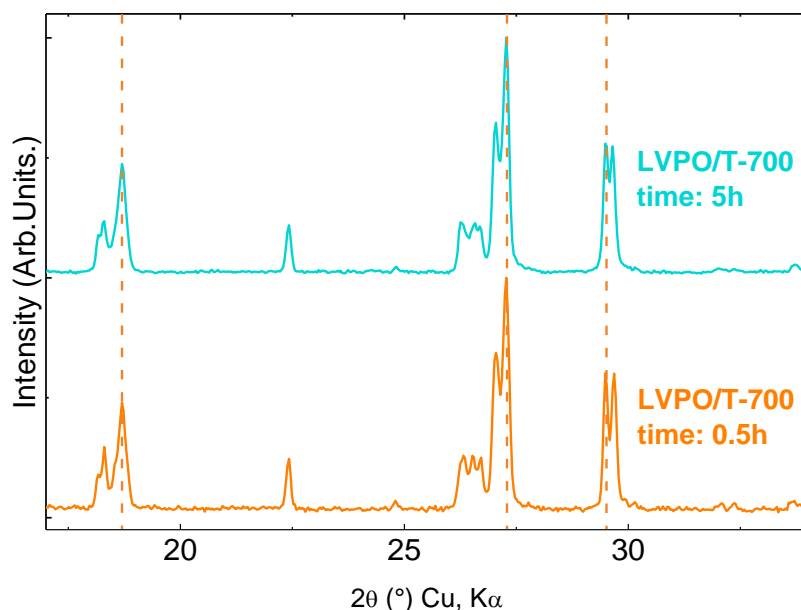


Figure 5-3 XRD patterns of ϵ -LVPO+PTFE mixture (LVPO/T) heated at 700 °C for 0.5 h and 5 h. The orange dashed lines show the location of LVPF peaks in LVPO/T-700.

Microstructure of sample LVPO/T-700 is shown in the SEM micrographs in Figure 5-4. The sample is composed of $\sim 10 \mu\text{m}$ size agglomerates within which, micron-size particles exist. In general, the particles have a similar look to the precursor LVPO particles (Figure 3-12). An additional layer seems to be covering the particles, which gave an amorphous appearance to them.

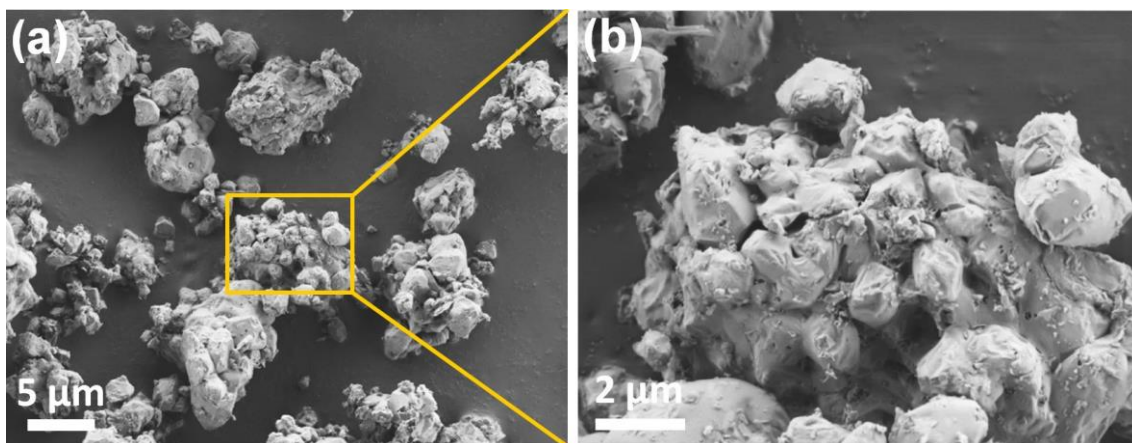


Figure 5-4 SEM micrographs of sample LVPO/T-700, (a) at low magnification, showing the agglomerates and (b) at high magnification showing the single particles morphology.

The presence of such layer is more visible in the STEM image in Figure 5-5a. In this image, a transparent layer is lying around a LVPO/T-700 particle of $\sim 200 \text{ nm}$ size. Figure 5-5b shows a high-magnification image of the layer around the particles. It has an

amorphous structure, which can also be seen from the FFT image in the inset. EDX analysis on this layer showed that this carbonaceous material does not contain F. Therefore, it is the leftover from the decomposition of PTFE powder.

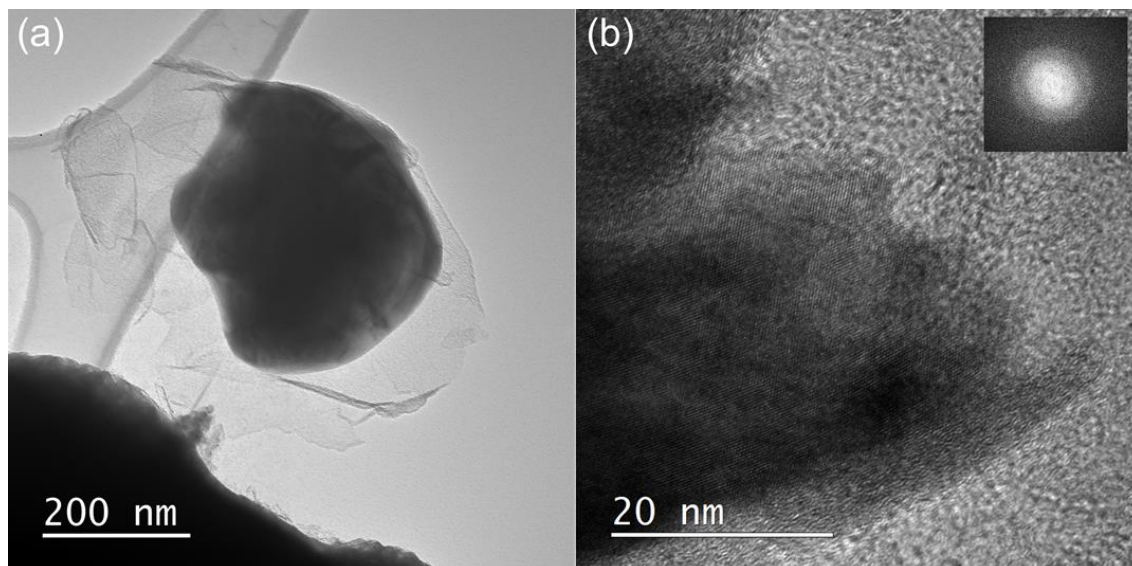


Figure 5-5 STEM image of a particle of sample LVPO/T-700, (a) particle covered with a carbonaceous layer and (b) high-resolution image of the particle, showing the amorphous nature of the carbon layer. The inset shows the FFT of the amorphous layer.

5.2.2. Stoichiometric Mix: Electrochemical Behavior

The shift in XRD peaks indicated the occurrence of a structural change, possibly due to incorporation of fluorine. Galvanostatic measurements were performed to characterize the electrochemical signature of the fluorinated material. Figure 5-6 compares the galvanostatic cycling of LVPO, LVPF and the fluorinated sample at 700 °C (LVPO/T-700). More than half of the capacity of LVPO/T-700 sample comes from an LVPF-type phase with operating potential of ~4.26 V. This indicates the successful fluorination using PTFE powder. However, some of the material is not transformed and the operating potential of the second part of capacity is similar to an LVPO-type material with operating potential close to 4 V. The presence of two distinct phases in the sample was already observed in the XRD pattern (Figure 5-2).

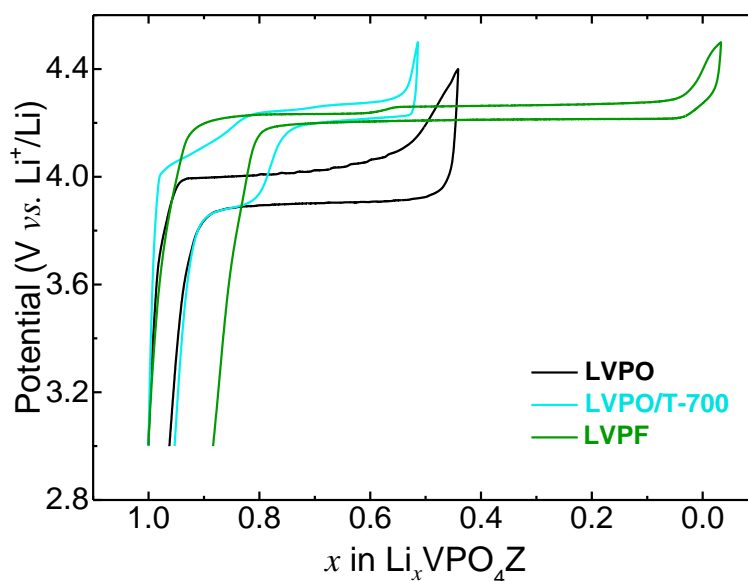


Figure 5-6 Galvanostatic cycling curves obtained for LVPO/T-700 in comparison to LVPO and LVPF at a C/50 rate in the high-voltage range (*i.e.* between 3.0 and 4.5 V vs. Li/Li⁺).

5.2.3. Excess of PTFE: Synthesis and Characterization

Considering the inefficiency of longer heating duration in the fluorination process (Figure 5-3), another approach was employed in the process. In this, higher amount of PTFE (2 moles) was used in the synthesis. The excess amount of fluorine in the reactor could provide a stronger F-rich atmosphere, which would in turn help with the fluorination process. The precursors, one mole of ϵ -LVPO and 2 moles of PTFE were mixed according to Equation 5-3 and the mixture was heated up at various temperatures.



The XRD patterns of the synthesized materials (named LVPO/2T) are shown in Figure 5-7. The black and green dashed lines respectively show the location of LVPO and LVPF peaks. The heat-treatments were conducted at 600-900 °C. At 600 °C (LVPO/2T-600), the peak related to PTFE (18°) is still present and the peaks of ϵ -LVPO do not show a drastic shift. At 700 °C (LVPO/2T-700), the peak of PTFE started to decrease in intensity and alongside with that, the peak at ~30 shifted to lower angles. Increasing the heating temperature to 800 °C (LVPO/2T-800) and then 900 °C (LVPO/2T-900) resulted in complete consumption of PTFE and formation of an LVPF-type phase. In addition, in LVPO/2T-800 and to smaller extent in LVPO/2T-900, peaks of a second phase, $\text{Li}_3\text{V}_2(\text{PO}_4)_3$ (marked by asterisks) are also present. Formation of this phase could be due to the leakage in the synthesis reactor. In the case that the reactor is not tightened well,

some air can be exchanged with Ar atmosphere. This, most probably happened during cooling process with decrease of inner atmosphere pressure, and result in formation of such impurity phase.

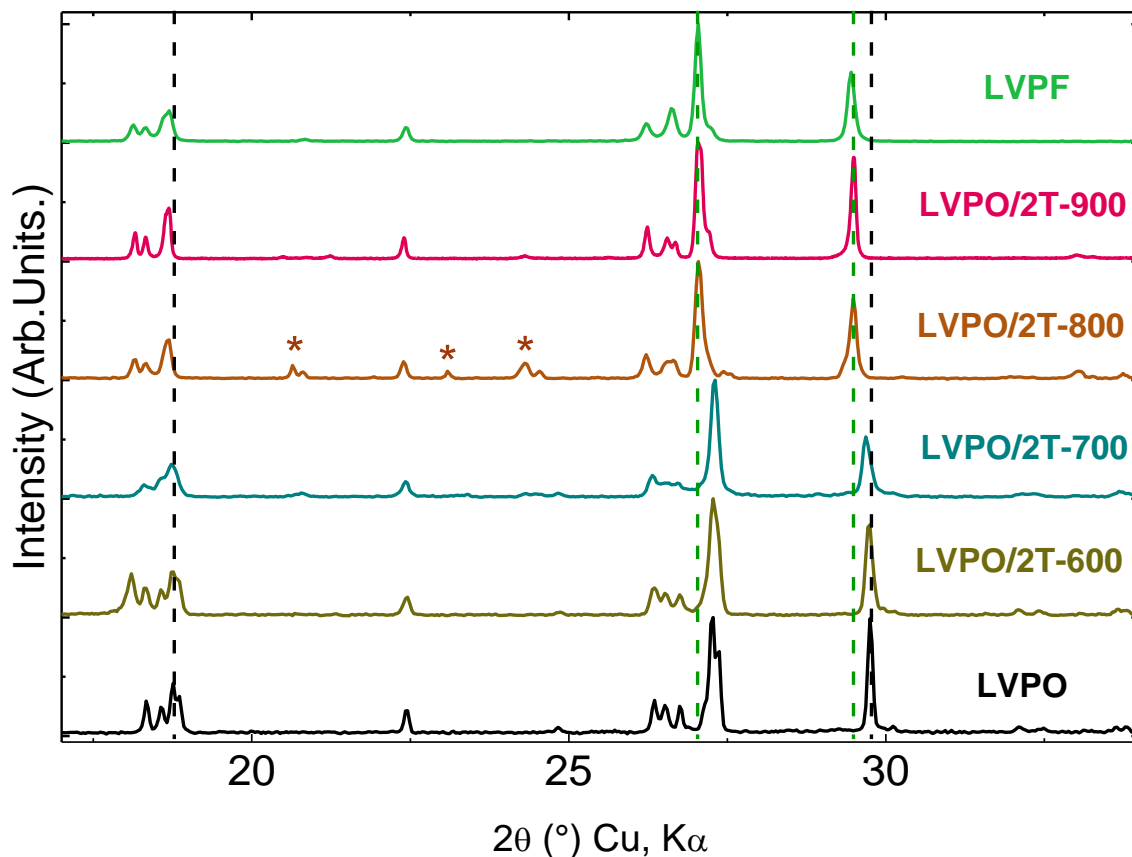


Figure 5-7 XRD patterns of ϵ -LVPO+2PTFE mixture at RT and heat-treated at 600, 700, 800 and 900 °C in comparison to ϵ -LVPO and LVPF. The black and green dashed lines respectively show the location of LVPO and LVPF peaks. The asterisks show the $\text{Li}_3\text{V}_2(\text{PO}_4)_3$ impurity peaks.

The SEM micrographs of sample LVPO/2T-900 are shown in Figure 5-8 at low (a) and high (b) magnification. We can see that the particles have grown in size, compared to LVPO/T-700 (Figure 5-4), due to the higher synthesis temperature of 900 °C. The particles do not have the crystalline shape of precursor LVPO and tend to have undefined shape. Higher amount of the leftover carbonaceous layer is seen compared to the sample synthesized from the stoichiometric mix (LVPO/T-700).

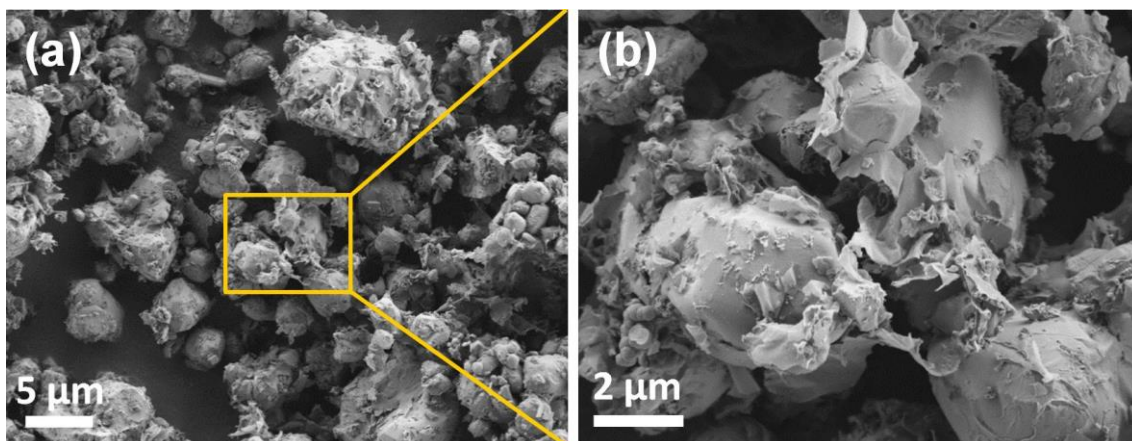


Figure 5-8 SEM micrographs of sample LVPO/2T-900, (a) at low magnification, showing the agglomerates and (b) at high magnification showing the single particles morphology.

The STEM-EDS mapping on a single particle of LVPO/2T-900 sample shows that V, P, F and O elements are distributed homogeneously. This confirmed the successful fluorination of LVPO particles throughout the particle. The contrast changes on EDS maps are due to the variation in thickness in the particle.

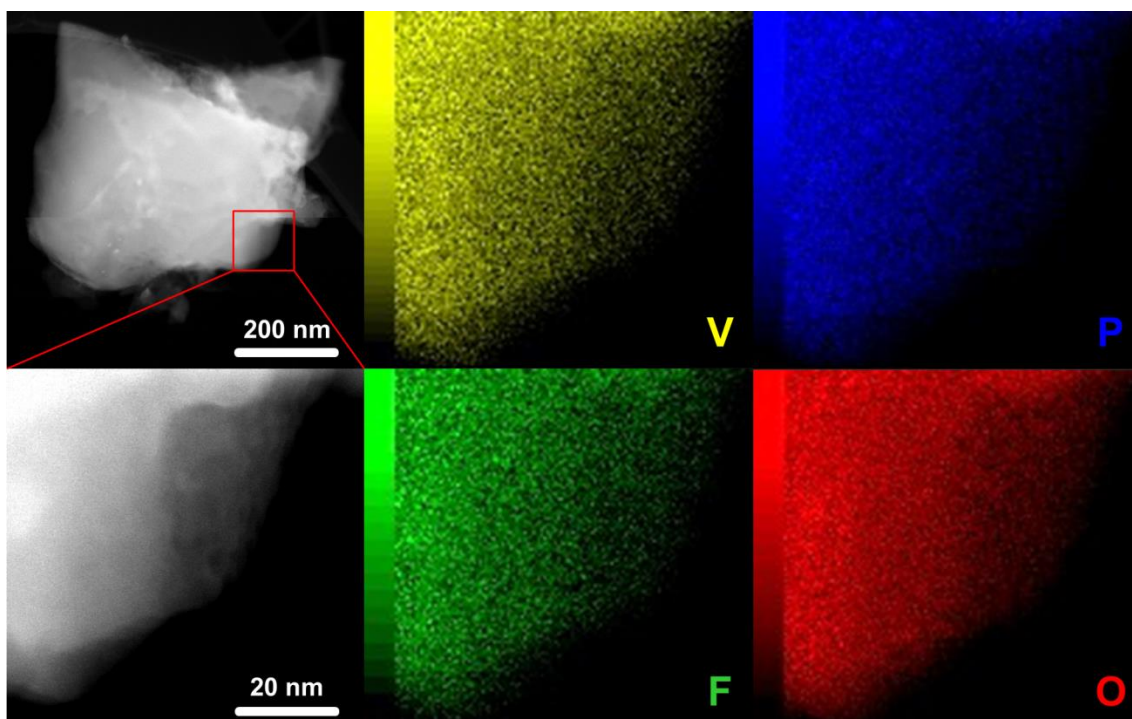


Figure 5-9 STEM-HAADF image and EDS mapping of V, P, F and O elements on a single particle of LVPO/2T-900 sample.

In Figure 5-10, the high resolution XRD patterns of LVPO, LVPO/2T-900 and LVPF are compared. Sample LVPO/2T-900 has evolved from an LVPO phase towards an LVPF-

type phase. However, there are distinctions between LVPO and LVPO/2T-900 samples, either in peak intensity *e.g.* peak at 29.5° or peak splitting, *e.g.* peak at 26.7° . Therefore, a more thorough analysis of the diffraction pattern was performed by Rietveld analysis in order to study the structure of this material.

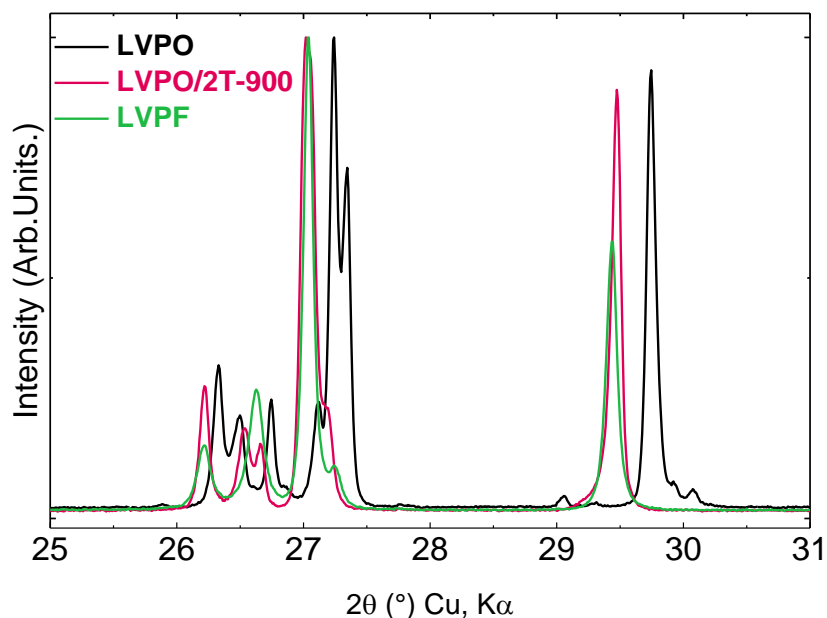


Figure 5-10 Comparison of main peaks of XRD patterns of LVPO, LVPO/2T-900 and LVPF.

5.2.4. Excess of PTFE: Crystal Structure

The structural parameters were refined for the LVPO/2T-900 sample by LeBail method starting from the structural model of LVPF (ICSD No. 184601). The refined pattern is shown in Figure 5-11. The refinements showed that this phase has the Tavorite-type structure of LVPF and in fact, the phase is (almost) identical to LVPF. In addition, small amount of $\text{Li}_3\text{V}_2(\text{PO}_4)_3$ impurity was observed. The refined lattice parameters of the triclinic lattice with $P\bar{1}$ space group (N^o2) are shown in Table 5-1.

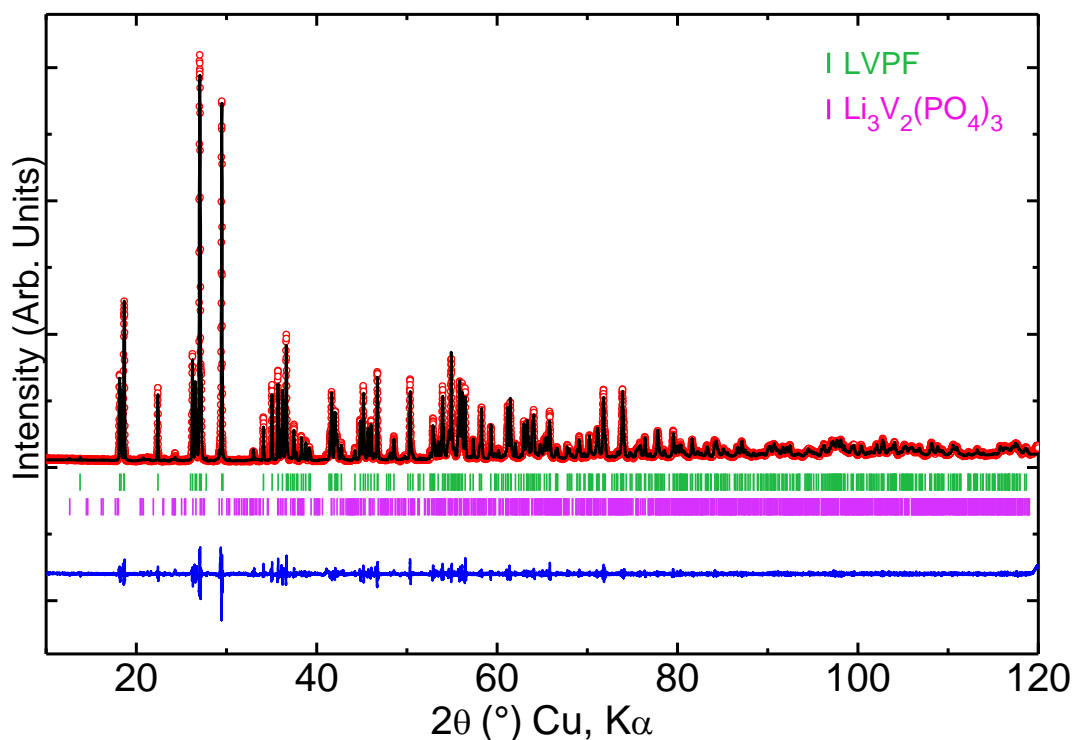


Figure 5-11 Rietveld refinement of LVPO/2T-900 sample based on X-ray powder diffraction pattern. The observed, calculated and difference curves are presented as red dots, black line and blue line, respectively. The theoretical Bragg positions of LVPF (green) and impurity $\text{Li}_3\text{V}_2(\text{PO}_4)_3$ (purple) are shown.

Table 5-1 Structural parameters of LVPO/2T-900 calculated by LeBail refinement matching method.

a (Å)	b (Å)	c (Å)	α (°)	β (°)	γ (°)	V (Å ³)
5.1735(0)	5.3121(7)	7.2593(9)	107.5436(7)	107.9641(8)	98.4270(7)	174.529

The crystal structure of the fluorinated phase, similar to LVPF, is built up of interconnected VO_4F_2 octahedra which share common fluorine atoms to form infinite ...V-F-V... chains (Figure 5-12a). These chains are connected to each other via isolated PO_4 tetrahedra. A 3D framework is generated by these corner-sharing polyhedra with tunnels that run along [100], [010] and [101]. Vanadium lies in two octahedral sites (V(1) and V(2) in Figure 5-11) with a V-O distances in the range of 1.96-1.99 Å. The V-F distances on the octahedral chains are 1.98 Å (Figure 5-12b), which differs them from the short and long bonds in precursor ϵ -LVPO. The reduction of V valence state from +4 to +3 as a result of introducing F in the Tavorite structure of ϵ -LVPO, plays a vital role in lowering the distortion in octahedra and forming more symmetrical ligands.

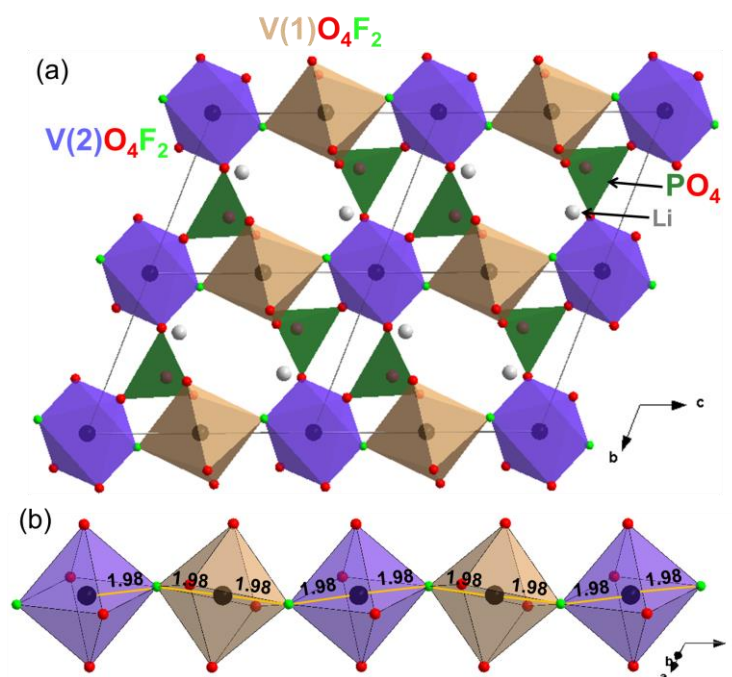


Figure 5-12 Crystal structure of LVPO/2T-900, (a) interconnection of VO_4F_2 octahedra and PO_4 tetrahedra, (b) VO_4F_2 octahedral chain.

5.2.5. Excess of PTFE: Electrochemical Behavior

The electrochemical behavior of the synthesized samples was studied using galvanostatic cycling at C/50 rate. Figure 5-13a and b show a comparison between ϵ -LVPO, LVPF, and the fluorinated samples LVPO/2T-800 and LVPO/2T-900 for the cycling at high voltage range (3-4.5 V) and low voltage range (1.5-3 V), respectively. LVPO/2T-800 and LVPO/2T-900 both show feature of an LVPF-type operating potential at ~ 4.25 V (Figure 5-13a). They both show an LVPF-type electrochemical signature, where a step was appeared in the oxidation half-cycle due to formation of $\text{Li}_{0.67}\text{VPO}_4\text{F}$ intermediate phase. They also both show a comparable polarization to LVPF sample at this potential. The polarization of LVPO/2T-900 is slightly larger than LVPO/2T-800, which could be due to a particle size growth at higher temperature. Some of the capacity of LVPO/2T-800 also comes from the $\text{Li}_3\text{V}_2(\text{PO}_4)_3$ phase. The operating potential plateaus of this phase at 3.6V, 3.68 V and 4.05 V are visible in the cycling graph. These features are almost invisible for sample LVPO/2T-900 due to the very small quantity of this impurity in this sample. No features related to ϵ -LVPO phase (operating potential 3.95 V) are present in samples LVPO/2T-800 and LVPO/2T-900. This can also be seen in the low voltage range cycling curves (Figure 5-13b), where samples LVPO/2T-800 and LVPO/2T-900 show mainly LVPF-type behavior and there is no feature of ϵ -LVPO plateaus on the curves.

The well-defined plateau of LVPF is changed slightly towards a sloping voltage for sample LVPO/2T-900, that is even more pronounced for sample LVPO/2T-800. In addition, the operating potential of LVPO/2T-900 is slightly higher than LVPF being 1.82 V and 1.78 V, respectively. It is difficult to assign a defined voltage for LVPO/2T-800, due to the sloping voltage behavior. These observations confirm the XRD results which showed a modification from ϵ -LVPO phase towards an LVPF-type phase.

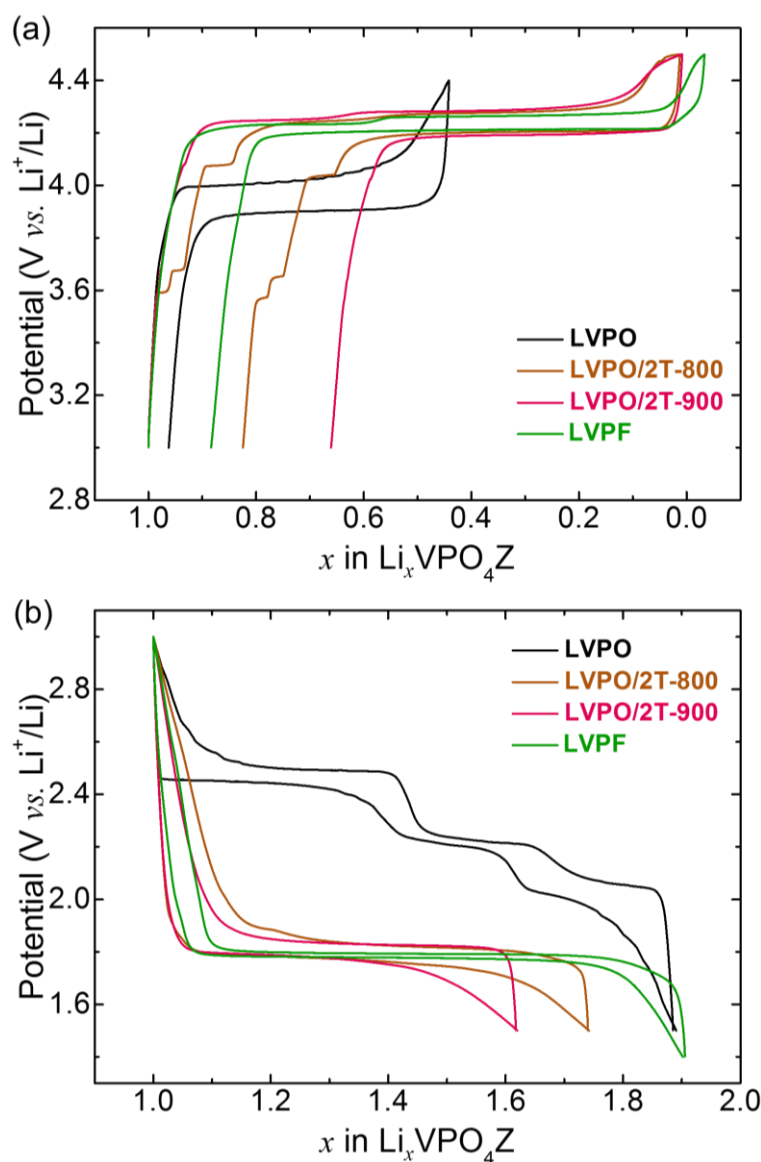


Figure 5-13 Galvanostatic cycling curve of LVPO, LVPO/2T-800, LVPO/2T-900 and LVPF at second cycle at (a) high-voltage range (3.0-4.5 V vs. Li/Li⁺) and (b) low voltage range (1.5-3.0 V vs. Li/Li⁺) with a current density corresponding to C/50 cycling rate.

5.3. Summary and Discussion

In this chapter, fluorination of β -VPO and ε -LVPO materials by PTFE was discussed. PTFE with the $(C_2F_4)_n$ chemical formula, is a fluoropolymer of tetrafluoroethylene. It is composed completely from carbon and fluorine. Thus, when decomposed at high temperatures, could provide a highly fluorinating atmosphere. It was predicted that decomposed PTFE could stimulate a complete fluorination, where F atoms would substitute the O atoms in the V-X (X=O or F) bonds of vanadyl phosphate materials and form the fluorinated counterparts (VPO₄F and LiVPO₄F). In this work, PTFE was used for the first time, to the best of our knowledge, as the sole source of fluorination.

Firstly, the mixture of β -VPO phase and PTFE was heated at high temperatures. The β -VPO phase showed a complete transformation to (VO)₂P₂O₇ pyrophosphate phase and no fluorination occurred. This was again attributed to the instability of the β -VPO phase, as discussed in Chapter 4. Therefore, this method could not be applied for the formation of VPO₄F phase with the used conditions.

Secondly, ε -LVPO was fluorinated by mixing with stoichiometric amounts of PTFE powder and heating at high-temperatures. The fluorination took place at temperatures as high as 700 °C, where around half of the ε -LVPO phase was transformed to LVPF. Longer heating duration did not result in higher fluorination amount. Thus, another approach was employed, in which excess amount of PTFE was used in the synthesis process. The stronger fluorinating atmosphere in the synthesis medium resulted in more efficient fluorination and at 900 °C, ε -LVPO transformed to “LVPF” with only a slight formation of impurities. The structural analysis showed the formation of LVPF-type phase. The carbon reminiscent of the PTFE decomposition provides a reducing atmosphere inside the synthesis reactor. This, allows an easier path for transformation of V⁴⁺-containing ε -LVPO to V³⁺-containing LVPF and therefore easier substitution of F for O. The formed fluorinated phase had an operating potential of ~4.25 V vs. Li/Li⁺ for V³⁺/V⁴⁺ redox couple compared to 3.95 V potential of starting ε -LVPO for the V⁴⁺/V⁵⁺ redox couple. The electrochemical signature (appearance of a step at oxidation half-cycle due to formation of Li_{0.67}VPO₄F intermediate phase) in addition to the observed potential confirmed the LVPF-type nature of the phase. The polarization of the new fluorinated phase was also comparable to LVPF, despite a larger particle size. Therefore, it can be concluded that the reminiscent amorphous carbon of PTFE in this synthesis method is

more effective in increasing the electronic conductivity of the phosphate material than the carbon particles in conventional LVPF synthesis. Hence, PTFE can be used not only for the fluorination purpose in such synthesis techniques, but also to provide a higher conductivity for the particles due to the remaining carbon after the decomposition.

CHAPTER6: CONCLUSIONS

In this thesis work, fluorination of vanadium oxy-phosphate (vanadyl phosphate) compounds as high-energy Li ion battery cathode materials was investigated. Firstly, vanadium oxy-phosphates as the intermediate compounds were synthesized. These materials were then used during high-temperature fluorination process to achieve new materials with higher energy density. Lithium fluoride and PTFE powders were used in this work as the fluorine resources. The obtained intermediate phases and the fluorinated phases were the subjects of structural and chemical characterization including electrochemical characterization. The results were provided in three chapters.

In Chapter 3, the synthesis and characterization of the intermediate vanadium oxy-phosphates, β -VPO, ε -LVPO and β -LVPO, were discussed. The synthesis of a pure β -VPO (V^{4+}) as the high-temperature polymorph of VPO was challenging. Several polymorphs formed simultaneously and β -VPO could only be produced at temperatures >700 °C during long heating durations (>24 h). Synthesis through oxidation of VPO_4 (V^{3+}) phase proved to be the most efficient. This was attributed to the higher oxidation tendency of $V^{3+}PO_4$ with respect to $V^{3+}_2O_3$. This phase with an orthorhombic *Pnma* lattice showed an operating potential of ~ 3.97 V vs. Li/Li⁺ for V^{5+}/V^{4+} redox couple in the electrochemical cycling.

The lithiated ε -LVPO (V^{4+}) phase was also synthesized at high temperatures (700 °C). The synthesis of a pure phase was easier with respect to β -VPO. Relatively large prismatic particles (1-2 μ m) as nicely-shaped crystals were formed. The phase crystallized in a Tavorite framework with a $P\bar{1}$ triclinic lattice. The operating potential was ~ 3.95 V for the V^{4+}/V^{5+} redox couple. The second lithiated polymorph, β -LVPO (V^{4+}), was synthesized through reduction of V_2O_5 (V^{5+}) around 600 °C. The particles formed as nano-sheets with the orthorhombic *Pnma* lattice structure. β -LVPO had an operating potential ~ 3.98 V vs. Li/Li⁺ for V^{4+}/V^{5+} redox couple, which was slightly higher than the one for ε -phase (3.95 V). This was attributed to the higher oxidation state of V in β -LVPO

compared to ϵ -LVPO, which contains higher concentration of oxygen vacancies. The higher charge/discharge capacity of β -LVPO was attributed to its better kinetics of Li diffusion.

In Chapter 4, the fluorination of β -VPO and ϵ -LVPO through incorporation of LiF was described. The synthesis, characterization and electrochemical properties of the fluorinated phases were discussed. The LiF incorporation reaction in β -VPO at high temperatures using the stainless-steel reactor resulted in formation of a fluorinated vanadyl phosphate phase with a Tavorite structure. The XRD results showed the formation of such a phase at temperatures above 500 °C. Increasing the temperature until 700 °C resulted in higher LiF consumption, while the main phase (VPOF) peaks shifted more towards LVPF phase peaks. Therefore, at higher temperatures, an LVPF-type phase was more likely to appear. NMR results confirmed the formation of an LVPF-type phase, since the ^6Li and ^{31}P shifts appeared at the location of LVPF NMR shifts. Additional signals at 84 ppm and 186 ppm were assigned to the presence of vanadyl defects. The electrochemical characterization using the galvanostatic cycling showed that either the obtained material is a composite of various similar phases or it undergoes various steps in lithium extraction/insertion reaction. Nevertheless, LVPF-type phase had the highest capacity with a ~ 4.21 V potential vs. Li/Li^+ . The decomposition of the β -VPO material during the heating process in the stainless-steel reactor showed the instability of the phase. This caused a difficulty of reproduction in the synthesized materials. In addition, it was presumed that the formation of LVPF-type phase was due to the reaction of VPO_4 (one of the decomposition products of VPO) with LiF. Therefore, further studies are needed in order to explore the phase formation and stability.

The LiF incorporation reaction in ϵ -LVPO took place at temperatures above 600 °C. A new Tavorite-structured phase was formed through this reaction, which increased in amount by increasing the heating temperature. The dependency of the reaction on the heating temperature was obvious, since at 700 °C, the synthesis product was a composite of LVPO and new LVPOF phase, while at 800 °C, the product was mainly LVPOF. This phase had a larger lattice volume compared to precursor LVPO. This was a result of larger F atoms incorporation in the lattice. The ^7Li and ^{31}P MAS-NMR results showed that the new oxy/fluoro-phosphate LVPOF phase had an LVPO-type structure, meaning that the framework was preserved during the reaction. Further lattice refinement studies showed that about 20% of the O atoms on the V ligands of VO_6 octahedral chains were substituted

by F atoms. XANES analysis showed that vanadium in LVPOF had a mixed +3/+4 valence state. However, the exact value could not be assessed due to the effect of F (ionicity of V-F bond) on the edge absorption of spectrum. The distortion of VO₆ octahedra in LVPO was reduced in LVPOF. The presence of mixed O/F ligands, causing the V reduction, resulted in a higher symmetry in the octahedra. The presence of F in the chemical composition of LVPOF was demonstrated by EDX analysis. However, analysis on several individual particles by STEM-EDX showed that the F amount varied among particles, pointing of a solid-solution material. Local fluctuations were observed in the V edge position of EELS spectra on different particles, which was connected to the effect of F amount. Another observation in this regard was the infeasibility of LVPOF structure fitting using experimentally-obtained XRD CIF file. The latter could not be fitted on local electron diffraction pattern of particles, which was reflected also on STEM atomic resolution images. Therefore, this study showed the significance of systematic characterization at both micro- and nano-scale in order to obtain insights on material properties. The operating potential of the LVPOF phase at high-voltage range was increased compared to that of the precursor LVPO (4.12 V and 3.95 V vs. Li/Li⁺, respectively). The formation of ionic V-F bonds in LVPOF compared to V-O and highly covalent V=O bonds in LVPO increased the redox potential. Additionally, LVPOF had a higher charge capacity than LVPO. This was attributed to the effect of F on improving the slow kinetics of Li diffusion in LVPO and increasing the Li exchange during the electrochemical reaction. It was possible to improve the properties of LVPO by tuning its crystal structure, since the main framework did not change during the fluorination. Therefore, we can conclude that the LiF incorporation in β-VPO resulted in formation of LVPF-type phase, while the similar reaction with ε-LVPO, resulted in formation of LVPO-type phase.

In Chapter 5, the fluorination of β-VPO and ε-LVPO using PTFE as the F source was described. The reaction of β-VPO with PTFE in the reactor resulted in production of a pyrophosphate phase. This was attributed to the instability of β-VPO phase during high-temperature treatment inside of the sealed stainless-steel reactor.

The fluorination of ε-LVPO by PTFE in a stoichiometric mix was possible at temperatures as high as 700 °C. At this temperature, half of the ε-LVPO precursor was consumed, reacted with the decomposed PTFE and transformed to LVPF. The ε-LVPO phase was not stable at higher heating temperatures. In addition, higher synthesis duration

did not increase the amount of fluorinated phase. In another approach, PTFE was used in excess amount in the reactants mixture. This provided a higher F amount in the synthesis medium, which therefore, increased the fluorination probability. The stronger F atmosphere and possibly the higher pressure inside the reactor after PTFE decomposition also affected the stability of ϵ -LVPO. It was possible to increase the synthesis temperature to 900 °C, where ϵ -LVPO transformed to “LVPF” with a small amount of $\text{Li}_3\text{V}_2(\text{PO}_4)_3$ impurity. The structure refinement confirmed the formation of LVPF. The microscopic observations showed the presence of leftover carbon from PTFE decomposition as a cloud surrounding the particles. Additionally, the electrochemical signature of the fluorinated LVPF-type phase was similar to LVPF, with an operating potential of 4.25 V vs. Li/Li^+ . The polarization of the former was comparable to latter, despite of a larger particle size. Therefore, it can be concluded that the reminiscent amorphous carbon of PTFE in this synthesis method is more effective in increasing the electronic conductivity of the phosphate material than the carbon particles in conventional LVPF synthesis.

To the best of our knowledge, PTFE was used for the first time in this work as the only source of fluorine for a fluorination purpose. In general, the strong C-F bonds in PTFE limits its application for such works. However, the results showed successfully the possibility of using PTFE for fluorinating vanadium oxy-phosphate materials. In addition, the presence of reminiscent amorphous carbon from the decomposition of PTFE can increase the electronic conductivity of the base particles, which is highly desirable especially in phosphate-type cathode materials. Therefore, this fluorination method can be extended to other materials and other applications, as well. This can be an interesting subject for future work.

Another significant observation was that fluorination of ϵ -LVPO with PTFE resulted in formation of an LVPF-type phase, while during fluorination with LiF, an LVPO-type phase was formed. It can be concluded that the incorporation of Li atoms of LiF in the ϵ -LVPO structure could play a role in stabilization of the main crystal framework, where desirable. Such results contribute to more profound understanding of the fluorination induced by different fluorinating agents.

The correlation between structural, chemical and electrochemical characterization results presented in this work was essential to attain understanding of structure-property

relationship and its importance on the tuning of the electrochemical properties of vanadium oxy/fluoro-phosphate compounds.

CHAPTER7: PERSPECTIVES FOR FUTURE WORK

In this work, in addition to β -VPO and ε -LVPO, β -LVPO was synthesized, as it was described in Chapter 3. It is of interest to investigate the possibility of fluorination of this polymorph along with ε -LVPO. Comparison of the synthesis results from these two polymorphs can give clearer insight into the fluorination mechanism and its effects on the properties in relation to the structure. Therefore, some experiments were initiated through fluorination with PTFE. Here, some synthesis and characterization results are provided as bullet points. Because of the successful preliminary results, the continuation of this line of study is planned for the future work.

- ❖ For the related experiments, a similar reaction path was applied as previously described synthesis on other vanadium oxy-phosphate phases. For this, β -LVPO powder was mixed with PTFE powder in stoichiometric amounts and pellets were prepared. These pellets were placed in stainless steel reactors and were heat-treated at high temperatures for 30 min. Since the β -phase is a low-temperature polymorph, any further reaction could be expected to take place at lower temperatures, with respect to ε -phase. Therefore, 600 °C and 700 °C temperatures were chosen for the preliminary tests. A chemical reaction according to Equation 7-1 was predicted.



- ❖ XRD patterns of the samples synthesized at 600 °C and 700 °C (named β -LVPO/T) are presented in Figure 7-1. For the sake of comparison, patterns of β -LVPO and LVPF are also shown in this figure. The patterns show that heating the mixture of β -LVPO and PTFE resulted in formation of a triclinic-structured (Tavorite-type) phase. At 600 °C (β -LVPO/T-600), two phases are present as the precursor β -LVPO and the newly formed triclinic phase. At 700 °C (β -LVPO/T-700), only one triclinic phase is present. The green dashed lines show the position

of some of the peaks of this phase. One can notice that this phase, although similar, but is still distinctive from LVPF phase. In addition, the newly formed phase is also different in (β -LVPO/T-600) and (β -LVPO/T-700) samples. For instance, the peak located at $\sim 27.5^\circ$ in the former sample, is shifted towards lower angles ($\sim 27.1^\circ$) in the later one.

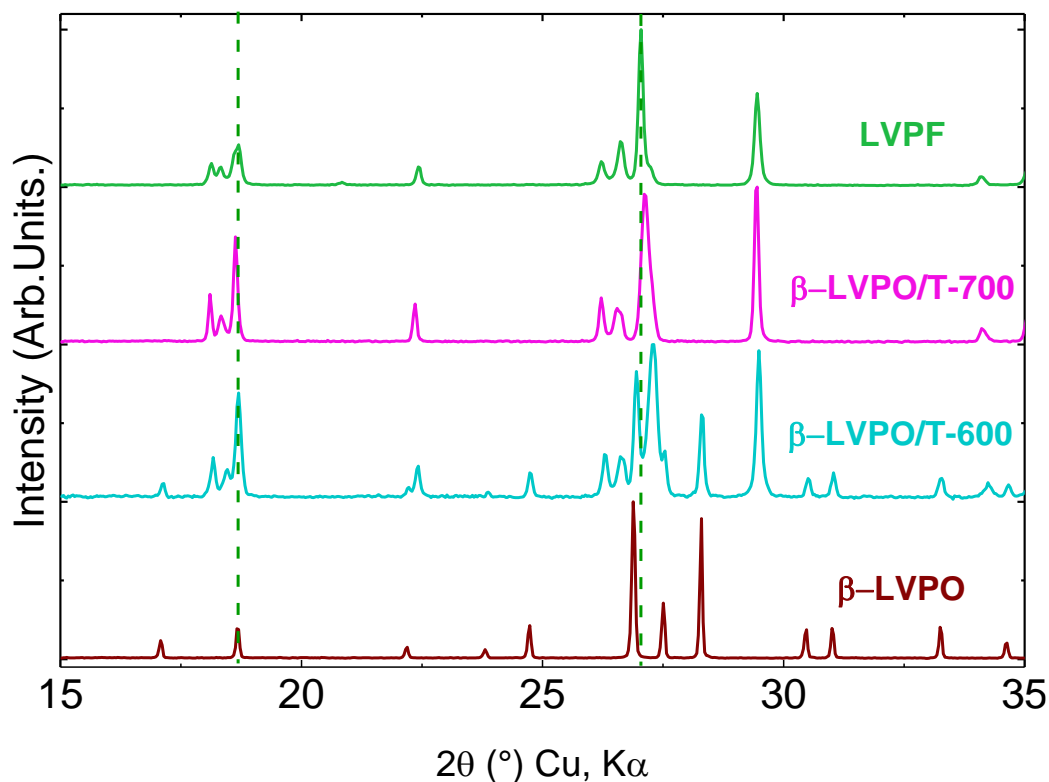


Figure 7-1 XRD patterns of β -LVPO+PTFE mixture (β -LVPO/T) at RT and heat-treated at 600 °C and 700 °C in comparison to β -LVPO and LVPF. The green dashed lines show the location of LVPF peaks.

- ❖ Figure 7-2 shows the microstructure of sample β -LVPO/T-700. The agglomerates are composed of crystalline particles with particle size below 500 nm. The fluorination process at high temperatures resulted in formation of rock-shape particles from the precursor β -LVPO nano-sheets (Figure 3-20). These particles also differ in size and shape from the fluorinated particles of ϵ -LVPO (Figure 5-4).

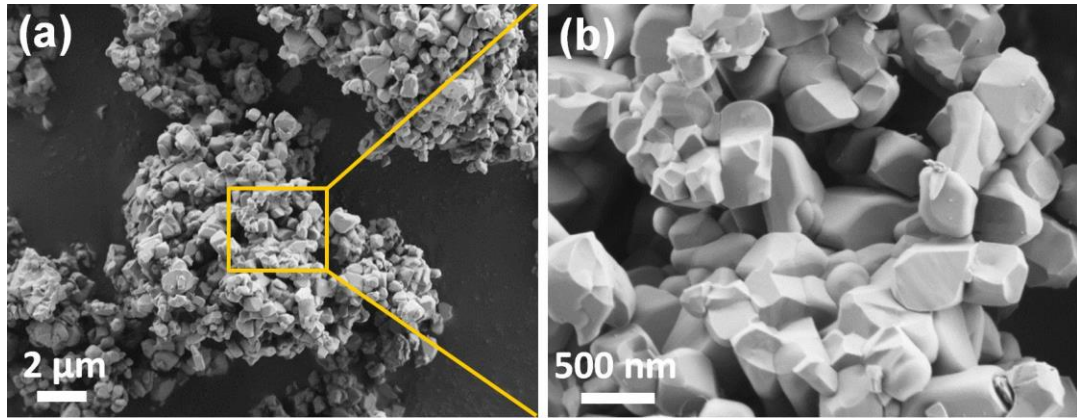


Figure 7-2 SEM micrographs of sample β -LVPO/T-700, (a) at low magnification, showing the agglomerates and (b) at high magnification showing the single particles morphology.

- ❖ The preliminary lattice refinement results showed that β -LVPO/T-700 has an LVPF-type Tavorite crystal structure. However, an acceptable fit is not obtained yet and further work is needed to study the crystal structure more precisely. The refined lattice parameters are as following: a (Å)=5.1644(4), b (Å)=5.3017(8), c (Å)=7.2255(2), α (°)=107.4291(3), β (°)=107.8249(9), γ (°)=98.4994(5), and V (Å³)=173.337(4).
- ❖ Electrochemical behavior of the PTFE-fluorinated phase (β -LVPO/T-700) is compared to LVPF and precursor β -LVPO in Figure 7-3, where galvanostatic cycling curves are shown at high-voltage range (3.0-4.5 V vs. Li/Li⁺). The cycling behavior of the fluorinated sample is clearly different than β -LVPO (operating potential ~3.97 V). Although this sample shows an LVPF-type voltage feature, it is still different than LVPF. The operating potential is slightly lower than LVPF (4.22 V vs. 4.25 V) and the electrochemical signature is also different. The step in the Li insertion process of LVPF is absent for sample β -LVPO/T-700. Instead, the Li insertion/extraction process proceeds as a plateau (two-phase mechanism) for about 60% of the capacity and in the rest, a process similar to a sloping slope voltage (solid-solution mechanism) takes place.

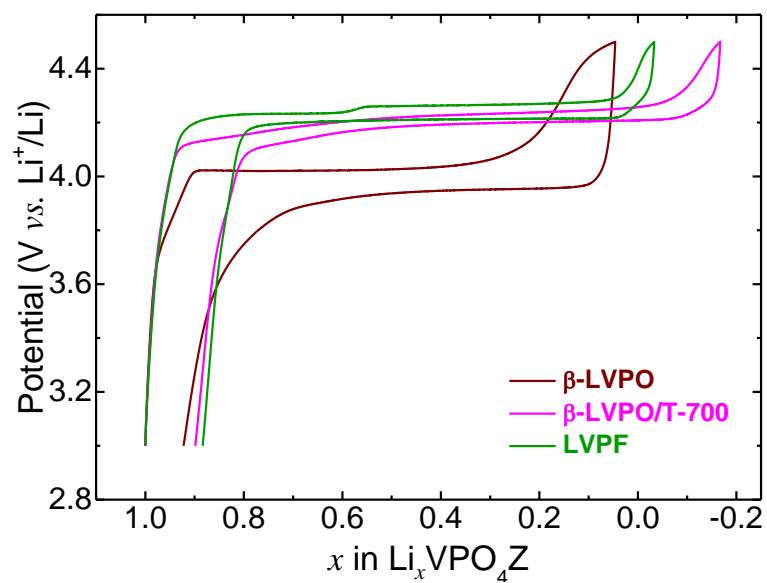


Figure 7-3 Galvanostatic cycling curve of β -LVPO, β -LVPO/T-700 and LVPF at second cycle at high-voltage range (3.0-4.5 V vs. Li/Li⁺) with a current density corresponding to C/50 cycling rate.

REFERENCES

- Allen, C. J., Jia, Q., Chinnasamy, C., Mukerjee, S., & Abraham, K. (2011). Synthesis, structure and electrochemistry of lithium vanadium phosphate cathode materials. *Journal of The Electrochemical Society*, *158*(12), A1250-A1259.
- Antipov, E. V., Khasanova, N. R., & Fedotov, S. S. (2015). Perspectives on Li and transition metal fluoride phosphates as cathode materials for a new generation of Li-ion batteries. *IUCrJ*, *2*(1), 85-94.
- Armand, M., & Tarascon, J.-M. (2008). Building better batteries. *nature*, *451*(7179), 652-657.
- Ateba Mba, J.-M. (2013). *New Lithium Transition Metal Fluorophosphates as Positive Electrode Materials for Li-ion Batteries*. Bordeaux 1,
- Ateba Mba, J.-M., Masquelier, C., Suard, E., & Croguennec, L. (2012). Synthesis and crystallographic study of homeotypic LiVPO₄F and LiVPO₄O. *Chemistry of Materials*, *24*(6), 1223-1234.
- Ateba Mba, J.-M. A., Croguennec, L., Basir, N. I., Barker, J., & Masquelier, C. (2012). Lithium insertion or extraction from/into tavorite-type LiVPO₄F: an in situ X-ray diffraction study. *Journal of The Electrochemical Society*, *159*(8), A1171-A1175.
- Azmi, B. M., Ishihara, T., Nishiguchi, H., & Takita, Y. (2002). Cathodic performance of VOPO₄ with various crystal phases for Li ion rechargeable battery. *Electrochimica Acta*, *48*(2), 165-170.
- Azmi, B. M., Ishihara, T., Nishiguchi, H., & Takita, Y. (2003). Vanadyl phosphates of VOPO₄ as a cathode of Li-ion rechargeable batteries. *Journal of Power Sources*, *119*, 273-277.
- Barker, J., Gover, R., Burns, P., & Bryan, A. (2005). A symmetrical lithium-ion cell based on lithium vanadium fluorophosphate, LiVPO₄F. *Electrochemical and Solid-State Letters*, *8*(6), A285-A287.
- Barker, J., Gover, R., Burns, P., Bryan, A., Saidi, M., & Swoyer, J. (2005). Structural and electrochemical properties of lithium vanadium fluorophosphate, LiVPO₄F. *Journal of Power Sources*, *146*(1-2), 516-520.
- Barker, J., Saidi, M., & Swoyer, J. (2003). Electrochemical insertion properties of the novel lithium vanadium fluorophosphate, LiVPO₄ F. *Journal of The Electrochemical Society*, *150*(10), A1394-A1398.
- Berrah, F., Guesdon, A., Leclaire, A., Borel, M.-M., Provost, J., & Raveau, B. (2001). The vanadium monophosphates AVOPO₄: Synthesis of a second form β-KVOPO₄ and structural relationships in the series. *Solid state sciences*, *3*(4), 477-482.
- Bianchini, M., Ateba-Mba, J., Dagault, P., Bogdan, E., Carlier, D., Suard, E., . . . Croguennec, L. (2014). Multiple phases in the ε-VPO 4 O–LiVPO 4 O–Li 2 VPO 4 O system: a combined solid state electrochemistry and diffraction structural study. *Journal of Materials Chemistry A*, *2*(26), 10182-10192.
- Boivin, É. (2017). *Crystal chemistry of vanadium phosphates as positive electrode materials for Li-ion and Na-ion batteries*. Amiens,
- Boivin, E., Chotard, J.-N. I., Ménétrier, M., Bourgeois, L., Bamine, T., Carlier, D., . . . Croguennec, L. (2016). Oxidation under air of tavorite LiVPO₄F: Influence of vanadyl-type defects on its electrochemical properties. *The Journal of Physical Chemistry C*, *120*(46), 26187-26198.
- Boivin, E., David, R. n., Chotard, J.-N. I., Bamine, T., Iadecola, A., Bourgeois, L., . . . Masquelier, C. (2018). LiVPO₄F_{1-y}O_y Tavorite-Type Compositions: Influence of the Concentration of Vanadyl-Type Defects on the Structure and Electrochemical Performance. *Chemistry of Materials*, *30*(16), 5682-5693.
- Boivin, E., Iadecola, A., Fauth, F., Chotard, J.-N., Masquelier, C., & Croguennec, L. (2019). Redox Paradox of Vanadium in Tavorite LiVPO₄F_{1-y}O_y. *Chemistry of Materials*, *31*(18), 7367-7376.

- Bragg, W. L. (1913). The structure of some crystals as indicated by their diffraction of X-rays. *Proceedings of the Royal Society of London. Series A, Containing papers of a mathematical and physical character*, 89(610), 248-277.
- Callister, W. D., & Rethwisch, D. G. (2011). *Materials science and engineering* (Vol. 5): John Wiley & sons NY.
- Chen, Z., Chen, Q., Chen, L., Zhang, R., Zhou, H., Chernova, N. A., & Whittingham, M. S. (2013). Electrochemical Behavior of Nanostructured ϵ -VOPO₄ over Two Redox Plateaus. *Journal of The Electrochemical Society*, 160(10), A1777.
- Chen, Z., Chen, Q., Wang, H., Zhang, R., Zhou, H., Chen, L., & Whittingham, M. S. (2014). A β -VOPO₄/ ϵ -VOPO₄ composite Li-ion battery cathode. *Electrochemistry communications*, 46, 67-70.
- Chung, S.-Y., Bloking, J. T., & Chiang, Y.-M. (2002). Electronically conductive phospho-olivines as lithium storage electrodes. *Nature materials*, 1(2), 123-128.
- Clark, R. (1968). *The Chemistry of Titanium and Vanadium* Elsevier Pub. Co., New York, 266.
- Degen, T., Sadki, M., Bron, E., König, U., & Nénert, G. (2014). The highscore suite. *Powder Diffraction*, 29(S2), S13-S18.
- Dominko, R., Garrido, C. V.-A., Bele, M., Kuezma, M., Arcon, I., & Gaberscek, M. (2011). Electrochemical characteristics of Li₂-xVTiO₄ rock salt phase in Li-ion batteries. *Journal of Power Sources*, 196(16), 6856-6862.
- Dugas, R., Forero-Saboya, J. D., & Ponrouch, A. (2019). Methods and Protocols for Reliable Electrochemical Testing in Post-Li Batteries (Na, K, Mg, and Ca). *Chemistry of Materials*, 31(21), 8613-8628.
- Dupre, N., Gaubicher, J., Angenault, J., & Quarton, M. (2004). Electrochemical study of intercalated vanadyl phosphate. *Journal of Solid State Electrochemistry*, 8(5), 322-329.
- Dupre, N., Gaubicher, J., Angenault, J., Wallez, G., & Quarton, M. (2001). Electrochemical performance of different Li-VOPO₄ systems. *Journal of Power Sources*, 97, 532-534.
- Dupre, N., Wallez, G., Gaubicher, J., & Quarton, M. (2004). Phase transition induced by lithium insertion in α I- and α II-VOPO₄. *Journal of Solid State Chemistry*, 177(8), 2896-2902.
- Duscher, G. (2019). <http://web.utk.edu/~gduscher/eels.html> Lectures, NC State University.
- Eames, C., Armstrong, A., Bruce, P., & Islam, M. (2012). Insights into changes in voltage and structure of Li₂FeSiO₄ polymorphs for lithium-ion batteries. *Chemistry of Materials*, 24(11), 2155-2161.
- Ellingham, H. (1944). Transactions and communications. *J. Soc. Chem. Ind.*, 63(5), 125.
- Gaubicher, J., Le Mercier, T., Chabre, Y., Angenault, J., & Quarton, M. (1999). Li/ β -VOPO₄: A New 4 V System for Lithium Batteries. *Journal of The Electrochemical Society*, 146(12), 4375-4379.
- Gibot, P., Casas-Cabanas, M., Laffont, L., Levasseur, S., Carlach, P., Hamelet, S., . . . Masquelier, C. (2008). Room-temperature single-phase Li insertion/extraction in nanoscale Li_xFePO₄. *Nature materials*, 7(9), 741-747.
- Girgsdies, F., Dong, W.-S., Bartley, J. K., Hutchings, G. J., Schlögl, R., & Ressler, T. (2006). The crystal structure of ϵ -VOPO₄. *Solid state sciences*, 8(7), 807-812.
- Girgsdies, F., Schneider, M., Brückner, A., Ressler, T., & Schlögl, R. (2009). The Crystal Structure of δ -VOPO₄ and Its Relationship to ω -VOPO₄. *Solid state sciences*, 11(7), 1258-1264.
- Goldstein, J. I., Newbury, D. E., Michael, J. R., Ritchie, N. W., Scott, J. H. J., & Joy, D. C. (2017). *Scanning electron microscopy and X-ray microanalysis*: Springer.
- Goodenough, J. B., & Kim, Y. (2010). Challenges for rechargeable Li batteries. *Chemistry of Materials*, 22(3), 587-603.
- Goodenough, J. B., & Park, K.-S. (2013). The Li-ion rechargeable battery: a perspective. *Journal of the American Chemical Society*, 135(4), 1167-1176.
- Gopal, R., & Calvo, C. (1972). Crystal structure of β VPO₅. *Journal of Solid State Chemistry*, 5(3), 432-435.
- Gover, R., Burns, P., Bryan, A., Saidi, M., Swoyer, J., & Barker, J. (2006). LiVPO₄F: A new active material for safe lithium-ion batteries. *Solid State Ionics*, 177(26-32), 2635-2638.

- Groat, L. A., Chakoumakos, B. C., Brouwer, D. H., Hoffman, C. M., Fyfe, C. A., Morell, H., & Schultz, A. J. (2003). The amblygonite (LiAlPO₄F)-montebrasite (LiAlPO₄OH) solid solution: A combined powder and single-crystal neutron diffraction and solid-state ⁶Li MAS, CP MAS, and REDOR NMR study. *American Mineralogist*, 88(1), 195-210.
- Groat, L. A., Raudsepp, M., Hawthorne, F. C., Ercit, T. S., Sherriff, B. L., & Hartman, J. S. (1990). The amblygonite-montebrasite series; characterization by single-crystal structure refinement, infrared spectroscopy, and multinuclear MAS-NMR spectroscopy. *American Mineralogist*, 75(9-10), 992-1008.
- Guilmard, M., Pouillier, C., Croguennec, L., & Delmas, C. (2003). Structural and electrochemical properties of LiNi_{0.70}Co_{0.15}Al_{0.10}O₂. *Solid State Ionics*, 160(1-2), 39-50.
- Harrison, K. L., Bridges, C. A., Segre, C. U., Varnado Jr, C. D., Applestone, D., Bielawski, C. W., . . . Manthiram, A. (2014). Chemical and electrochemical lithiation of LiVOPO₄ cathodes for lithium-ion batteries. *Chemistry of Materials*, 26(12), 3849-3861.
- Harrison, K. L., & Manthiram, A. (2013). Microwave-assisted solvothermal synthesis and characterization of various polymorphs of LiVOPO₄. *Chemistry of Materials*, 25(9), 1751-1760.
- Hautier, G., Jain, A., Ong, S. P., Kang, B., Moore, C., Doe, R., & Ceder, G. (2011). Phosphates as lithium-ion battery cathodes: an evaluation based on high-throughput ab initio calculations. *Chemistry of Materials*, 23(15), 3495-3508.
- He, G., Huq, A., Kan, W. H., & Manthiram, A. (2016). β-NaVOPO₄ obtained by a low-temperature synthesis process: a new 3.3 V cathode for sodium-ion batteries. *Chemistry of Materials*, 28(5), 1503-1512.
- He, G., Kan, W. H., & Manthiram, A. (2018). Delithiation/lithiation behaviors of three polymorphs of LiVOPO₄. *Chemical communications*, 54(94), 13224-13227.
- Hidalgo, M. F. V., Lin, Y.-C., Grenier, A., Xiao, D., Rana, J., Tran, Omenya, F. O. (2019). Rational synthesis and electrochemical performance of LiVOPO₄ polymorphs. *Journal of Materials Chemistry A*, 7(14), 8423-8432.
- IPCC, & Team, C. W. (2014). Climate change 2014: Synthesis report. *Contribution of working groups I, II and III to the fifth assessment report of the intergovernmental panel on climate change*, 27, 408.
- Jordan, B., & Calvo, C. (1973). Crystal Structure of α-VPO₅. *Canadian Journal of Chemistry*, 51(16), 2621-2625.
- Julien, C., Mauger, A., Vijn, A., & Zaghbi, K. (2016). Lithium batteries. In *Lithium Batteries* (pp. 29-68): Springer.
- Kalluri, S., Yoon, M., Jo, M., Park, S., Myeong, S., Kim, J., Dou, S. X., Guo, Z., Cho, J., (2017). Surface Engineering Strategies of Layered LiCoO₂ Cathode Material to Realize High-Energy and High-Voltage Li-Ion Cells. *Adv. Energy Mater.* 7, 1601507.
- Kerr, T., Gaubicher, J., & Nazar, L. (2000). Highly Reversible Li Insertion at 4 V in ε-VOPO₄/α-LiVOPO₄ Cathodes. *Electrochemical and Solid-State Letters*, 3(10), 460-462.
- Kim, M., Lee, S., & Kang, B. (2017). High Energy Density Polyanion Electrode Material: LiVPO₄O_{1-x}F_x (x ≈ 0.25) with Tavorite Structure. *Chemistry of Materials*, 29(11), 4690-4699.
- Launay, M., Boucher, F., Gressier, P., & Ouvrard, G. (2003). A DFT study of lithium battery materials: application to the β-VOXO₄ systems (X= P, As, S). *Journal of Solid State Chemistry*, 176(2), 556-566.
- Lavrov, A., Nikolaev, V., Sadikov, G., & Porai-Koshits, M. (1982). *Synthesis and crystal structure of vanadyl lithium orthophosphate LiVOPO₄*. Paper presented at the Soviet Physics Doklady.
- Li, W., Song, B., & Manthiram, A. (2017). High-voltage positive electrode materials for lithium-ion batteries. *Chemical Society Reviews*, 46(10), 3006-3059.
- Lin, Y.-C., Hidalgo, M. F., Chu, I.-H., Chernova, N. A., Whittingham, M. S., & Ong, S. P. (2017). Comparison of the polymorphs of VOPO₄ as multi-electron cathodes for rechargeable alkali-ion batteries. *Journal of Materials Chemistry A*, 5(33), 17421-17431.

- Lin, Y.-C., Wen, B., Wiaderek, K. M., Sallis, S., Liu, H., Lapidus, S. H., . . . Karki, K. (2016). Thermodynamics, kinetics and structural evolution of ϵ -LiVOPO₄ over multiple lithium intercalation. *Chemistry of Materials*, 28(6), 1794-1805.
- Ling, C., Zhang, R., & Mizuno, F. (2014). Phase stability and its impact on the electrochemical performance of VOPO₄ and LiVOPO₄. *Journal of Materials Chemistry A*, 2(31), 12330-12339.
- Ma, R., Shao, L., Wu, K., Shui, M., Wang, D., Long, N., . . . Shu, J. (2014). Effects of oxidation on structure and performance of LiVPO₄F as cathode material for lithium-ion batteries. *Journal of Power Sources*, 248, 874-885.
- MacNeil, D. D., & Dahn, J. R. (2001). The reaction of charged cathodes with nonaqueous solvents and electrolytes: I. Li_{0.5}CoO₂. *Journal of The Electrochemical Society*, 148(11), A1205-A1210.
- Manthiram, A. (2011). Materials challenges and opportunities of lithium ion batteries. *The Journal of Physical Chemistry Letters*, 2(3), 176-184.
- Manthiram, A., & Goodenough, J. B. (1989). Lithium insertion into Fe₂(SO₄)₃ frameworks. *Journal of Power Sources*, 26(3-4), 403-408.
- Masquelier, C., & Croguennec, L. (2013). Polyanionic (phosphates, silicates, sulfates) frameworks as electrode materials for rechargeable Li (or Na) batteries. *Chemical Reviews*, 113(8), 6552-6591.
- Messinger, R. J., Ménétrier, M., Salager, E., Boulineau, A., Duttine, M., Carlier, D., . . . Massiot, D. (2015). Revealing defects in crystalline lithium-ion battery electrodes by solid-state NMR: applications to LiVPO₄F. *Chemistry of Materials*, 27(15), 5212-5221.
- Mestre-Aizpurua, F., Hamelet, S., Masquelier, C., & Palacin, M. (2010). High temperature electrochemical performance of nanosized LiFePO₄. *Journal of Power Sources*, 195(19), 6897-6901.
- Mizushima, K., Jones, P., Wiseman, P., & Goodenough, J. B. (1980). Li_xCoO₂ (0 < x < 1): A new cathode material for batteries of high energy density. *Materials Research Bulletin*, 15(6), 783-789.
- Ni, Y., & He, G. (2018). Stable cycling of β -VOPO₄/NaVOPO₄ cathodes for sodium-ion batteries. *Electrochimica Acta*, 292, 47-54.
- Ohzuku, T., & Makimura, Y. (2001). Layered lithium insertion material of LiCo_{1/3}Ni_{1/3}Mn_{1/3}O₂ for lithium-ion batteries. *Chemistry Letters*, 30(7), 642-643.
- Onoda, M., & Ishibashi, T. (2015). Phase Transition and Spin Dynamics of the LiVFPO₄ Insertion Electrode with the S= 1 Linear Chain and the Development of F-O Mixed System. *Journal of the Physical Society of Japan*, 84(4), 044802.
- Padhi, A. K., Nanjundaswamy, K. S., & Goodenough, J. B. (1997). Phospho-olivines as positive-electrode materials for rechargeable lithium batteries. *Journal of The Electrochemical Society*, 144(4), 1188-1194.
- Park, N.-G., Kim, K. M., & Chang, S. H. (2001). Sonochemical synthesis of the high energy density cathode material VOPO₄·2H₂O. *Electrochemistry communications*, 3(10), 553-556.
- Pell, A. J., Clément, R. J., Grey, C. P., Emsley, L., & Pintacuda, G. (2013). Frequency-stepped acquisition in nuclear magnetic resonance spectroscopy under magic angle spinning. *The Journal of chemical physics*, 138(11), 114201.
- Penner-Hahn, J. (2005). X-ray absorption spectroscopy. The University of Michigan. *Ann Arbor, MI, USA*.
- Pivko, M., Arcon, I., Bele, M., Dominko, R., & Gaberscek, M. (2012). A₃V₂(PO₄)₃ (A= Na or Li) probed by in situ X-ray absorption spectroscopy. *Journal of Power Sources*, 216, 145-151.
- Raccichini, R., Amores, M., & Hinds, G. (2019). Critical Review of the Use of Reference Electrodes in Li-Ion Batteries: A Diagnostic Perspective. *Batteries*, 5(1), 12.
- Ravel, B., & Newville, M. (2005). ATHENA, ARTEMIS, HEPHAESTUS: data analysis for X-ray absorption spectroscopy using IFEFFIT. *Journal of synchrotron radiation*, 12(4), 537-541.

- Rehr, J., Albers, R., & Zabinsky, S. (1992). High-order multiple-scattering calculations of X-ray-absorption fine structure. *Physical review letters*, 69(23), 3397.
- Rodriguez-Carvajal, J. (1990). *FULLPROF: a program for Rietveld refinement and pattern matching analysis*. Paper presented at the satellite meeting on powder diffraction of the XV congress of the IUCr.
- Schindler, M., Hawthorne, F., & Baur, W. (2000). Crystal chemical aspects of vanadium: polyhedral geometries, characteristic bond valences, and polymerization of (VO n) polyhedra. *Chemistry of Materials*, 12(5), 1248-1259.
- Semsari Parapari, S., Ateba Mba, J.-M., Tchernychova, E., Mali, G., Arçon, I., Kapun, G., . . . Dominko, R. (2020). Effects of a Mixed O/F Ligand in the Tavorite-Type LiVPO4O Structure. *Chemistry of Materials*, 32(1), 262-272. doi:10.1021/acs.chemmater.9b03698
- Shi, Y., Zhou, H., Britto, S., Seymour, I. D., Wiaderek, K. M., Omenya, F., . . . Whittingham, M. S. (2019). A high-performance solid-state synthesized LiVOPO4 for lithium-ion batteries. *Electrochemistry communications*, 105, 106491.
- Sirisopanaporn, C., Masquelier, C., Bruce, P. G., Armstrong, A. R., & Dominko, R. (2011). Dependence of Li2FeSiO4 electrochemistry on structure. *Journal of the American Chemical Society*, 133(5), 1263-1265.
- Siu, C., Seymour, I. D., Britto, S., Zhang, H., Rana, J., Feng, J., . . . Zhou, G. (2018). Enabling multi-electron reaction of ε-VOPO 4 to reach theoretical capacity for lithium-ion batteries. *Chemical communications*, 54(56), 7802-7805.
- Song, Y., Zavalij, P. Y., & Whittingham, M. S. (2005). ε-VOPO4: electrochemical synthesis and enhanced cathode behavior. *Journal of The Electrochemical Society*, 152(4), A721-A728.
- Stadelmann, P. (1999). Electron microscopy software-java version (jems). *CIME—EPFL: Lausanne, Switzerland, 2011*.
- Stevie, F., Giannuzzi, L., & Prentner, B. (2005). The focused ion beam instrument. In *Introduction to Focused Ion Beams* (pp. 1-12): Springer.
- Sun, W., & Du, J. (2017). Structural stability, electronic and thermodynamic properties of VOPO4 polymorphs from DFT+ U calculations. *Computational Materials Science*, 126, 326-335.
- Sun, X., Xu, Y., Jia, M., Ding, P., Liu, Y., & Chen, K. (2013). High performance LiV 0.96 Mn 0.04 PO 4 F/C cathodes for lithium-ion batteries. *Journal of Materials Chemistry A*, 1(7), 2501-2507.
- Tan, H., Verbeeck, J., Abakumov, A., & Van Tendeloo, G. (2012). Oxidation state and chemical shift investigation in transition metal oxides by EELS. *Ultramicroscopy*, 116, 24-33.
- Viswanath, R., & Miller, P. (1979). High temperature phase transition in NH4H2PO4. *Solid State Communications*, 32(8), 703-706.
- Wang, H., Jang, Y. I., Huang, B., Sadoway, D. R., & Chiang, Y. M. (1999). TEM study of electrochemical cycling-induced damage and disorder in LiCoO2 cathodes for rechargeable lithium batteries. *Journal of The Electrochemical Society*, 146(2), 473-480.
- Whittingham, M. S. (2014). Ultimate limits to intercalation reactions for lithium batteries. *Chemical Reviews*, 114(23), 11414-11443.
- Whittingham, M. S., Siu, C., & Ding, J. (2018). Can multielectron intercalation reactions be the basis of next generation batteries? *Accounts of chemical research*, 51(2), 258-264.
- Whittingham, M. S., Song, Y., Lutta, S., Zavalij, P. Y., & Chernova, N. A. (2005). Some transition metal (oxy) phosphates and vanadium oxides for lithium batteries. *Journal of Materials Chemistry*, 15(33), 3362-3379.
- Williams, D. B., & Carter, C. B. (1996). The transmission electron microscope. In *Transmission electron microscopy* (pp. 3-17): Springer.
- Wong, J., Lytle, F., Messmer, R., & Maylotte, D. (1984). K-edge absorption spectra of selected vanadium compounds. *Physical Review B*, 30(10), 5596.

- Yang, Y., Fang, H., Zheng, J., Li, L., Li, G., & Yan, G. (2008). Towards the understanding of poor electrochemical activity of triclinic LiVOPO₄: Experimental characterization and theoretical investigations. *Solid state sciences*, 10(10), 1292-1298.
- Zhang, S., Li, L., & Kumar, A. (2008). *Materials characterization techniques*: CRC press.
- Zhou, F., Zhao, X., & Dahn, J. (2009). Reactivity of charged LiVPO₄F with 1 M LiPF₆ EC: DEC electrolyte at high temperature as studied by accelerating rate calorimetry. *Electrochemistry communications*, 11(3), 589-591.
- Zhou, H., Shi, Y., Xin, F., Omenya, F., & Whittingham, M. S. (2017). ϵ - and β -LiVOPO₄: Phase Transformation and Electrochemistry. *ACS applied materials & interfaces*, 9(34), 28537-28541.